ALFRED-WEGENER-INSTITUT
HELMHOLTZ-ZENTRUM FÜR POLAR-
UND MEERESFORSCHUNG

University of Potsdam
Faculty of Science
Institute of Physics and Astronomy

Master thesis

ANALYSIS AND COMPARISON OF THE ANTARCTIC ATMOSPHERIC OSCILLATION IN REANALYSIS AND CLIMATE MODEL DATA

prepared by

Johannes Riebold

from Schelldorf

Date of submission: 01.08.2019
Supervisor: Dr. Dörthe Handorf
First referee: Prof. Dr. Markus Rex
Second referee: Prof. Dr. Arkady Pikovsky

KURZZUSAMMENFASSUNG

Die Antarktische Oszillation ist bekannt als das dominante atmosphärische Variabilitätsmuster in außertropischen Regionen der Südhemisphäre und ist gekennzeichnet durch eine entgegengesetzte Schwankung von troposphärischen Luftdruckanomalien zwischen mittleren und höheren Breiten. Dieses großräumige Muster atmosphärischer Variabilität steht in engem Zusammenhang mit diversen beobachteten klimatischen Entwicklungen der jüngeren Vergangenheit auf der südlichen Erdhälfte. Aus diesem Grund wird die folgende Arbeit zunächst die zeitlichen Entwicklungen der letzten Jahrzehnte und die räumlichen Muster der Antarktischen Oszillation in der Troposphäre sowie in der Stratosphäre in Reanalysedaten untersuchen. Daraufhin werden verschiedene, um das Atmosphärenmodell ECHAM aufgebaute Modellkonfigurationen daraufhin untersucht, inwiefern sie in der Lage sind, die aus den Reanalysedaten abgeleiteten Charakteristiken zu reproduzieren.

CONTENTS

1 INTRODUCTION 1

2 ATMOSPHERIC FOUNDATIONS 3
  2.1 General composition 3
  2.2 Thermal stratification 4
  2.3 Zonal wind and temperature structure 6
  2.4 Waves and instabilities 8
  2.5 Polar vortex 9
  2.6 Ozone 10
    2.6.1 Gas phase chemistry of ozone depletion 12
    2.6.2 Heterogeneous chemistry of polar ozone depletion 13
  2.7 Teleconnections and oscillations 15
    2.7.1 The Antarctic Oscillation 17
    2.7.2 Mechanism and drivers 20

3 REANALYSIS DATA 23
  3.1 ERA-Interim 23
  3.2 Geopotential height fields 24
  3.3 Antarctic Oscillation in reanalysis data 27
    3.3.1 Tropospheric Antarctic Oscillation 27
    3.3.2 Stratospheric Antarctic Oscillation 29
  3.4 Higher order patterns of variability 31
  3.5 Frequency analysis 32

4 CLIMATE MODELS 37
  4.1 Atmospheric General Circulation Models 37
    4.1.1 Governing equations 38
    4.1.2 Coordinates and numerical schemes 39
  4.2 ECHAM 42
  4.3 Polar SWIFT 42
  4.4 MPI-ESM 44
  4.5 Evaluation of models 44
    4.5.1 General assessment of ECHAM-SWIFT 46
    4.5.2 Simulated Antarctic Oscillation patterns 48
    4.5.3 Simulated Antarctic Oscillation trends 51
    4.5.4 Correlation maps 53

5 CONCLUSION AND OUTLOOK 55

A APPENDIX 57
  A.1 Wavelet transforms of stratospheric PC time series 57
  A.2 Tropospheric AAO patterns and time series 58
  A.3 Stratospheric AAO patterns and time series 60

B METHODS 63

B.1 Empirical Orthogonal Function analysis 63
  B.1.1 Basic principle in two dimensions 63
  B.1.2 Extension and generalisation to higher dimensions 64
B.2 Trend and significances 66
B.3 Wavelet transform 66
B.4 Taylor diagram 68

BIBLIOGRAPHY

INTRODUCTION

1

Climate on the mid- and high-latitudes of the Southern Hemisphere (SH) has experienced pronounced changes over the last decades [Pachauri et al., 2014].

Due to human-made chlorofluorocarbon (CFC) emissions, which have been restricted by the Montreal Proctocol in 1989 and its amendments, losses of total ozone over Southern stratospheric polar regions exceeded 50 % during October in the late 20th century. These ozone losses peaked in the year 2000 with a record size of the well-known Antarctic ozone hole, which is however expected to fully regenerate over upcoming decades [Solomon et al., 2016] (see Chapter 2.6). Since ozone significantly contributes to radiative heating by aborbing UV-radiation, a pronounced lower stratospheric cooling by up to 10 K, as well as a strenghtening and delayed breakdown of the stratospheric circumpolar vortex (see Chapter 2.5) have been observed at high southern latitudes during the last decades [Thompson et al., 2002; Randel et al., 1999]. Furthermore, until the beginning of the 21th century one of the most rapidly regional surface warmings on Earth by several degrees over the Antarctic peninsula has been recognised [Mulvaney et al., 2012; Turner et al., 2016], and total sea ice coverage in the Southern Ocean increased by up to 1.8 % per decade—with strong regional differences however [Pachauri et al., 2014; Bintanja et al., 2013]. Additionally, scientific studies pointed out that mass losses of the West Antarctic ice sheet increased by about $\sim 70\,\%$ in the past decade. This probably accelerates sea level rise dramatically in upcoming years and centuries [Paolo et al., 2015]. Moreover, a poleward shift of the westerly wind and rainfall belt has been observed, which is generally associated with stronger westerly winds and increased rainfall over high-latitudes—and vice versa over mid-latitudes [Solman et al., 2016]. Further changes in the SH's climate system, such as potential long-term trends concerning the variability and strength of the well-known *El Niño-Southern Oscillation* (ENSO) [Cai et al., 2015] or threatened marine and terrestrial ecosystems [Hoegh-Guldberg et al., 2010] are still an area of active research. It is still an ongoing debate to what extent these observed changes may be attributed to internal climate variability or to anthropogenic forcing, such as human emissions of CO_2 or industrial CFC emissions.

Closely linked to many of these observed trends and changes is the so-called Antarctic Oscillation (AAO) (see Chapter 2.7) [Thompson et al., 2002]. The AAO is the dominant mode of extratropical atmospheric climate variability over the SH and is generally considered to be an inherent feature of the chaotic and complex atmospheric system [Gong et al., 1999; Thompson et al., 2000; Zheng et al., 2013]. In its positive phase, the AAO is characterised by lower tropospheric pressure anomalies as usual over the poles accompanied by higher tropospheric pressure anomalies over mid-latitudes—and vice versa in its negative phase.

Despite the fact that the AAO is not a result of anthropogenic forcing, human activities might have significant impact on the occurrence frequency and strength of positive and negative AAO phases. Indeed, it has been shown that especially in austral summer the combined effect of greenhouse gas increases and ozone depletion over the last decades resulted in an overall shift of the AAO towards more positive polarities [Gillett et al., 2003; Marshall et al., 2004]. However, projected ozone recovery in future times is expected to counteract the greenhouse gas-induced positive tendency of the AAO [Perlwitz et al., 2008].

Due to the high complexity and nonlinearity of the atmospheric system, climate models are typically employed to study spatial patterns, as well as the corresponding temporal trends and variability of large-scale teleconnection patterns like the AAO (see Chapter 4). In order to ensure reliable projections of future climate change and to gain a better understanding of the way natural climate variability may interact with the observed long-term trends, it is essential that climate models realistically simulate such dominant large-scale modes of internal atmospheric variability.

Therefore, the following thesis will systematically first analyse spatial patterns, recent trends as well as interannual variability of the AAO using ERA-Interim reanalysis data. Afterwards, different climate model setups, such as stand-alone atmosphere runs, as well as fully coupled model simulations are evaluated regarding their ability to reproduce the observed AAO-related features.

Special focus lies on the usage of the fast polar chemistry model SWIFT [Rex et al., 2014], which simulates polar ozone chemistry interactively allowing for a realistic representation of nonlinear feedbacks between ozone fields and atmospheric dynamic. The usage of an interactive ozone chemistry model is motivated by different previous studies:

- Thompson et al., 2002 pointed out by studying reanalysis and station-based data, that stratospheric circulation and temperature anomalies induced by ozone depletion in springtime may propagate downwards and influence tropospheric circulation (and consequently the AAO). This stratospheric influence may not only be present in spring, but also in summer due to the thermal memory of the stratosphere.

- Fogt et al., 2009 showed that climate models including time-varying ozone fields simulate recent trends in the AAO on average more realistically, compared to models considering fixed ozone climatologies.

- Romanowsky et al., 2019 demonstrated that in the Northern Hemisphere, vertical coupling processes between troposphere and stratosphere, as well as recent trends of the North Atlantic Oscillation are represented more realistically in atmospheric models including the interactive chemistry model SWIFT.

ATMOSPHERIC FOUNDATIONS 2

The Earth's atmosphere is the gaseous domain surrounding the Earth's surface and its general composition as well as its thermal stratification will be briefly described in the beginning of this Chapter (see Chapter 2.1–2.2). The AAO is a large-scale planetary teleconnection pattern over the SH and influences especially mid- and high-latitudinal southern regions (see Chapter 2.7). Therefore, Chapters 2.3–2.5 will describe relevant atmospheric large-scale features in polar and mid-latitude regions, such as the vertical and horizontal zonal wind structure, polar vortices, large-scale Rossby waves and instabilities. Special focus when assessing the capability of climate models in reproducing AAO patterns and trends is on the interactive ozone model SWIFT. For this reason, Chapter 2.6 will describe recent trends and characteristics of ozone, as well as important ozone-destructing processes, which form the basis for the simulation of polar ozone depletion within the SWIFT module.

2.1 GENERAL COMPOSITION

The right hand-side of Figure 2.1 shows the volume ratios of gases that mostly form the Earth's atmosphere. The main components, which are nitrogen (N_2, 78 %), oxygen (O_2, 21 %), argon (Ar) and carbon dioxide (CO_2), fill above 99 % of the atmospheric volume and their ratios remain nearly constant up to 80 km altitude. Greenhouse gases, such as water vapor (H_2O), carbon dioxide CO_2, nitrous oxide (N_2O) or methane (CH_4), exhibit relatively small volume ratios. These gases transmit solar UV radiation and absorb infrared radiation from the Earth's surface. This so-called natural greenhouse effect contributes to an additional overall warming of about 33 °C. As a consequence of the steady increase of greenhouse gas concentrations over the last century due to emissions from industry, combustion processes or agriculture, the greenhouse effect is enhanced resulting in additional anthropogenic warming of the atmosphere. Due to evaporation processes at the Earth's surface, relatively high amounts of water vapor can be found in very low altitudes, which accounts for about 60 % of the overall greenhouse effect. Since an overall warmer atmosphere is able to hold larger amounts of water vapor and additionally leads to higher evaporation rates at the surface, an overall increase of H_2O concentration in the atmosphere could be observed over recent decades [Chen et al., 2016]. A further essential atmospheric species for life on Earth is ozone O_3, which absorbs short-wave UV radiation ($\lambda <$380 nm). This high-energetic radiation would otherwise be extremely harmful for humans and plants. The so-called ozone layer is typically located in altitudes between 15 to 35 km (see Figure 2.1) and leads to additional warming in the respective altitude range. In this respect, tracer gases such as Chlorofluorocarbons (CFCs), as well as simple nitrogen oxides (NO_x) or chlorine oxides (ClO_x) play an important role in chemical ozone depletion cycles and heir mixing ratios generally vary with altitude due to chemical processes (see Chapter 2.6).

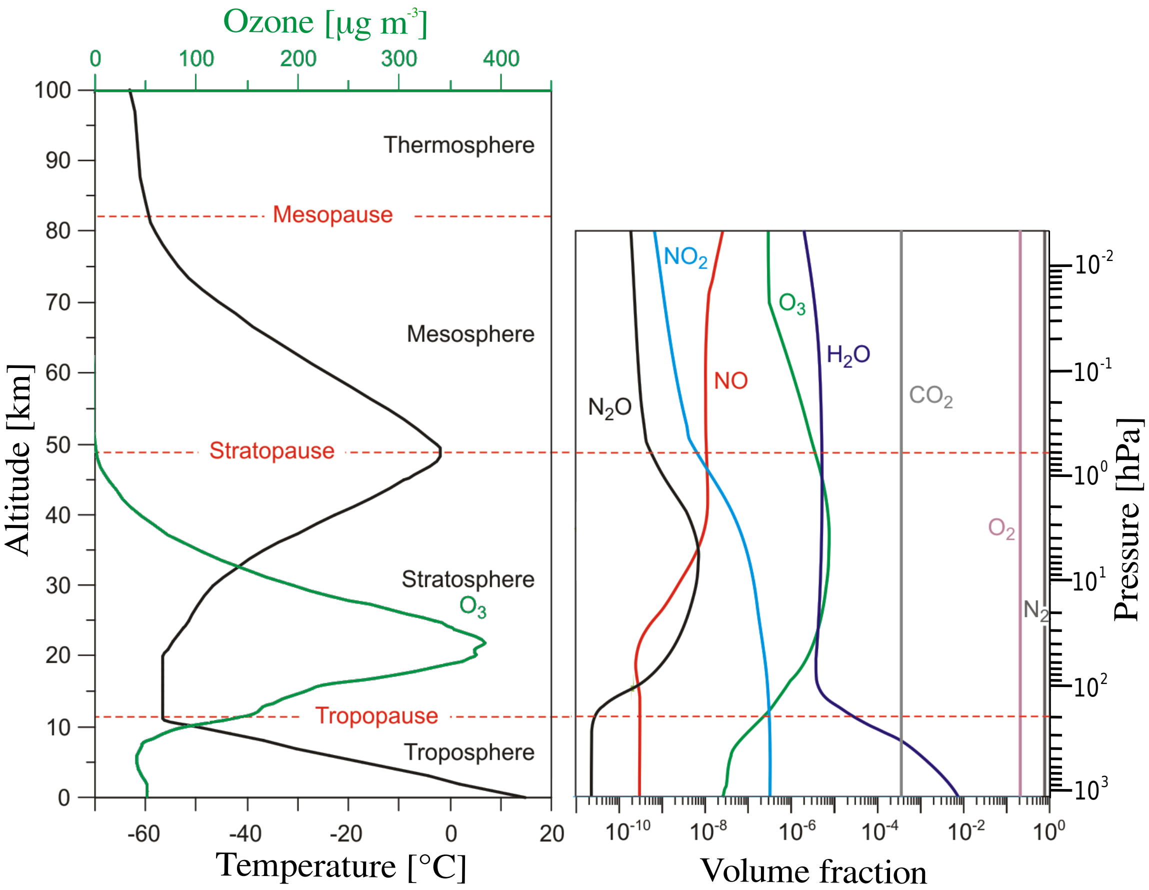

Figure 2.1: Left: general vertical temperature profile of the atmosphere and an exemplary vertical ozone profile. Right: volume fractions of the most abundant gases forming the Earth's atmosphere (picture taken and edited from: *Generalic, Eni. "Atmosphere." Croatian-English Chemistry Dictionary & Glossary. 20 Oct. 2018. KTF-Split. 14 June 2019. <https://glossary.periodni.com>*).

2.2 THERMAL STRATIFICATION

From an energetic point of view, the change of overall internal energy $\mathrm{d}U$ of an air parcel is given by the sum of heat transfer δQ with adjacent air parcels and pressure-volume work δW. This is commonly summarised by the *1st law of thermodynamics*

$$\mathrm{d}U = \delta Q - \delta W.$$

When air parcels vertically rise into levels of lower pressures they experience an expansion and release energy to their surroundings due to a release of pressure-volume work. Contrary, descending air parcels get compressed and gain energy. A common assumption for atmospheric processes is that the heat transfer δQ between an air parcel and its surrounding is negligible and that the overall change of internal energy is therefore given by the work done. This is especially an appropriate approximation for large-scale air movements and termed an adiabatic process, which can mathematically be described by the adiabatic state equations [Pichler, 1997].

The so-called dry-adiabatic lapse rate $\Gamma_\mathrm{d} = -\frac{\mathrm{d}T}{\mathrm{d}z} = 9.8\,\frac{^\circ\mathrm{C}}{\mathrm{km}}$ (z is vertical coordinate) relates to the change of temperature T, which a dry air parcel experiences when lifted adiabatically up or down in vertical z-direction. The moist-adiabatic lapse rate $\Gamma_\mathrm{m} < \Gamma_\mathrm{d}$ additionally takes into account the amount of atmospheric moisture and strongly depends on the onset of condensation and evaporation processes, which may either lead to a release or absorption of latent heat. In this respect, the potential temperature θ is commonly used and defined, which corresponds to the temperature an air parcel would attain by adiabatically bringing it down to standard reference pressure.

The general thermal vertical structure of the atmosphere is shown in Figure 2.1 and is typically divided into different layers, such as the troposphere, stratosphere, mesosphere and thermosphere. The transition regions between different layers, called tropopause, stratopause etc., are generally characterised by a significant change of the atmospheric lapse rate Γ_at—that is, the actual lapse rate of the observed atmospheric stratification.

The tropospheric layer is commonly characterised by decreasing temperatures with height. This is in general a combined result of decreasing air pressure with altitude and stronger absorption of the Earth's emitted infrared radiation by greenhouse gases in lower tropospheric layers compared to upper layers. Especially large amounts of water vapor in the lower troposphere contribute to a strong surface-near warming. Since the tropospheric atmospheric lapse rate Γ_at might potentially be larger than the respective moist or dry-adiabatic lapse rate $\Gamma_\mathrm{m/d}$ (in dependence on air humidity), unstable stratifications are possible. Such unstable configurations may lead to convective uprising activity and turbulent airflow within the troposphere. Additionally, the troposphere contains over 99 % of the total mass of water vapor and large amounts of total aerosols, which are both the most important components involved in cloud formation processes. Consequently, the tropospheric dynamics tend to be highly chaotic, which is manifested in the underlying highly nonlinear equations of motions (see Chapter 4.1.1).

The transition zone between the troposphere and the stratosphere is called tropopause and is located at around 8 km over polar regions and around 17 km above equatorial regions. The adjacent stratosphere is characterised by an overall increasing temperature trend with height. This can mainly be attributed to the direct absorption of UV radiation by relatively high amounts of ozone in the respective altitudes (see Figure 2.1). As a consequence of a negative lapse rate Γ_at, uprising and therefore adiabatically cooling air parcels in the stratosphere will immediately be restored and oscillate around their equilibrium height position with Brunt–Väisälä frequency N [Pichler, 1997]. Such a general stable stratification, as well as the fact that only small amounts of moist tropospheric air are transported across the tropopause makes the stratosphere a less turbulent and poorly mixed layer. Therefore, in contrast to the troposphere no significant vertical motions and classical cloud formation processes can be observed.

Located above the stratopause is the mesosphere, which is found at altitudes of about 50 to 85 km and is characterised by decreasing temperatures with height. The upwardly adjacent layer is called Ionosphere and includes the thermosphere, as well as the exosphere. The Ionosphere exhibits an extreme temperature increase, mostly due to absorption of sun's X-ray and extreme UV radiation.

2.3 ZONAL WIND AND TEMPERATURE STRUCTURE

Figure 2.2 illustrates the latitude-altitude profile of zonal wind u and temperature T for austral winter and austral summer season. The plots were calculated from monthly ERA-Interim data (see Chapter 3.1) averaged over the period 1979–2016. The general vertical temperature structure and stratification as described in Chapter 2.2 is very well observable with typical lapse rate inversion above the tropopause.

A main driver of atmospheric circulation is the differential heating by the sun that induces an equatorward meridional temperature gradient $\frac{\partial T}{\partial y}$ with higher temperatures at the equator and lower temperatures at the poles. As a result, convective uprising motions of less dense and warm air result in the formation of thermal lows at the surface and thermal highs in higher altitudes around the equator—and vice versa at the poles. From a coarse point of view, the resulting meridional pressure $\frac{\partial p}{\partial y}$ and density $\frac{\partial \rho}{\partial y}$ gradients at the surface and in higher altitudes give rise to meridional equatorward and poleward air motions, respectively. For a frictionless fluid on a rotating sphere with the hydrostatic and steady-state approximation being made in the equations of motion, the zonal deflection of meridional air motions by the Coriolis force can be described by the *geostrophic equation*

$$f u_g = -\frac{1}{\rho} \frac{\partial p}{\partial y}, \tag{2.1}$$

where f describes the Coriolis parameter, ρ is air density and u_g is the zonal geostrophic wind speed. This equation basically represents the established balance between pressure force and Coriolis force and motivates the overwhelming majority of westerlies especially in the upper mid-latitude troposphere.

As observable in Figure 2.2, a vertical increase of zonal wind u can be noticed in connection with horizontally decreasing temperatures (baroclinic stratification), which can be expressed by the *thermal wind equation*

$$f \frac{\partial u}{\partial z} = g \frac{\partial \ln T}{\partial y}. \tag{2.2}$$

This equation describes the strengthening or weakening of the zonal wind speed with height z due to meridional density (or temperature) gradients and is obtained by incorporating the hydrostatic equation $\frac{\partial p}{\partial z} = -\rho g$[1](cf. Chapter 4.1.1) into the geostrophic equations for zonal wind speed (see Equation 2.1) and meridional wind speed.

Due to the thermal wind relation 2.2, strongest zonal winds in the lower atmosphere are typically found near the tropopause and are associated with jet streams. However from a more profound point of view, there exist different mechanisms and approaches for explaining the existence of jets [Li et al., 2012]. The subtropical jet stream is considered to be mainly a result of angular momentum transport from the tropics into the subtropics due to the thermal *Hadley* circulation. This thermally-driven jet is usually located around 30° N/S (and more polewards

---

[1] which assumes that the overall pressure at a given point is solely a result of the mass of the air column above it,

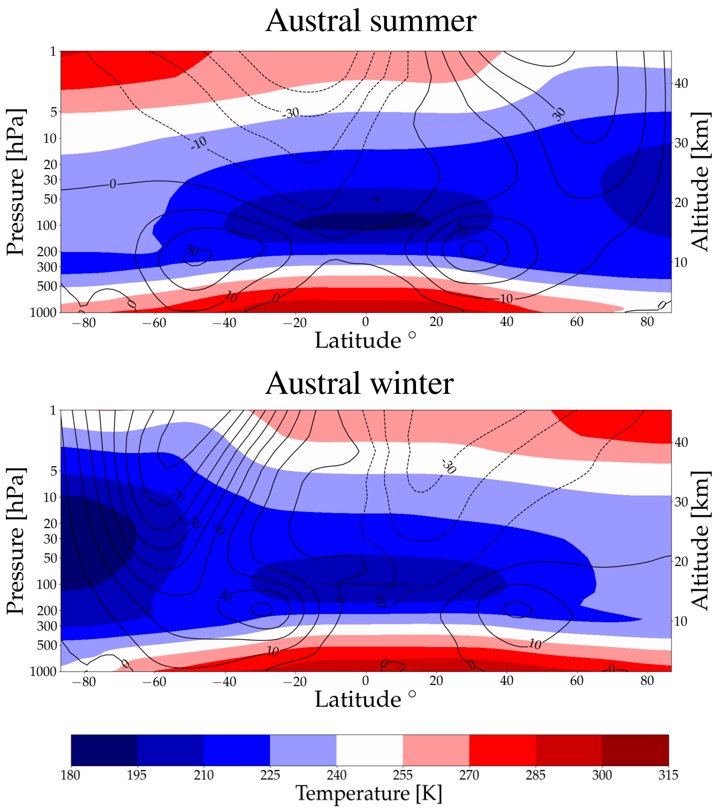

Austral summer

Austral winter

Figure 2.2: Latitude-altitude profile of zonal wind u (black contour lines with contour interval of $10\,\mathrm{m\,s^{-1}}$) and temperature T (colors) for winter and summer season calculated from monthly ERA-Interim data averaged over the period 1979-2016. The tropospheric jets at 30° (winter) and 50° (summer) on the respective hemisphere stand out as dominant features, as well as the stratospheric polar night jet in the respective hemispheric winter.

in winter), as can be noticed in Figure 2.2. A second type is the mid-latitude eddy-driven jet or sometimes called polar front jet, which emerges as a result of the convergence of the meridional eddy momentum flux[2] of zonal momentum in mid-latitude zones of enhanced baroclinic activity (see Chapter 2.4). However, both processes that lead to the formation of jets may interact and are not independent from each other, which often results in only one single observed jet maximum per hemisphere in zonal wind plots (see Figure 2.2). This is especially the case in seasons when regions of strongest baroclinicity may coincide with regions where the eddy-free subtropical jet is present [Lee et al., 2003].

---

[2] which can be decomposed into the contribution of stationary eddies $\bar{u}^*\bar{v}^*$ and transient eddies $\overline{u'v'}$, where the prime denotes deviation from time average, the asterisk denotes deviations from zonal mean and the overbar is the average over time.

2.4 WAVES AND INSTABILITIES

Atmospheric waves are usually associated with spatially periodic disturbances in fields of atmospheric variables (eg. temperature T, pressure p), which may propagate over time. The most prominent form of large-scale atmospheric waves is called *Rossby* wave, whose zonal wave numbers k_x typically corresponds to wavelengths on synoptic ($\mathcal{O} \sim 1000$ km, $k = 6-8$), or even larger planetary scales.

For the simple case of a barotropic, non-divergent, linearised and unforced atmospheric model, free Rossby waves owe their existence to the conversation of the vertical component of absolute vorticity $\eta_z = \zeta_z + f_z$. Absolute vorticity η_z is given by the sum of relative vorticity of the flow $\zeta_z = \frac{\partial v}{\partial x} - \frac{\partial u}{\partial y}$ and planetary vorticity $f_z = 2\Omega \sin(\varphi)$, where φ is latitude and Ω is Earth's rotational velocity. Thus, an air parcel displaced poleward due to an initial perturbation enters a region of higher planetary vorticity f_z and has in turn to lower its relative vorticity ζ_z by curving its trajectory equatorwards. This results in a meandering circumpolar wave pattern of the jet stream with ridges (warm tropical air, high pressure) and troughs (cold polar air, low pressure), which determine the mid-latitude weather to a large extent (see Figure 2.3). The zonal phase speed c_x of such Rossby wave-patterns within a zonal mean flow with speed u_0 is given by

$$c_x = u_0 - \frac{\beta}{k_x^2 + k_y^2}, \tag{2.3}$$

where $\beta = \frac{\partial f_z}{\partial y}$ is the meridional gradient of planetary vorticity. Thus, the phase velocity is always negative (westward) relative to the underlying zonal mean velocity u_0 . Especially stationary waves with $c_x = 0$ are discussed in the context of severe weather extremes over recent decades [Coumou et al., 2014]. Such stationary waves can however only occur in westerly flow on wavelengths around 6000 km, when the wave movement and the background flow u_0 balance.

Apart from free Rossby waves, orographic or diabatic forcing may disturb the mean zonal flow and are able to excite forced Rossby waves in the atmosphere, which are supposed to be primary responsible for the energy transfer between stratosphere and troposphere [Shaman et al., 2016]. However, perturbations of the mean flow and propagating waves within the atmosphere may either grow or decay over time leading to amplification and instabilities. The most dominant form of instability especially in mid-latitudes is the baroclinic instability, which leads to amplification of small disturbances and the formation of mid-latitude cyclones and weather systems. This form of instability only occurs in a baroclinic atmosphere with vertical shear of horizontal winds [Pichler, 1997]. Linear perturbation theory shows that for increasing vertical wind shear instability of disturbances will first occur at a certain critical wavelength on synoptic scales (∼1000 km) and the growing disturbances of the mean zonal flow gain their energy from the available potential energy supplied by the horizontal temperature gradients.

A different form of atmospheric instability is barotropic instability, which occurs due to latitudinal shear of the mean zonal flow and requires solely barotropy. In this case, energy is directly gained or restored from the mean flow. This helps to maintain the mean flow against friction in mid-latitudes, where no necessary criteria for barotropic instability are fulfilled and perturbations restore their energy back.

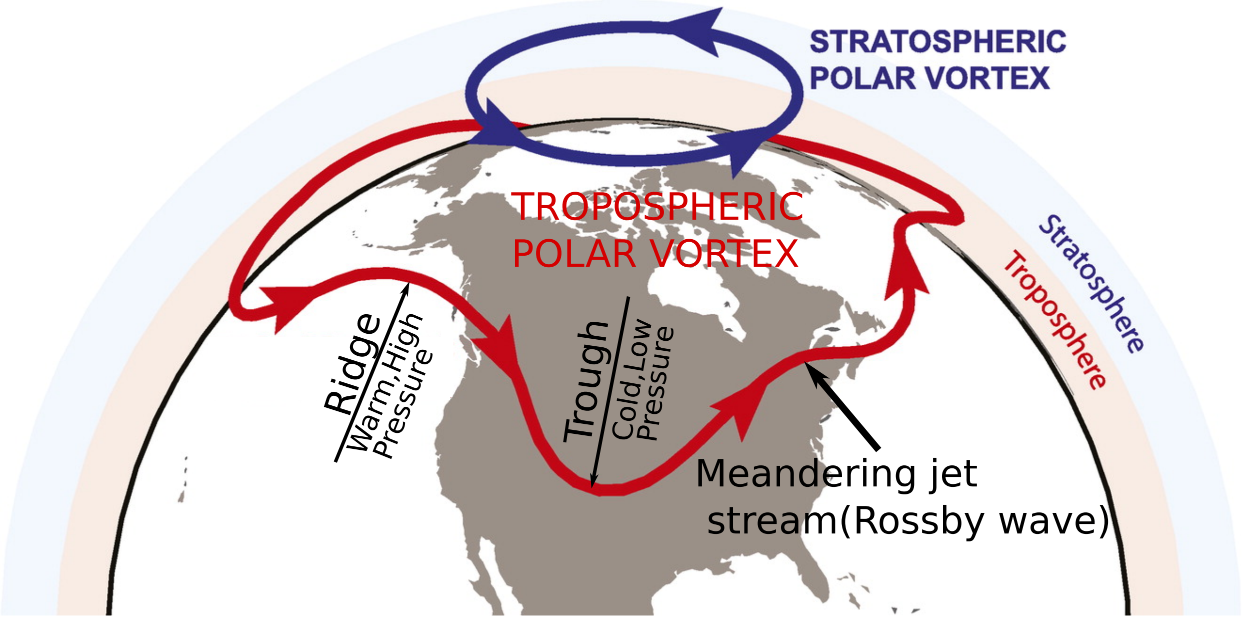

Figure 2.3: Schematic illustration of the tropospheric and polar vortex, as well as of a typical Rossby wave pattern, which results in a meandering jet stream with troughs and ridges (picture taken and edited from Waugh et al., 2017).

2.5 POLAR VORTEX

Polar vortices are an inherent feature of Earth's climate system and can be found on both hemispheres. They are generally divided, on the one hand, into a stratospheric polar vortex and on the other hand, into a tropospheric polar vortex (see Figure 2.3) [Waugh et al., 2017].

The stratospheric vortex forms in austral(boreal) fall in the SH(NH), when the polar regions begin to be completely located in the Earth's shadow and lack solar heating. It strengthens during the respective winter season and breaks down in spring, when incoming solar radiation compensates the meridional temperature gradient between polar regions and tropics by heating the polar stratosphere. Due to the strong meridional temperature gradient in fall and winter, a circumpolar planetary westerly flow is formed within the vortex, commonly called the *Polar Night Jet*. This westerly flow encircles the poles and maximises at around 60° latitude at the outer edge of the vortex with top speeds of over $80\,\mathrm{m\,s^{-1}}$ in the SH in austral winter. Along with the isolation of the vortex, temperatures drop below -80°C in the SH (see Figure 2.2).

Typically, the polar vortex is defined by sectors of high potential vorticity PV, which is defined as the product of absolute vorticity ζ_z and the vertical gradient of potential temperature $\frac{\partial\theta}{\partial z}$. It has been shown that this quantity is even conserved in a baroclinic frictionless fluid and diabatic heating and may be used to derive a variety of other dynamical variables [Hoskins et al., 1985].

As noticed in Figure 2.2, there exist significant hemispherical differences regarding shape and strength of the stratospheric vortices. This mostly arises from the fact that due to the more complex land-sea configuration in the NH, more forced Rossby waves are excited compared to the SH. In this respect, the vertical propagation of stationary Rossby waves is constrained by the criterion of Charney and Drazin [Charney et al., 1961]

$$0 < u_0 < \frac{\beta}{k_x^2 + k_y^2 + \frac{f_0^2}{4N^2H^2}} = u_c, \tag{2.4}$$

where f_0 is Coriolis parameter, N is Brunt–Väisälä frequency and H is scale height. According to this criterion, only extremely long-wave stationary Rossby waves are able to propagate upward into the stratosphere in westerly flow and disturb the vortex. Nevertheless, the vertical propagation can only proceed until a critical speed u_c of the westerly flow is reached. As a result of stronger wave activity in the NH, the NH polar vortex is less stable, meandering more stronger and warmer compared to the SH vortex and sometimes may split up into two vortices. This stronger impact of upwardly propagating waves is assumed to be an essential factor leading to more frequent *sudden stratospheric warming* events, which come along with temperature increases of 50 ◦C within a few days in the stratosphere and may cause an immediate breakdown of the vortex [Matsuno, 1971]. However, a stratospheric warming event has been observed for the first time in September 2002 on the SH as well [Charlton et al., 2005].

In contrast to the stratospheric polar vortex, the tropospheric vortex extends to much lower latitudes (typically between 40 and 50°), exists over the entire year and shows up more asymmetries due to the described impact of atmospheric waves in lower altitudes. Despite the fact that both vortices can be considered as two separated structures, they may interact by a variety of troposphere-stratosphere pathways and coupling mechanisms [Holton et al., 1995; Stohl et al., 2003].

2.6 OZONE

The typical vertical distribution of ozone as depicted in Figure 2.1 indicates that largest amounts (over 90 %) of ozone can be found in a confined altitude range from the lower stratosphere up to 35 km—the so-called ozone layer. Generally, the ozone layer around the equator is located in higher altitudes (peak concentration around 26 km) compared to the poles (peak concentration around 17 km), although its thickness varies seasonally and geographically.

Ozone acts as a climate-active gas as it affects the energy balance of the stratosphere and the troposphere. Basically, stratospheric ozone absorbs short-wave UV radiation and absorbs and emits thermal long-wave radiation, which in the case of stratospheric ozone has mainly two consequences for the Earth's surface: on the one hand, a positive long-wave radiative forcing effect is provided due to the absorption of solar UV radiation leading to additional heating of the stratosphere. The heated stratosphere emits long-wave radiation to the troposphere and contributes to additional surface warming. On the other hand, due to stratospheric ozone absorption less short-wave UV radiation reaches the Earth's surface, which leads to additional surface cooling. Nevertheless, the induced effect of surface warming overwhelms the cooling effect. This results for instance in a net negative radiative forcing on the Earth's surface caused along with stratospheric ozone depletion. The radiative effect of ozone in different altitudes generally differs significantly and strongly depends on the vertical and horizontal ozone distribution and is highly complex. [Gauss et al., 2005; Myhre et al., 2013]

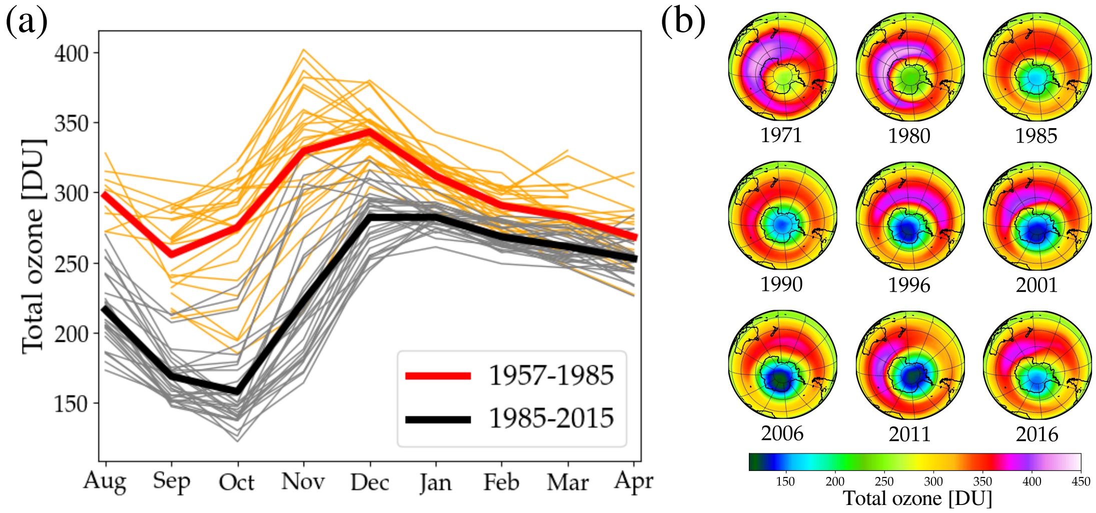

Figure 2.4: (a) Illustration of springtime ozone losses before and after the detection of the ozone hole. Thin lines depict specific years and thick bold lines indicate averages over the respective periods: 1957–1985 (orange), and 1985–2015 (grey). Units are given in Dobson unit DU, where 100 DU correspond to a 1 mm thick layer when the total ozone column would be collected at the ground under standard conditions. Data are observations at Halley station (75°S, 26°W) taken from the British Antarctic Survey (www.bas.ac.uk/). (b) Development of the Antarctic ozone hole over recent decades. Data are taken from the Copernicus Climate Change Service (cds.climate.copernicus.eu).

Additionally, ozone is among the most essential gas species for life on Earth, since it protects humans, animals and plants by absorbing extremely harmful UVC radiation (100–280 nm) almost completely, as well as large amounts of UVB radiation (280–315 nm).

The fundamental theory of photochemical formation and destruction of ozone is described by the ozone–oxygen cycle suggested by Chapman [Chapman, 1930]. Following this theory, the production of ozone is given by the reactions

$$O_2 + h\nu \rightarrow 2\,O \qquad (\lambda < 240\,\mathrm{nm}), \tag{2.5}$$

$$O + O_2 \xrightarrow{M} O_3, \tag{2.6}$$

where an oxygen molecule O_2 is first photolysed by a high energy UV photon into two oxygen atoms O. Afterwards, the oxygen atom O reacts in a third order reaction with an oxygen molecule O_2 to ozone O_3, where M represent a third molecule needed for energy balance.

In turn, the corresponding ozone destruction process within the Chapman cycle is given by the photolysis and oxydation reactions

$$O_3 + h\nu \rightarrow O(^1D) + O_2 \qquad (\lambda < 310\,\mathrm{nm}), \tag{2.7}$$

$$O + O_3 \rightarrow 2O_2, \tag{2.8}$$

where the excited oxygen atom $O(^1D)$ in Equation 2.7 is converted to an oxygen atom O when colliding with an arbitrary molecule M.

Oxygen photolysis in Equation 2.5 becomes more effective in regions where largest amounts of extremely short-wave UV radiation are supplied. Therefore, the tropical stratosphere acts as the main source region of ozone, whereas only tiny amounts are produced in tropospheric regions due to the lack of available UV radiation, which is mostly absorbed in the stratosphere located above.

However, especially between autumn and spring largest amounts of total column ozone can be found in stratospheric polar regions, whereas in the tropical stratospheric source region comparatively small amounts of total ozone are present. These greater ozone abundances accumulating in polar regions are related to a large-scale meridional circulation cell, which proceeds on timescales of about 5 years and is called the Brewer-Dobson circulation [Brewer, 1949]. This wave-driven circulation cell is characterised by uprising motions at the equator into the tropical stratosphere, where air parcels move poleward and descend at high latitudes [Holton et al., 1995]. Thus, ozone as well as other chemical species produced in the tropics are transported towards the poles, resulting in higher ozone abundances at high latitudes compared to the tropics. This transport is especially pronounced in the NH and in seasons where the Brewer-Dobson circulation is strongest due to higher wave activity (autumn, winter and spring).

2.6.1 *Gas phase chemistry of ozone depletion*

Chemistry models only considering the Chapman cycle given by Equations 2.5-2.8 would largely overestimate the amount of total ozone compared to observations; therefore, further chemical destruction processes involving ozone-depleting substances have to be considered in addition to the Chapman cycle.

These processes typically proceed in catalytic cycles of the form

$$\begin{array}{l} X + O_3 \rightarrow XO + O_2 \\ XO + O \rightarrow X + O_2 \\ \hline O_3 + O \rightarrow 2O_2, \end{array}$$

where the ozone-depleting reaction species X is permanently reproduced within the cycle and ozone is destroyed.

In this respect, a large number of catalytic cycles for several ozone-depleting chemical families and gases are known nowadays. It has early been recognised that nitrogen (X=NO) chemistry [Crutzen, 1970], as well as hydrogen (X=OH) chemistry [Bates et al., 1950] contribute to ozone depletion in the stratosphere, where the nitrogen catalytic cycle is the dominant ozone depletion process in mid-latitudes. In addition to that, ozone-depletion cycles including chlorine (X=Cl) [Stolarski et al., 1974] and bromine (X=Br) [Wofsy et al., 1975] were proposed in the 1970s.

Nevertheless, only small fractions of atmospheric nitrogen, hydrogen, bromine or chlorine are bounded in reactive and short-lived chemical compounds (NO_x, HO_x, Br_x, ClO_x), which are directly involved in ozone-destroying cycles. Rather, they are mostly bounded in reservoir gases. These reservoir gases are not able to destroy ozone directly, but may be converted to a

Family	Reactive gases	Reservoir gases	Anthropogenic source gases
Nitrogen N	NO_x : NO, NO_2, NO_3, N	$HNO_3, N_2O_5, ...$	nitrous oxide N_2O
Hydrogen H	HO_x : OH, HO_2, H	$H_2O, ...$	methane CH_4, water H_2O
Chlorine Cl	ClO_x : Cl, ClO, Cl_2O_2	$HCl, ClONO_2, ...$	CFCs
Bromine Br	Br_x : Br, BrO	$HBr, HOBr, ...$	Halones

Table 2.1: Overview over the most important ozone destroying families, their reactive gases and reservoir gases as well as anthropogenic source gases.

reactive species by other chemical processes. The sum of reactive species and reservoir species is typically termed total amount of inorganic nitrogen NO_y, hydrogen HO_y, bromine Br_y and chlorine Cl_y, respectively.

The total amount of the respective inorganic species in the stratosphere and therefore their overall potential in contributing to ozone depletion is determined by anthropogenic source gases. Generally, these emitted source gases have long residence times in the troposphere. However, when transported into the stratosphere they are photolysed by short-wave radiation and produce atomic nitrogen, hydrogen, bromine and chlorine atoms, which afterwards either destroy stratospheric ozone directly or are stored in reservoir gases of the respective family. Table 2.1 provides an overview over the four most important ozone destroying families (N, H, Cl, Br) including their reactive gases, their reservoir gases as well as anthropogenic source gases.

Around 1985, a recurring springtime ozone hole was discovered at high southern latitudes, which was characterised by an extreme ozone reduction in altitudes approximately between 14–20 km compared to previous decades [Farman et al., 1985]. As shown in Figure 2.4, this negative anomaly, which started many years before its discovery and peaked in the early 2000s, is especially pronounced in October and is still observable in present days. This was in fact quite controversial, since in winter and spring largest ozone amounts are expected at the poles due to the relatively strong Brewer-Dobson transport in these seasons.

Since the aforementioned chemical depletion processes can not sufficiently explain these extreme losses, shortly after its discovery the ozone hole was predominantly attributed to human-made emissions of chlorofluorocarbons (CFCs) and a chemical mechanism for polar ozone depletion was proposed [Solomon et al., 1986]. After CFC emissions were rigorously restricted along with the Montreal Protocol in 1989 and its amendments, the ozone hole now shows signs of recovery over recent years and is expected to completely regenerate till 2050, leading to an expected positive radiative forcing contribution over upcoming years.

2.6.2 *Heterogeneous chemistry of polar ozone depletion*

In order to explain the unprecedented polar ozone losses around the end of the 20th century, heterogeneous reactions have to be taken into account, which proceed on liquid or solid surfaces. Of major importance for ozone depletion in polar regions are Polar Stratospheric Clouds (PSCs). These clouds are basically categorised into three classes depending on their chemical composition and begin to form at very low temperatures below -78 °C.

In polar winter, reservoir species of chlorine (HCl, $ClONO_2$) react on the surface of PSCs to chlorine molecules Cl_2. When first sun rays reach the polar stratosphere in spring, these chlorine molecules are immediately photolysed into reactive chlorine species ClO_x, which initiate the important ozone-depleting chlorine cycle

$$2\,(Cl + O_3 \rightarrow ClO + O_2) \tag{2.9}$$

$$ClO + ClO \xrightarrow{M} Cl_2O_2 \tag{2.10}$$

$$Cl_2O_2 + h\nu \rightarrow 2\,Cl + O_2 \tag{2.11}$$

$$2\,O_3 + h\nu \rightarrow 3\,O_2, \tag{2.12}$$

leading to massive ozone losses in polar regions in spring time. In this respect, a feedback mechanism between springtime ozone losses and PSCs was proposed: springtime ozone losses reduce stratospheric temperatures, which in turn prolongs the presence of PSCs and consequently also the formation of ozone-destroying ClO_x species [Jones et al., 1995].

An additional effect of PSCs that enhances ozone depletion is the conversion of active nitrogen NO_x to the reservoir species HNO_3 on PSC surfaces. Hence, less NO_x is available in the stratosphere, which is able to deactivate the reactive chlorine species ClO_x into chlorine reservoir gases Cl_y. Additionally, when cloud drops within the PSCs grow in size, the bounded HNO_3 may be sediment to lower altitudes by gravity and cannot be converted to chlorine-deactivating NO_x by sunlight in spring. This process, called denitrification, finally favours ozone depletion in spring.

As explained in Chapter 2.5, the polar vortex on the SH is more isolated and colder compared to the NH; hence more PSCs are forming during winter and therefore the aforementioned processes are more active on the SH. Thus, the polar ozone hole is much more pronounced in the SH in contrast to the NH.

2.7 TELECONNECTIONS AND OSCILLATIONS

It has long been recognised that global atmospheric weather systems are linked and connected over large distances, which was already noted by the Vikings at the beginning of the second millennium [Feldstein et al., 2017] and recorded for the first time in David Crantz's *The History of Greenland(1767):*

"It has been many times remarked, that the weather in Greenland is just the reverse to that in Europe; so that when the temperate climates are incommoded with a very hard winter, it is here uncommonly mild, and vice versa."[Vallis et al., 2008]

First extensive studies on atmospheric linkages were carried out by Sir Gilbert Walker in the 1920s, who collected large amounts of data from an extensive station network at that time and revealed relationships between distant regions by employing correlation analyses. Three patterns of pressure anomalies[3] were noted and named the *North Atlantic Oscillation* (NAO), *North Pacific Oscillation* (NPO) and *Southern Oscillation* (SO), which extend over the SH and a large part of the NH [Walker, 1923]. To illustrate these anomaly patterns, Figure 2.5 depicts one-point correlation maps for Sea Level Pressure (SLP) anomalies, showing the correlation coefficient of each respective grid point time series with the time series of a reference point.

The SO relates to a see-saw like oscillation of sea level pressure between Australia-Indonesia and the South-East Pacific, induced by a thermally driven east-west circulation over the Pacific ocean, which was named the Walker circulation in his honour many years later. In combination with the ocean system, the resulting oscillations in SLP, as well as in Sea Surface Temperature (SST) and zonal winds are nowadays well-known as the El Niño-Southern Oscillation (ENSO). In its normal phase, ENSO is characterised by cold SSTs, relatively high pressures near the ground and dry conditions in the East Pacific in connection with upwelling of cold and nutrient-rich deep water at the South-American coast—and vice versa in Western Pacific regions. The reversal of these normal conditions every 2–7 years in El Niño years leads to severe droughts in Indonesia and heavy rainfall over South America. However, there also exist potential linkages and teleconnections related to ENSO over the entire globe, such as with the Indian monsoon or African precipitation [Torrence et al., 1999; Diaz et al., 2001].

The NAO and NPO describe two important dipole-like patterns of pressure anomalies on the NH, which are observed in the Northern Atlantic and the Northern Pacific region, respectively [Hurrell, 1996]. The NAO is commonly associated with negatively correlated pressure anomalies between the Icelandic low and the Azores high, whereas the NPO is typically related to the fact that pressure fluctuations over Hawaii are opposed to those over Alaska and the Bering Sea. Together with other detected anomaly patterns, such as a wave-like pattern called Pacific North American Oscillation (PNA) [Wallace et al., 1981] or a dipole-like pattern over the North Atlantic-European region termed East Atlantic Oscillation (EAO) [Mikhailova et al., 2016], all of these teleconnections were studied extensively over recent years and have been shown to have significant regional and large-scale impact on the entire NH's climate system and its temporal variability [Trigo et al., 2002; Linkin et al., 2008].

---

[3] Anomalies are typically defined as deviations from the mean annual cycle.

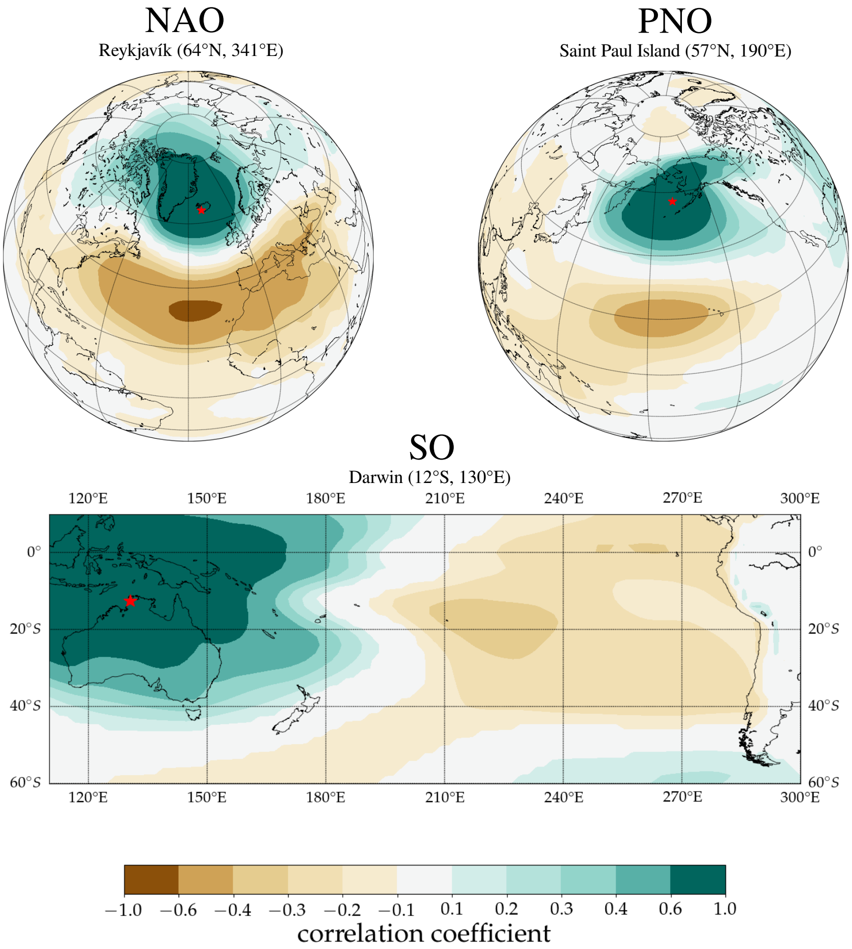
NAO
Reykjavík (64°N, 341°E)
PNO
Saint Paul Island (57°N, 190°E)
SO
Darwin (12°S, 130°E)
120°E
150°E
180°E
210°E
240°E
270°E
300°E
0°
20°S
40°S
60°S
−1.0
−0.6
−0.4
−0.3
−0.2
−0.1
0.1
0.2
0.3
0.4
0.6
1.0
correlation coefficient

Figure 2.5: One-point correlation maps for the three teleconnection and oscillation patterns identified by Walker, calculated from detrended monthly mean SLP anomaly time series from ERA-Interim data for the period 1979–2012: the North Atlantic Oscillation NAO (upper left), the Northern Pacific Oscillation NPO (upper right) and the Southern Oscillation SO (bottom). The correlation coefficients at each grid point were calculated with respect to the time series of a reference point, which is indicated by the red star.

From a classical point of view, the term teleconnection is used in atmospheric science to describe all forms of climatic linkages or relations on intraseasonal to interannual timescales—either directly or indirectly—between geographically separated regions. These regions might be thousands of kilometres apart from each other.

However, the word teleconnection was first used in the mid 1930s [Ångström, 1935] and had not established itself in climatic literature until the 1980s. The name basically refers to the fact that some kind of information is transported between distant regions throughout the atmosphere, which may result in positive or negative correlations. These teleconnection patterns can be identified by employing statistical analysis techniques, such as correlation and regression maps or empirical orthogonal function analysis, on a variety of atmospheric variables [Wallace et al., 1981].

2.7.1 *The Antarctic Oscillation*

In 1928, Sir Gilbert Walker stated as well:
"Just as in the North Atlantic there is a pressure opposition between the Azores and Iceland,... , there is an opposition between the high pressure belt across Chile and the Argentine on the one hand, and the low pressure area of Weddell Sea and the Bellingshausen Sea on the other." [Gong et al., 1999]

However, the scarcity of observational data from the Antarctic region did not allow for more profound research on this supposed relation between the mid- and high-southern latitudes.

In the late 20th century, when more data from the high-latitudes of the SH became available and more analyses were carried out, the existence of such a relation in mid- and high-latitudinal southern regions was confirmed and named the *Antarctic Oscillation* AAO [Rogers et al., 1982].

The Antarctic Oscillation describes the most dominant mode of extratropical climate variability on interannual to intraseasonal timescales over the SH [Thompson et al., 2000]. In the troposphere, it is associated with an alternation and meridional exchange of masses between the mid- and high-southern latitudes, resulting by convention in higher pressure anomalies over mid-latitudes and in lower pressure anomalies over Antarctica in its positive phase—and vice versa in its negative phase. For illustration, Figure 2.6 shows polar stereographic plots of ERA-Interim monthly z'_{700} geopotential height anomalies (see Chapter 3.2)) for a negative tropospheric AAO phase (February 2002) and a positive AAO phase (May 1989). Also shown is a one-point correlation map for SLP anomalies as in Figure 2.5.

Furthermore, Figure 2.7 depicts the crosscorrelation coefficients of zonally averaged monthly SLP anomalies on the SH using ERA-Interim reanalysis data. The tropospheric AAO manifests itself in a strong and significant negative correlation down to -0.76 between mid-latitudes (40°S) and high-latitudes (60–70°S). This implies that increasing pressures above the mid-latitudes are typically accompanied by decreasing pressures above high-latitudes and vice versa. In order to characterise the current state of the tropospheric AAO at a respective time, several Antarctic Oscillation-indices (AAOI) have been defined. The first and perhaps most simplest definition of an topospheric AAOI using reanalysis data was given by Gong et al., 1999:

$$\mathrm{AAOI} = P^*_{40^\circ S} - P^*_{65^\circ S}, \tag{2.13}$$

where $P^*_{40^\circ S}$ and $P^*_{65^\circ S}$ stand for the normalised zonal mean SLP of 40°S and 65°S, respectively. A slightly different definition is given by Nan et al., 2003, who used $P^*_{70^\circ S}$ instead of $P^*_{65^\circ S}$ by reason of supposedly stronger negative correlations between 40°S and 70°S compared to 40°S and 65°S. To examine the reliability of such reanalysis-based tropospheric AAOI prior to the satellite era, station based indices have been introduced. Such station based indices were for instance defined by Marshall, 2003, who used SLP observations from six stations located at 40°S and 65°S, respectively, in order to provide a proxy zonal mean. A more sophisticated and nowadays frequently used definition of the AAOI is given by the first principal component of the leading Empirical Orthogonal Function (EOF) as described in Chapter B.1. Some more indices with their individual strengths and weaknesses have been defined over the last years [Ho et al., 2012]. However, it is pointed out that time series of differently defined AAOI are strongly and significantly correlated, as it can be noted in Figure 2.7.

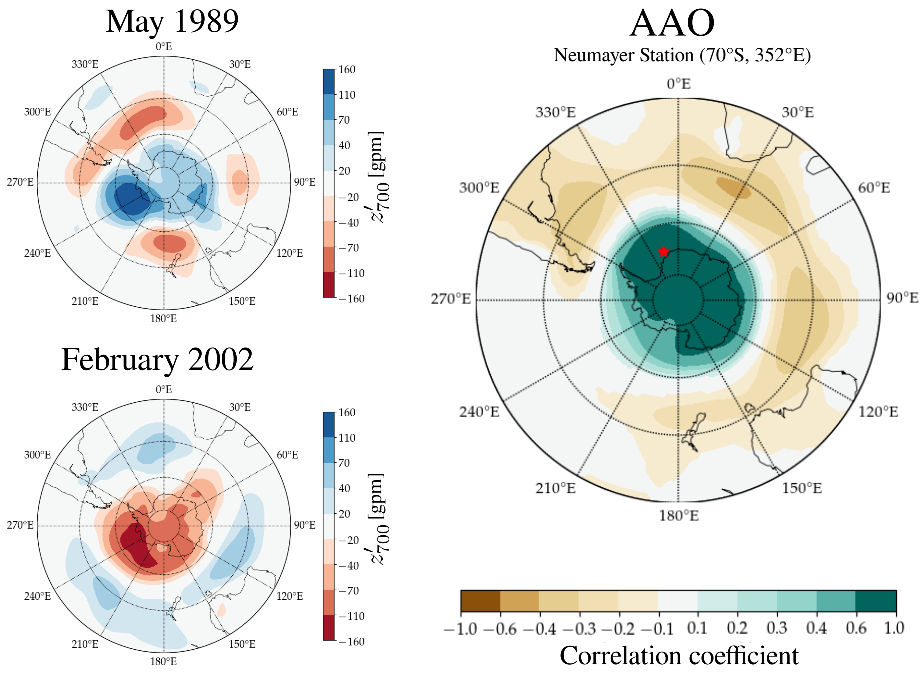
May 1989

February 2002

AAO

Neumayer Station (70°S, 352°E)

Figure 2.6: Left: Examples of a positive tropopsheric AAO phase (top, May 1989) and a negative tropospheric AAO phase (bottom, February 2002). Plottet are z'_{700} geopotential height anomalies taken from ERA-Interim. Right: Same one-point correlation map as in Figure 2.5 for SLP anomalies for illustrating the anticorrelation between mid- and high-latitudes and the AAO.

The tropospheric AAO can not be considered as an isolated atmospheric phenomenon, given that several studies over recent years and decades have demonstrated that it is strongly related to other components of the climate system over the entire SH [Hall et al., 2002].

As expected by the definition of the AAO in the troposphere, the correlation plot in Figure 2.8 between the station based Marshall AAOI and geopotential height anomalies z'_{700} (see Chapter 3.2) indicates that a high polarity state is related to higher pressure anomalies over the mid-latitudes and lower anomalies over Antarctica—and vice versa for negative polarities. Since the tropospheric AAO is dominated by ring-shaped and zonally symmetric components in mid- and high-latitudes, it is also referred to as the Southern Annular Mode (SAM). Its counterpart on the Northern hemisphere is therefore typically called the Arctic Oscillation (AO), or Northern Annular Mode (NAM).

Probably the most prominent consequence observed during a positive tropospheric AAO phase is a strengthening of the westerly wind belt. This is a result of an increase of the meridional pressure gradient $\frac{\partial p}{\partial y}$ between the mid- and high-latitudes, which increases zonal geostrophic wind speeds according to Equation 2.1 [Lovenduski et al., 2005]. The correlation map in Figure 2.8 between the station-based Marshall tropospheric AAOI and zonal wind speed u indicates that the anomalously strong pressure gradient during a positive AAO phase acts to significantly strengthen the westerly winds at around 55°S, and to weaken westerlies at around 35°S (easterly anomaly), which finally results in a shift of the westerly wind belt towards Antarctica. In this respect, a southward shift of the Antarctic circumpolar stormtrack has been recognised in con-

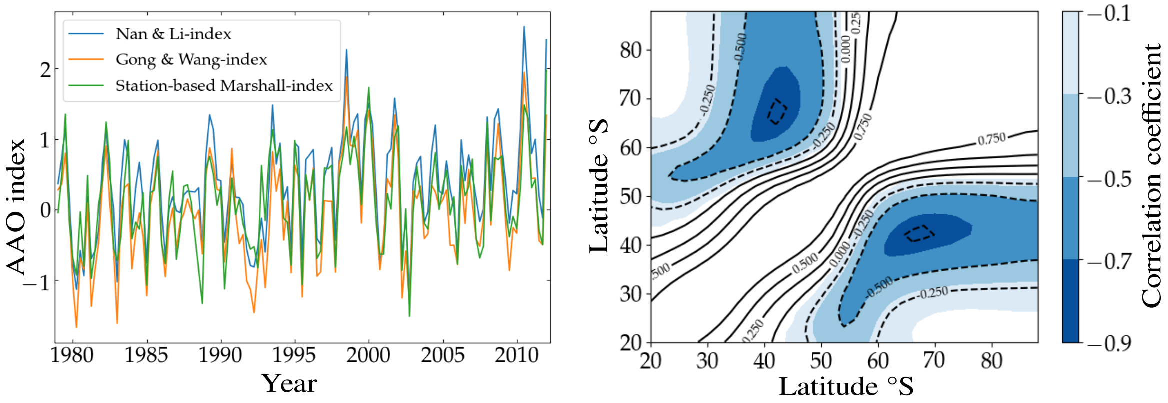

Figure 2.7: Left: Time series of different tropospheric AAOI: Nan and Li (blue), Gong and Wang (orange) and station based Marshall index (green). All indices show up to be very similar by visual inspection and are strongly correlated with each other. Right: Crosscorrelation coefficients of zonally averaged SLP anomalies for all months on the SH using ERA-Interim data.

nection with a positive polarity of the tropospheric AAO [Gillett et al., 2006]. These stormtrack regions act as relatively narrow zones with strongest baroclinic wave activity, where extratropical cyclonic storms travel driven by prevailing winds.

As a consequence of the aforementioned zonal wind variability, the frictional transfer of momentum at the air–sea interface is subjected to variations too, and may affect ocean circulations on the SH. Therefore, positive westerly wind anomalies during a positive tropospheric AAO phase increase northward Ekman transport of surface water between 45°S and 65°S. Contrary, the associated easterly wind anomalies in lower latitudes induce stronger southward Ekman transport between 30°S and 45°S. Mass conservation induces that the divergence around the Antarctic coast implies stronger nutrient-rich deep water upwelling, which favours biological productivity. In constrast, the convergence around 45°S causes stronger surface water downwelling. In this respect, it was noticed that a slight increase of chlorophyll concentration around the Antarctic coast and a decrease at around 45°S could be detected as a response to an increasing tropospheric AAOI [Lovenduski et al., 2005]. Additionally, it was shown that the previously described upwelling effect around the Antarctic coast is connected to stronger ice shelf basin melting in certain coastal regions, which possibly acts as a driver for the destabilisation of the Antarctic Ice Shelf [Greene et al., 2017]. Furthermore, it was proposed that a more intense circumpolar current might be associated with a positive tropospheric AAO polarity [Hall et al., 2002].

Studies on the effect of an increasing tropospheric AAOI on the Sea Ice Extent (SIE) in the Southern Ocean suggest that the main response results, on the one hand, in a decrease of sea ice in the Weddell Sea and Bellinghausen Sea, and one the other hand, in an increase in the central Pacific sector (Ross Sea, Amundsen Sea) [Lefebvre et al., 2004]. This may be attributed to anomalous meridional heat fluxes and sea ice advection in the respective regions. It has been proposed that an anomalous poleward meridional heat flux in the vicinity of the Anarctic Peninsula during positive tropospheric AAO polarities advects warmer air from mid- and low-latitudes and therefore lowers SIE in the Weddell and Bellinghausen Sea [Liu et al., 2004]. This enhancement of poleward meridional heat flux contributes to anomalous warm surface temperatures over the Antarctic Peninsula during positive tropospheric AAO phases. Furthermore, significant regional warmings over southern Chile and Argentina, over Tasmania, south-eastern Australia, over the South Island of New Zealand, as well as anomalously cold surface temperatures over most of Antarctica have been observed in connection with an increasing AAOI [Gillett et al., 2006]. The correlation map in Figure 2.8 indicates additional surface warming over the southern Indian and Atlantic Oceans during positive AAO phases and reproduces the aforementioned continental warming regions partly. This differences might be due to the low quality of ERA-Interim 2-m air temperatures over Antarctica compared to station based data [Jones et al., 2015]).

Moreover, high-index polarities of the tropospheric AAO are shown to be connected to anomalous fluxes of CO_2 from the Southern Oceans to the atmosphere [Butler et al., 2007], which in turn favours the poleward shift of stormtracks [Miller et al., 2006]. In addition to the previous impacts, several other studies pointed out aspects related to the polarity of the AAO, such as the intensification of wildfire activity during a positive phase, as well as precipitation changes in South America [Holz et al., 2011; Silvestri et al., 2003], Australian rainfall [Meneghini et al., 2007] or dust weather frequency in China [Fan et al., 2004].

2.7.2 *Mechanism and drivers*

The origin of the tropospheric AAO, as well as the driving mechanisms beyond other teleconnections, is a topic of ongoing research and debate due to the complexity of the atmospheric system.

Teleconnection patterns such as the PNA wave train or the mid-latitude wave-like features of the AAO suggest that these modes of variability are at least partially driven and connected to Rossby waves [Hoskins et al., 1981; Karoly, 1989; Seo et al., 2017]. However, the general form of annular modes and oscillation patterns, such as the tropospheric AAO or the AO, have been shown to appear in aquaplanet general circulation models with zonally symmetric boundary conditions and without orographic or diabatic excitation of forced Rossby waves [Cash et al., 2002]. Therefore, it is widely accepted that the AAO and the AO, as well as other oscillation patterns, basically arise from internal atmospheric dynamics. However, land-sea contrasts and diabatic heat sources might be responsible for shaping zonal asymmetries in mid-latitudes, which are not as pronounced in aquaplanet simulations with uniform surface and zonally symmetric boundary conditions [Sempf et al., 2005].

A potential explanation for the vacillation of the jet stream associated with positive and negative tropospheric AAO polarities (see Figure 2.8 (top right)) is a mutual reinforcement mechanism between eddies and the mean zonal flow. An anomalously strong jet stream leads to enhanced baroclinic eddy activity in the respective region, which in turn strengthens the jet and favors eddy activity again [Hall et al., 2002; Limpasuvan et al., 1999]. Since eddy activity is especially pronounced in stormtrack regions in the centers of the southern Indian, Pacific and Atlantic ocean, strongest anticorrelation in pressure between mid- and high-latitudes can be found in these region (see Figure 2.8 top left). Additionally, minimal stochastic models simulating the vacillation of the jet stream as a Wiener process by taking into account conservation

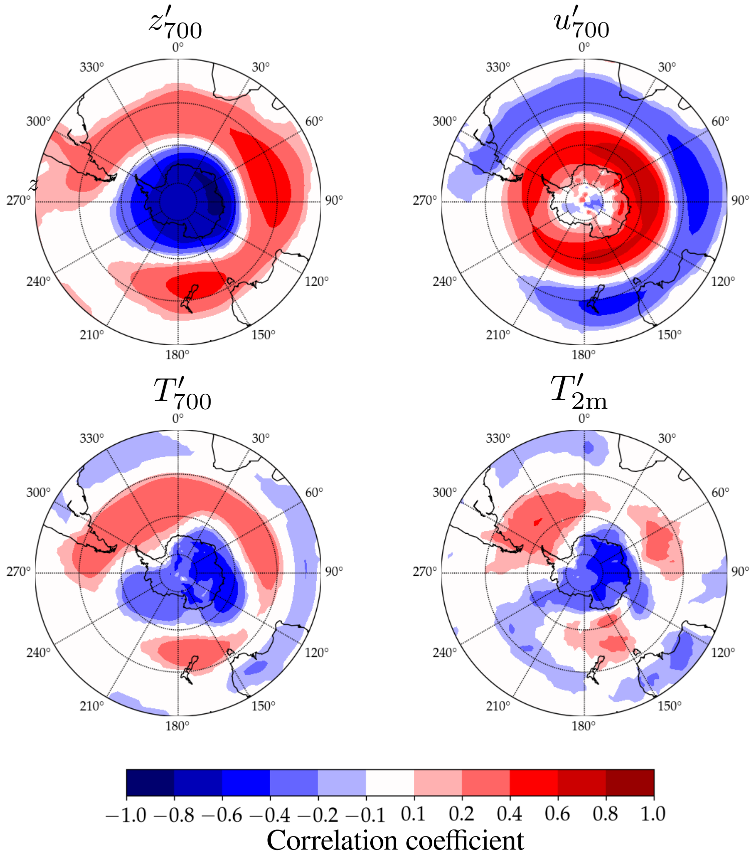

Figure 2.8: Correlation map between the station-based Marshall tropospheric AAOI and anomalies of geopotential height of the 700 hPa pressure level z_{700}, zonal wind u_{700} and temperature T_{700} at 700 hPa, as well as 2-m air temperature ($T_{2\mathrm{m}}$). All time series have been detrended before computing the correlation. The station-based Marshall indices are taken from: *Marshall, Gareth & National Center for Atmospheric Research Staff (Eds). Last modified 19 Mar 2018. "The Climate Data Guide: Marshall Southern Annular Mode (SAM) Index (Station-based)." Retrieved from https://climatedataguide.ucar.edu/climate-data/marshal*

of zonal momentum [Gerber et al., 2005], showed similar anticorrelated features between mid- and high-latitudes as observed in Figures 2.7 (right) and 2.8 (top right).

As shown for the AAO's counterpart in the NH—the AO—a different perspective is to interpret the positive and negative phases of such annular modes of variability in terms of circulation regimes [Sempf et al., 2007]. These circulation regimes correspond to preferred atmospheric configurations and may be considered as parts of a chaotic attractor of the underlying large-scale nonlinear atmospheric system. This chaotic attractor includes phase space regions belonging to positive and negative states of the annular mode and allows for occasional transitions between these phase state regions. In this respect, tuning experiments employing three-layer models proposed a potential bifurcation route for the AO, which finally related the regime behavior within the chaotic attractor to transitions between the ruins of formerly coexisting attractors. It seems plausible that dynamics in the SH underlie such a scenario as well.

3 REANALYSIS DATA

Reference atmospheric data are necessary for the analysis of atmospheric dynamics or variability, as well as to evaluate and compare the performance of contemporary atmospheric models. Such ”real-world” data are commonly given either by *in-situ* observations and measurements, such as from thermometers or rain gauges, or by so-called reanalysis data.

Atmospheric reanalysis datasets provide comprehensive retrospective snapshots of the atmospheric system at regular intervals over long time periods and are among the most frequently used data sets in climate science. They are generated via data assimilation, a technique that combines historical observations from different sources and model-based forecasts in order to estimate the state of the atmopsheric system as accurately as possible. Observational data include for instance measurements from ground-based stations, ships, aeroplanes, satellites or upper-air soundings. Typically, the assimilation procedure at a certain time step consists of a first-guess of the atmospheric state generated by a numerical weather prediction model and is based on the atmospheric state of the previous time step. The forecast is then updated in light of the observations by a distinct assimilation scheme, for instance variational methods or ensemble Kalman-filter [Reich et al., 2014]. Thus, even with spatially inhomogeneous observations the assimilation system produces completely gridded atmospheric state estimates at every time step for all kinds of atmospheric variables.

Different reanalysis products, such as the European ECMWF (European Centre of Medium-Range Weather Forecasts) reanalysis and the American NCEP/NCAR (National Centers for Environmental Prediction/National Center for Atmospheric Research) reanalysis, generally use different observational data, atmospheric models and assimilation schemes.

Since reanalysis data are a result of a complex inferential process that involves theory-based calculations, errors and uncertainties in such datasets are generally less well understood and calculable compared to traditional observations and measurements [Parker, 2016]. Furthermore, changes in observational methods over time could produce spurious trends or biases. Especially in regions, where observations are of low quality and stem from earlier time periods (as those prior to the beginning of the modern satellite era in the late 1970s) or over remote and data sparse regions, reanalysis data primarily depend on the model forecast and should be treated with more suspicion [Screen et al., 2011; Bromwich et al., 2007].

3.1 ERA-INTERIM

For analyses in this thesis, data from the ERA-Interim reanalysis [Dee et al., 2011] are used, which is a global atmospheric reanalysis dataset provided by ECMWF and is the successor of the ERA40 product. The ERA-Interim dataset covers the time period from January 1979 till August 2019 and was motivated particularly to improve issues of the predecessors. Such shortcomings of the predecessors include for instance several bias corrections, as well as the representation of hydrological cycles and stratospheric circulation [Hagemann et al., 2005].

The ERA-Interim reanalysis is produced based on a 2006 release (Cy31r2) of the ECMWF Integrated Forecasting System (IFS). The IFS incorporates a forecast model with three fully coupled components for the atmosphere, land surface and ocean waves. Additionally, as a core element it employs a 4D-Var (4-dimensional variational analysis) assimilation scheme using a 12 hourly analysis cycle. During each cycle, available observations are combined with prior information from the forecast model to estimate the evolving state of the global atmosphere. This results in a dataset with 6-hourly gridded estimates of 3-dimensional meteorological fields, as well as 3-hourly estimates of surface parameters and other 2-dimensional variables. On average, about 10^7 observations are assimilated per day, mostly originating from satellites measurements, such as clear-sky radiances from polar-orbiting and geostationary sounders and imagers, or wind and ozone retrievals from various satellite-borne sensors and scatterometers. Additionally, data from radiosondes, pilot balloons, wind profilers or other ground-based stations are assimilated.

The IFS operates on 60 vertical levels from the surface up to 0.1 hPa with spectral resolution T255 (see Chapter 4.1.2). This results in a horizontal resolution of approximately 80 km on the corresponding reduced N128 Gaussian grid, which is equally spaced in distance. However, the ERA-Interim data used in this thesis are horizontally regridded to a $2 \times 2°$ regular latitude-longitude grid and vertically reduced to 37 levels, since when studying large-scale atmospheric phenomena coarser resolution is generally sufficient.

3.2 GEOPOTENTIAL HEIGHT FIELDS

The central climatic variable in this thesis is the geopotential height $z_g(p)$ of different pressure levels p, defined as

$$z_g(p) = \frac{1}{g_0} \int_0^{h(p)} g(\varphi, z) \mathrm{d}z, \tag{3.1}$$

where $h(p)$ is the geometrical height of a given pressure level p, $g_0 = 9.80665 \, \frac{\mathrm{m}}{\mathrm{s}^2}$ is the reference gravity constant, φ is latitude, and z is geometric height. The associated unit geopotential metre (1 gpm) corresponds to the geometrical height z above sea level at which an air parcel with mass 1 kg has a potential energy of 9.80665 J. Thus, at mid-latitudes, where the gravity constant g is close to g_0, 1 gpm approximately coincides with a geometric metre. At the poles, where $g > g_0$, a geopotential metre corresponds to less than one geometrical metre, and vice versa at the equator. Since an air parcel moving along a surface of constant geopotential height (isohypses) maintains its potential energy, geopotential height is commonly used as the vertical coordinate in atmospheric research instead of geometric height z.

Figure 3.1 depicts the mean fields of geopotential heights at the 700 hPa pressure level [1], termed z_{700}. Also shown is the standard deviation $\sigma_{z'_{700}}$ of the 700 hPa geopotential height anomaly field. These plots were calculated from monthly ERA-Interim data for the time period 1979–2016 over the SH. Shown are diagrams for austral summer DJF (December, January,

---

[1] The 700 hPa pressure level is located approximately 3 km above sea level in the troposphere and was chosen since most parts of Antarctica have a lower elevation. ERA-Interim data are extrapolated using the hydrostatic equation for altitude regions where the orography exceeds 3 km.

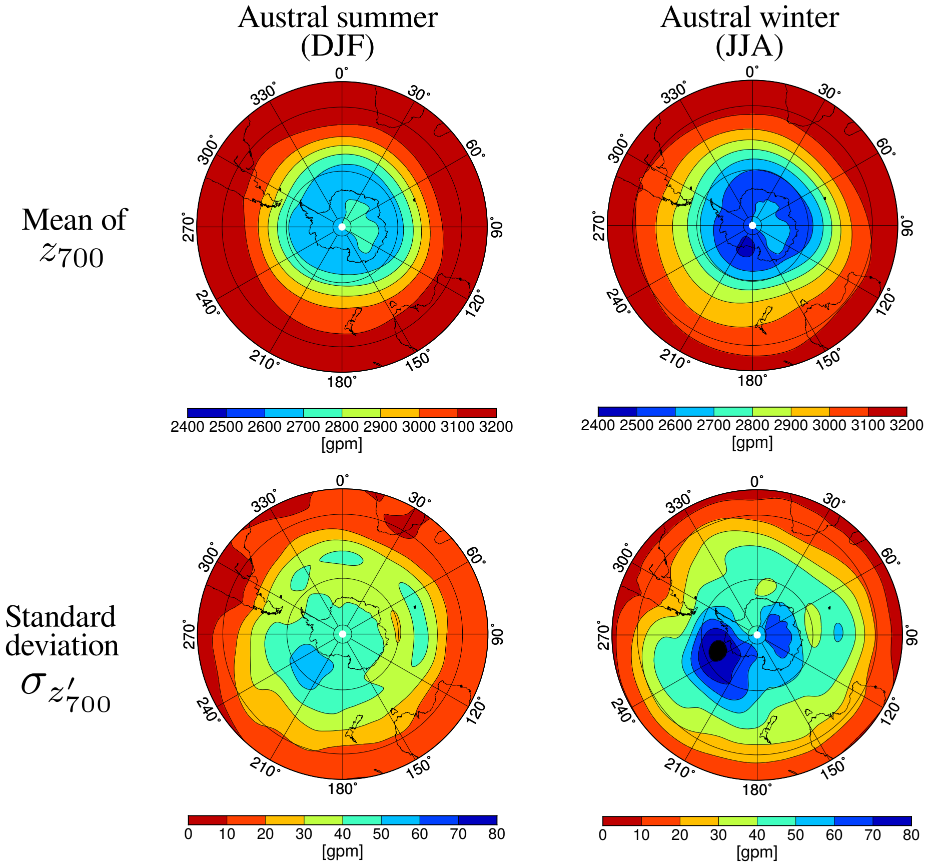
Austral summer (DJF)
Austral winter (JJA)
Mean of z_{700}
Standard deviation $\sigma_{z'_{700}}$
0°
30°
60°
90°
120°
150°
180°
210°
240°
270°
300°
330°
2400 2500 2600 2700 2800 2900 3000 3100 3200
[gpm]
0 10 20 30 40 50 60 70 80
[gpm]

Figure 3.1: Upper row: Mean field of the geopotential height field z_{700} at the 700 hPa pressure level for austral summer (DJF) and austral winter (JJA) computed from monthly mean ERA-Interim data for the period 1979–2016. Lower row: Standard deviation $\sigma_{z'_{700}}$ of the detrended geopotential height anomaly field z'_{700} calculated from monthly mean ERA-Interim data for the period 1979–2016.

February), as well as for austral winter JJA (June, July, August). Geopotential height anomalies z'_{700} are generally defined as deviations from the mean annual cycle. In order to calculate these anomalies z'_{700}, the multi-year monthly mean for the time period 1979–2016 was calculated at each grid point from the geopotential height time series z_{700} and afterwards subtracted from z_{700} for each respective month.

The mean field of z_{700} is characterised by a zonally symmetric decrease towards the poles of several hundred gpm, which is primarily a consequence of the meridional temperature gradient induced by the differential heating of the sun. As already outlined in Chapter 2.3, this gradient in temperature (and therefore in z_{700}) is particularly pronounced in austral winter due to the strong diabatic cooling at high latitudes during polar night.

Furthermore, a general feature is the poleward increase of interannual variability $\sigma_{z'_{700}}$ detected in each season. This might reflect the strong variability and susceptibility of the polar climate system due to the huge variety of different polar feedback mechanisms.The maximum variability $\sigma_{z'_{700}}$ at high-latitudes is observed over West Antarctica and the Amundsen

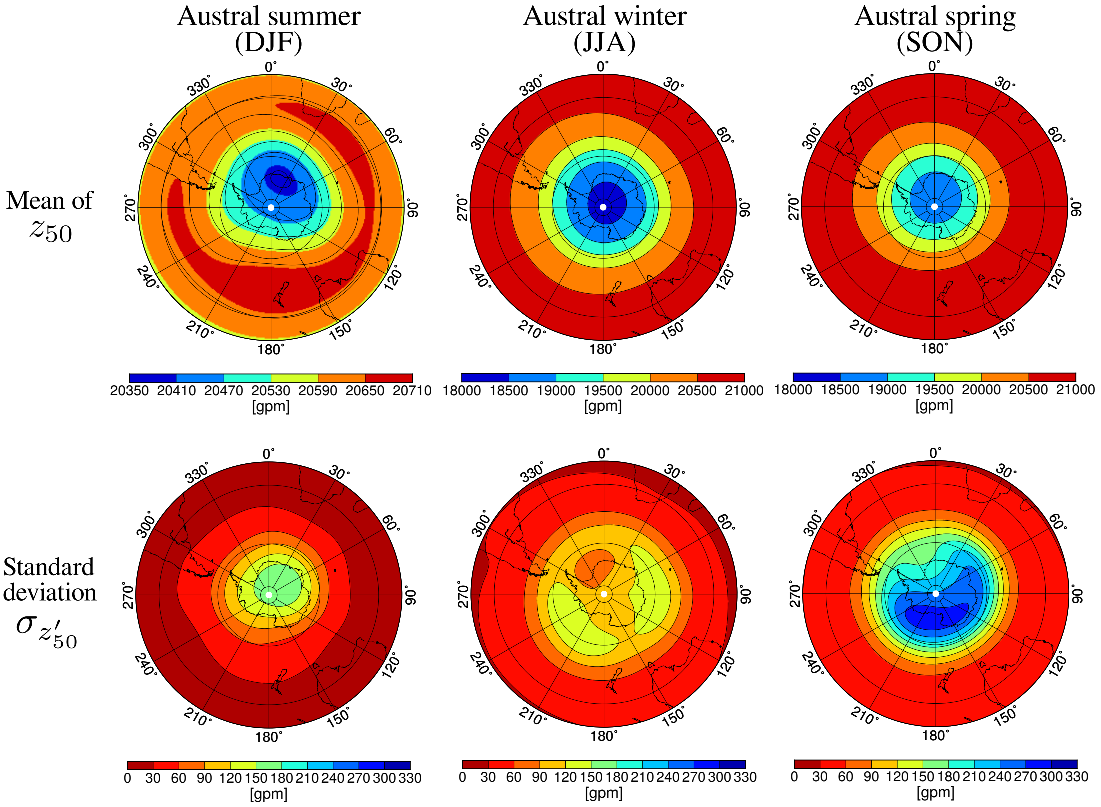
Austral summer (DJF)
Austral winter (JJA)
Austral spring (SON)
Mean of z_{50}
Standard deviation $\sigma_{z'_{50}}$
0°
30°
60°
90°
120°
150°
180°
210°
240°
270°
300°
330°
20350 20410 20470 20530 20590 20650 20710
18000 18500 19000 19500 20000 20500 21000
[gpm]
0 30 60 90 120 150 180 210 240 270 300 330

Figure 3.2: Same as in Figure 3.3, but for the 50 hPa level in the stratosphere. Austral spring (SON) is additionally shown in the right panel. Note the different scales in the mean plots.

Sea, whereas weaker amplitudes are recognised over East Antarctica. This center of action of interannual variability, which is more pronounced during austral winter time compared to austral summer, was also referred to as the "West Antarctic pole of variability" [Connolley, 1997]. Earlier studies suggest that this feature could result from the asymmetric nature of Antarctica's orography and its displaced centre of mass from the pole, which generates large-scale orographic Rossby waves contributing to the formation of this variability pattern [Lachlan-Cope et al., 2001]. The mean and variability patterns of austral spring SON (September, October, November) and austral autumn MAM (March, April, July) (not shown) reveal the same characteristics and spatial patterns with amplitudes lying between winter and summer season.

As in the troposphere, the stratospheric geopotential height field at 50 hPa[2] reveals a pronounced zonally symmetric decrease towards the pole (see Figure 3.2 (top)). As shown in Figure 3.2 (bottom), the polar vortex in austral winter and austral spring exhibits a considerable interannual variability. This year-to-year variability is especially pronounced in SON over southern polar regions and can mostly be attributed to variations in radiative heating induced by massive ozone-depletion in springtime (see Chapter 2.6.2). During austral summer, only a weak low pressure region and therefore weak westerlies are on average present over the polar cap.

---

[2] The 50 hPa pressure level was chosen as it is located in the midst of the ozone layer.

3.3 ANTARCTIC OSCILLATION IN REANALYSIS DATA

As described in Chapter B.1, Empirical Orthogonal Function (EOF) analysis computes the most efficient set of orthogonal basis functions, which explain a given fraction of variance of meteorological fields with a minimum of coefficients (Principal Components PCs). Therefore, EOF analysis has been extensively used as an aid in climatological studies especially to identify the most dominant patterns of atmospheric variability [Kidson et al., 1975; Wallace et al., 1981]. In this respect, it has been shown that EOF analysis serves as a useful tool for identifying and characterising atmospheric oscillation and teleconnection patterns around the globe—especially for geopotential height fields [Rogers et al., 1982; Thompson et al., 2000].

In order to examine the structure and the temporal evolution of the AAO for the time period 1979-2016, monthly ERA-Interim geopotential height anomaly fields of the 700 hPa (z'_{700}) and 50 hPa levels (z'_{50}) are used between 20°S and 88°S. This results in 6300 grid points for the interpolated $2 \times 2°$ grid resolution.

Due to the fact that grid points are equally spaced on a regular latitude-longitude grid, the number of grid points per unit area increases with higher latitudes as the meridians converge towards the poles. Therefore, high latitude features would be amplified and mid latitude features deemphasised. In order to remedy this inhomogeneous spatial distribution of data points, a common approach is to multiply each grid point by the square root of the cosine $\sqrt{\cos(\varphi)}$ of its respective latitude.

3.3.1 *Tropospheric Antarctic Oscillation*

The upper row in Figure 3.3 depicts the leading EOF of 700 hPa geopotential height anomalies z'_{700} and the respective 1st PC time series with unit variance and zero mean, which were calculated by including monthly values for all seasons. For examining seasonal differences, the analysis was additionally carried out by only considering monthly data of different seasons (DJF, MAM, JJA and SON). The fractions of variance (see Equation B.4), which are explained by the respective EOFs, vary between around 25 % (all seasons, MAM, SON) and over 30 % (DJF).

The structure of each leading z'_{700} EOF is a common definition of the tropospheric AAO. It reveals some kind of zonally symmetric ring-shaped pattern and can be associated with the direction in phase space, which explains most variance of the original z'_{700} time series. Thus, the patterns in Figure 3.3 can be interpreted in a way that positive geopotential height anomalies over mid latitudes are typically accompanied by negative anomalies over higher latitudes for months with a positive 1st PC (positive AAO phase). Contrary, negative geopotential height anomalies over mid latitudes are typically accompanied by positive anomalies over higher latitudes for months with a negative 1st PC (negative AAO phase). The 1st PC is therefore often referred to as a AAO-index (AAOI).

However, a closer investigation reveals that the tropospheric EOFs do not appear as complete zonally symmetric patterns. Especially in MAM, JJA and SON, three mid-latitudinal centres of action located in the stormtrack regions over the Pacific, Indian and Atlantic ocean can be observed, which resembles a wave-3 pattern of a stationary Rossby wave (see Chapter 2.4). In DJF the EOF pattern shows a more zonally symmetric shape in mid-latitudes. This may be at-

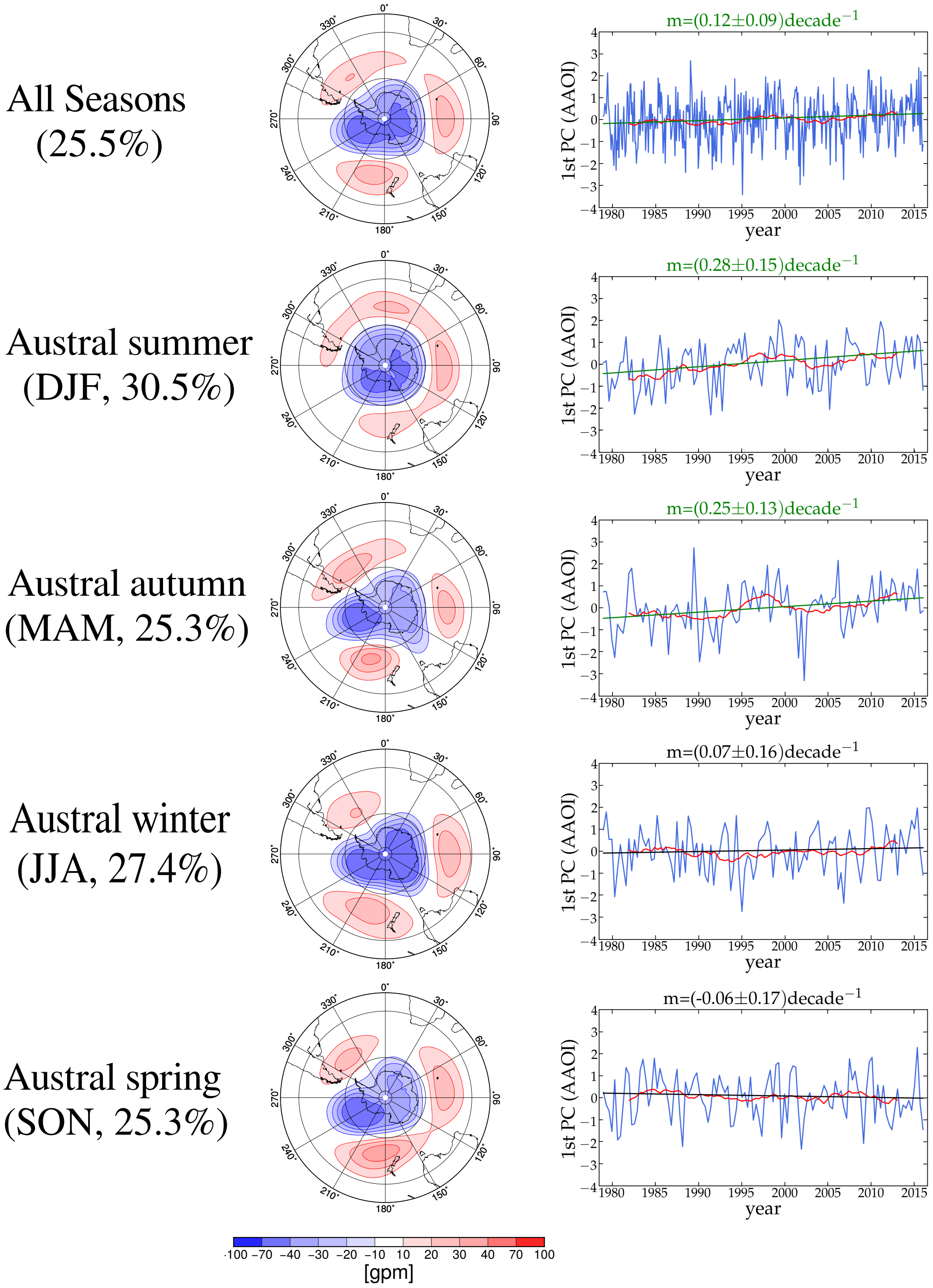

Figure 3.3: Leading EOFs (left), as well as the corresponding standardised 1st PC time series (right, blue curve) for different seasons computed from ERA-Interim 700 hPa geopotential height anomalies z'_{700} for the time period 1979-2016. Shown is also the percentage of explained variance in the left brackets. The patterns are normalised in such a way that the corresponding PC time series has unit variance. A linear trend line and a 6-year running mean (red) were calculated for each respective PC time series. The linear trend slopes and the repsective 95 % confidence intervals are given for each time series. For all seasons, DJF and MAM the significant trend slopes m are indicated by a green line color.

tributed to a less pronounced barcolinic wave activity in mid-latitude regions due to a weaker tropospheric meridional pole-equator temperature gradient and therefore less marked baroclinic stratification in austral summer. Additionally, a strong polar centre of action of the leading EOF pattern over Antarctica can be observed in austral winter, which is probably connected to variability of the stratospheric polar vortex.

By computing the Theil-Sen slope and the respective 95 % confidence intervals (see Chapter B.2), significant positive linear trends of the AAOI are detected during DJF and MAM over the last decades, which is in good agreement with previous studies [Fogt et al., 2009; Ding et al., 2012]. Especially the positive AAO trend in austral summer (DJF) is likely to be attributed to a delayed downward propagation of stratospheric signals induced by recent stratospheric ozone losses and the associated cooling in springtime [Thompson et al., 2002]. However, the precise mechanisms of this downward propagation are still under debate [Thompson et al., 2005]. The positive interannual linear trend for all seasons results from the contributions of the trends in DJF and MAM.

3.3.2 *Stratospheric Antarctic Oscillation*

Up to this point, the AAO has only been considered as a tropospheric variability pattern. Nevertheless, the fact that troposphere and stratosphere have shown to be coupled with each other motivates to analyse the dominant pattern of stratospheric variability as well, which for consistency might be termed the stratospheric AAO. For this reason, Figure 3.4 depicts the leading EOF and the respective 1st PC time series of geopotential height anomalies z'_{50} at the 50 hPa level. Obviously, the stratospheric geopotential height anomalies are predominantly characterised by variability patterns located over polar regions with largest amplitude in SON. These variability patterns can be associated with a dynamical strengthening or weakening of the stratospheric polar vortex in austral winter, late austral autumn and early/mid austral spring. Although the polar vortex is absent and stratospheric circulation is weakest in austral summer, a circumpolar variability pattern of z'_{50} can be observed over the polar cap. Since the amplitude of the stratospheric variability pattern in DJF (see Figure 3.4) is large enough to invert the mean equatorward pressure gradient in austral summer (see Figure 3.2 upper left panel), weak easterly winds levels might be present at certain times at the 50 hPa.

The observed higher amplitudes towards the pole are, on the one hand, in good agreement with the standard deviation plot in Figure 3.2; on the other hand, this might be at least partially a statistical artefact of the EOF calculation, as the average spatial correlation tends to increases towards the south pole at times when the polar vortex is present. Since EOF calculation aims to maximise the joint variability of all grid points, locations close to the poles may be emphasised; however Gerber et al., 2017 argued, that dynamical variability plays an important role for geopotential heights over polar regions, and results obtained from EOF analyses are not barely statistical artefacts (especially when analysing large-scale spatial domains). Due to smaller spatial correlation lengths compared to the stratosphere, such statistical effects are of minor concern in the troposphere but should always be borne in mind when interpreting EOFs as physical patterns of variability.

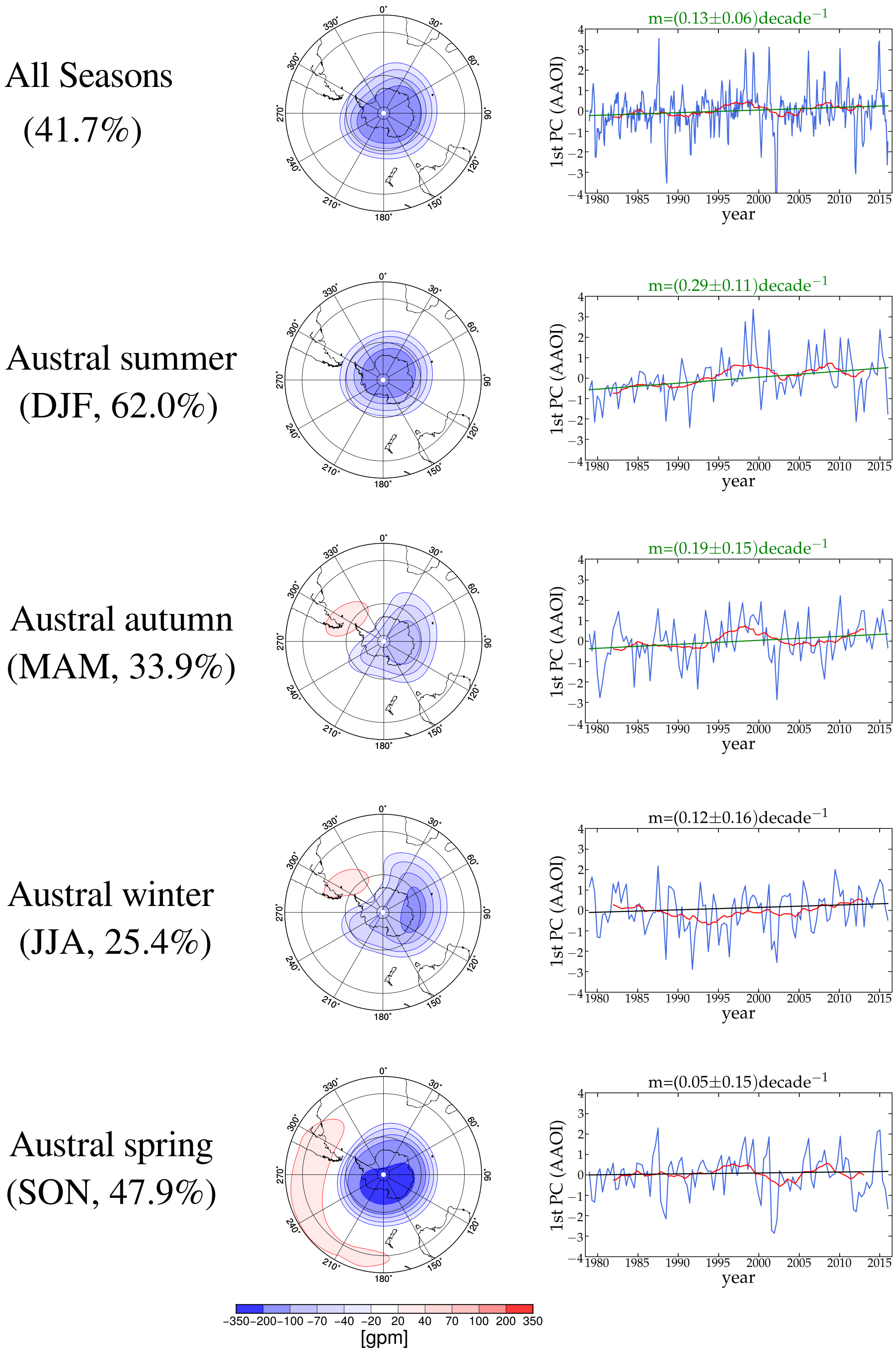

Figure 3.4: Same as in Figure 3.3, but for z'_{50} geopotential height anomalies.

For all seasons, in DJF and in SON, the variability pattern exhibits a symmetric shape around the pole. Contrary in MAM and JJA, more asymmetric patterns are present with shifted centres of action towards East Antarctica and the Southern Indian Ocean. In late austral autumn and austral winter (when the polar vortex is present), upward propagation of planetary waves is especially favored since westerlies are present in the troposphere and lower stratosphere up to a certain upper threshold (Charney-Drazin Equation 2.4). Therefore, the asymmetric shape of these variability patterns in austral winter and austral autumn might be attributed to upward propagation of planetary waves, which finally break into the stratosphere and distort the polar vortex.

In addition, a potential dipole pattern between Cape Horn and East Antarctica may be noted in MAM and JJA.

Both symmetric variability patterns in DJF and SON explain especially in austral summer up to 62 % of the entire seasonal variability. Contrary, the more complex and distorted patterns in MAM and JJA explain on average only up to 34% of variability.

Studying the associated leading PC time series shows an overall positive linear trend. On a seasonal scale, this tendency towards positive AAO polarities is significantly pronounced in DJF, when the stratospheric circulation is weakest, as well as in MAM. The strong trend in austral summer may reflect the thermal memory of the stratosphere, meaning that temperature anomalies induced by ozone losses in spring may affect and extend to the summer circulation [Thompson et al., 2002]. In this respect, trends in springtime loss depletion additionally prolong the existence of the polar vortex and consequently the period of ozone depletion (see Chapter 2.6.2). Overall, the impact of recent springtime ozone losses on the summer circulation might be enhanced over previous decades, which could potentially explain the observed upward trend in DJF.

It shows up that the tropospheric z'_{700} and stratospheric z'_{50} leading PC time series are highly correlated (correlation coefficient larger than 0.5 for each season). This underpins that tropospheric and stratospheric dynamics are linked to each other.

3.4 HIGHER ORDER PATTERNS OF VARIABILITY

Figure 3.5 shows the 2nd and 3rd EOF patterns of tropospheric and stratospheric geopotential height anomalies, respectively.

Although 2nd and 3rd tropospheric EOFs can explain comparable fractions of variance, all shown modes can be considered as statistically well separated from each other according to the criterion of North et al., 1982. Thus, the patterns are no mixtures of their respective true population counterparts. Due to statistical limitations such as the orthogonality constraint, there has been some debate to what extent especially higher EOFs can be interpreted as real physical modes of variability. For better physical interpretations, rotated EOFs are also sometimes used [Richman, 1986], which aim to identify simpler EOF structures at the expanse of alleviating the orthogonality constraint.

As shown in Figure 3.5 (left), the 2nd and 3rd tropospheric EOF patterns explain more than 20 % of the entire variance and resemble two out-of-phase wave trains extending over the South-

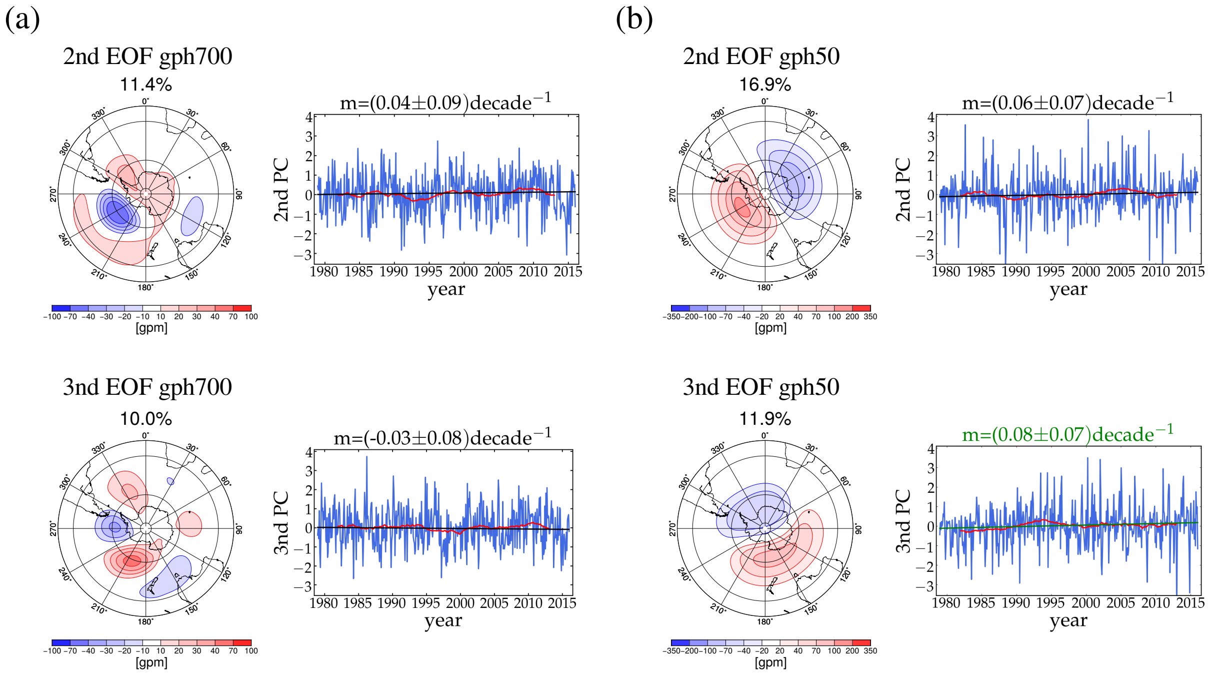

Figure 3.5: 2nd and 3rd EOF patterns and corresponding PC time series of (a) tropospheric z'_{700} and (b) stratospheric z'_{50} geopotential height anomalies. All seasons were pooled together before calculating the EOFs.

ern Pacific and Atlantic Ocean. These modes have been termed Pacific-South American (PSA) modes of variability and have been shown to be linked to ENSO, rainfall anomalies over South America, as well as to sea surface temperature anomalies in the tropics and the central and eastern Pacific [Mo et al., 2001]. In contrast to the AAO, no interannual linear trend over recent decades can be detected.

The higher stratospheric EOF modes in Figure 3.5 (right) reveal two wave-1 patterns and barely any significant linear trends. From a physical point of view, these patterns appear plausible since upward propagation of large-scale planetary waves with wavenumber $k = 1$ is generally favoured (see Equation 2.4); however, the relative rotation of both patterns by 90° with respect to each other sheds suspicion for the feature of being a statistical artefact due to the orthogonality constraint.

3.5 FREQUENCY ANALYSIS

In general, temporal climate variability can be considered as a combined result of internal dynamics and time-varying external forcings.

Internal variability is primarily a consequence of the strong nonlinear character of the entire climate system with each subsystem, such as the atmosphere, the ocean, the cryosphere or the biosphere, having its own characteristic time scale. Each of these climate system components is thereby potentially able to generate internal temporal variability, either by itself or by mutual

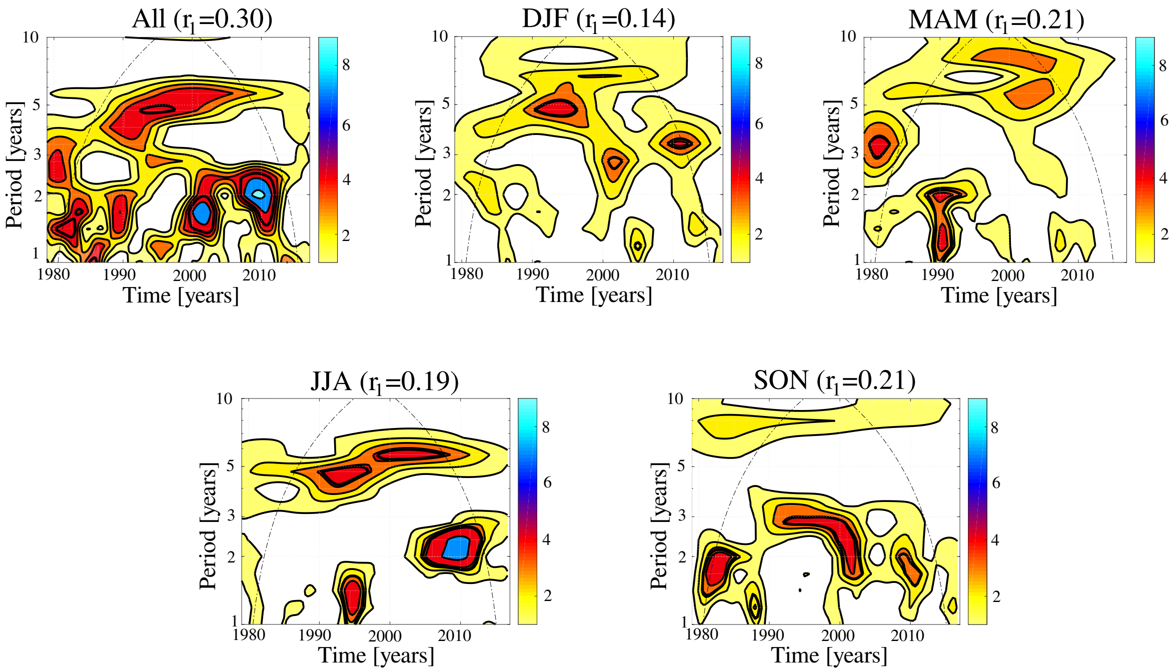

Figure 3.6: Wavelet Transform of the detrended z'_{700} leading PC time series for each respective season and for all seasons. The wavelet transforms show the spectral density in dependence on time and period. Spectral density values that lie outside the cone of influence (thin dashed line) are not considered to be reliable. Thick bold lines indicate regions, which lie outside the 95% confidence interval (ν=2 degrees of freedom) of the theoretical spectrum of a red noise process generated by an AR(1)-process (see Chapter B.3).

interactions with other subsystems due to nonlinearities in the involved physical processes and equations [Bauer et al., 2004].

External forcings are in general agreement considered to be the main sources of very low frequency variations. Atmospheric forcings include for instance variations of the incoming solar radiation during the 11-year solar cycle, changes in the atmospheric composition and in orbital parameters that mainly affect the Earth's energy budget. However the relative contribution of internal dynamics and external causes to atmospheric variability is still unclear and is predominantly examined and studied with climate model sensitivity experiments [Bracco et al., 2004].

Model studies based on atmospheric primitive-equation models, which were forced on timescales of the annual cycle, suggested that especially the interannual variability of large-scale patterns, such as the AAO, projects on a "red" spectrum with very-low frequency components dominating over higher intrannual components [James et al., 1989].

Further studies, which employed stochastic climate model approaches in connection with Fokker-Planck equation, obtained similar characteristic "red" spectra of variability [Hasselmann, 1976]. These studies considered low-frequency climate variability as a result of an integration of the rapidly varying atmospheric "weather" system by the slow-responding climate system (eg. ocean, cryosphere, vegetation...).

In order to investigate the temporal interannual variability of the AAO in more detail, the wavelet transform (see Chapter B.3) of the leading tropospheric (z'_{700}) PC times series (see Fig-

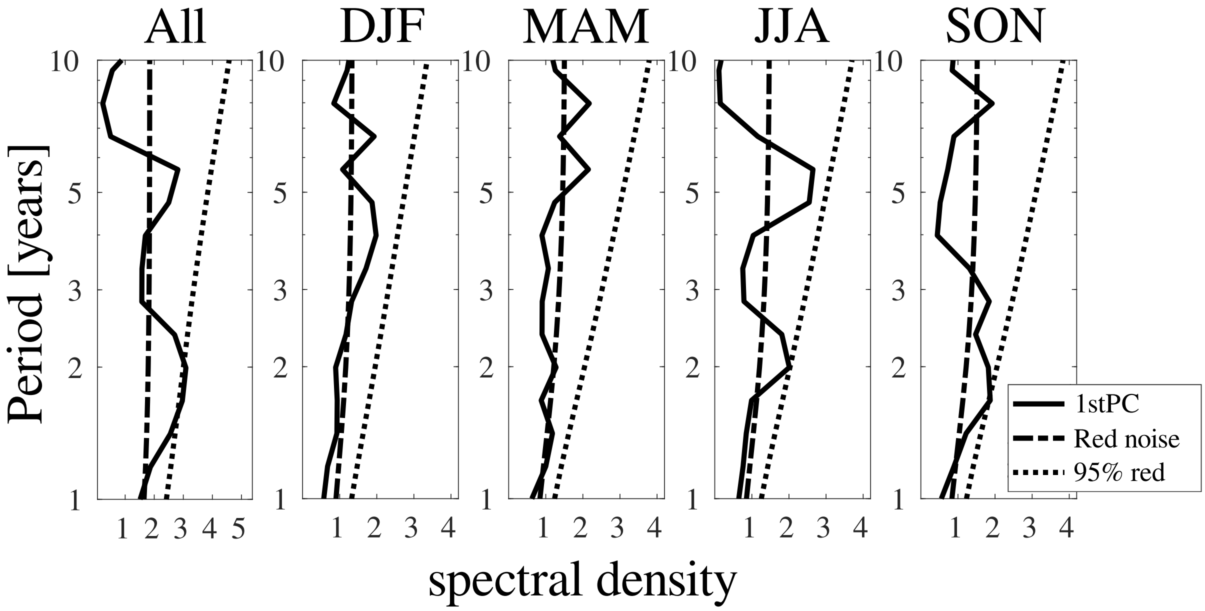

Figure 3.7: Global wavelet transform of the detrended z_{700} leading PC time series for each respective season and for all seasons, showing time averaged spectral densities. The dashed lines indicates the theoretical spectrum of an AR(1) process. The dotted lines signify the 95% confidence interval limits (degrees of freedom ν= length of time series n , see Chapter B.3).

ure 3.3) has been computed for each respective season by using a Morlet wavelet. All time series have been detrended beforehand and the resulting tropospheric wavelet transforms are depicted in Figure 3.6. Also shown are the lag-1 autocorrelation coefficients r_1 for each respective time series, which are overall small, but consistently positive.The lower lag-1 autocorrelation coefficient of the monthly-seasonal time series compared to the more continuous time series with all seasons is mainly due to the 9-month gap between seasons of two consecutive years.

Based on the positive lag-1 autocorrelation coefficient, the reference spectrum with which to compare the wavelet transform is chosen to be the theoretical "red" spectrum of a red-noise AR(1) process (see Equation B.10) with similar properties as the respective PC time series, such as same lag-1 autocorrelation r_1, variance σ_{PC} and zero mean. However, the wavelet transforms rarely reveal any regions in time and frequency domain that differ significantly from the reference spectral density. The only noteworthy and significant signals in the wavelet transforms appear especially in JJA for some years around 2010 with a period of two years and from 1990 to 2010 with a period of 5 years, as well as in SON in the 1990s and early 2000s with periods of 2–3 years.

Figure 3.7 illustrates the global wavelet spectrum, which is the time average of a certain frequency or period over the entire time interval and can be regarded and interpreted quite similar to a Fourier Transform. As noted before, the global spectra barely show any spectral densities at given frequencies that are unlikely to occur by chance in a corresponding AR(1) process.

In contrast to the troposphere, the AAO pattern in the less turbulent and more isolated stratosphere shows much stronger persistence. This is indicated by larger lag-1 autocorrelation coefficients with weakest persistence during austral summer and strongest persistence during austral spring (see Figure A.1). As already seen in the tropospheric wavelet analysis, the stratospheric wavelet plots lack significant signals as well, but generally show stronger signals on interannual frequencies due to the larger lag-1 autocorrelation. Significant signals show up in the beginning of the 2000s and around 1990 at periods of two years.

CLIMATE MODELS

4

Due to the huge complexity and nonlinearity of the climate system, it is almost impossible to study and to quantify future climate developments analytically, except for some few simplified and conceptual approaches and models. Along with the increasing computational power over the end of the 20th century, climate models became a popular tool allowing for more comprehensive studies of the climate system than ever before.

Basically, climate models may be considered as numerical representations of the governing physical equations. However, the corresponding set of partial differential equations can generally not be solved analytically. Therefore, climate models provide numerical solutions averaged over regions and time by discretising the spatial and temporal domain. The horizontal spatial resolution Δx ranges widely from some hundreds of metres in process models to the order of 100 km in global models and can be based on different grid types. The size of the time steps Δt typically range from minutes in short-term weather predictions to many years in paleoclimate simulations. However, higher resolutions in space and time are computationally more expensive and in order to ensure numerical stability of the model, Δt and Δx have to chosen according to certain criteria, which generally depend on the concrete numerical scheme.

Generally, the chosen complexity as well as the temporal and spatial resolution of the model strongly depends on the concrete scientific question. Energy balance models in their simplest form consider zonal or at least global energy budgets from emitted, absorbed and reflected solar or terrestrial radiation and allow for gaining insights into fundamental mechanisms, as for instance albedo feedbacks. On the next stage, earth models of intermediate complexity (EMICs) take into account more advanced and physical-based representations of dynamical processes and orography. Due to the advanced, but nevertheless often times still reduced and simplified representation of processes, EMICs require moderate computational resources and are suitable for tackling a huge variety of climate aspects, such as long-term paleoclimate simulations [Claussen et al., 2002]. On a final level, General Circulation Models (GCMs) provide the most precise representation of the climate system by numerically solving the full (but often times simplified) set of equations of motions at the expanse of higher computational costs. In addition to Atmospheric General Circulation Models and Sea-Ice-Ocean General Circulation Model, modern Earth System Models (ESMs) nowadays include complex and coupled descriptions of vegetation, ice sheets, carbon cycles or atmospheric chemistry as well.

4.1 ATMOSPHERIC GENERAL CIRCULATION MODELS

Atmospheric General Circulation Models (AGCMs) are essential components of ESMs and are nowadays widely used for numerical weather prediction and climate studies. Such models are basically constructed around a set of seven primitive equations, which were written down for the first time by the Norwegian meteorologist Vilhelm Bjerknes in the beginning of the 20th century. These equations mathematically represent physical conservation principles. Therefore, based on the corresponding basic physical laws they describe relationships between the seven primary atmospheric variables, which are three components of velocity, as well as pressure, temperature, air density and humidity. Some years after Bjerknes, Lewis Fry Richardson made the first attempt to predict weather numerically in detail. He discretised a region of interest into grid cells and formulated a discrete form of the governing equations on the grid. Richardson's famous imaginary description of a 'forecast factory', which should employ over 60,000 people manually solving the meteorological equations, is comparable to modern numerical weather prediction by parallel processing modern supercomputers. After the first computational numerical forecast with a one-dimensional model on the world's first electronic digital computer ENIAC in 1950, more sophisticated numerical forecasts became computationally realisable due to the steady increase in computational power. [Jacobson, 2005]

4.1.1 *Governing equations*

The dynamical core of AGCMs is governed by the following primitive equations in Eulerian form [Goosse et al., 2010]:

- the conservation of momentum is given by the *Navier-Stokes* equation:

$$\rho\underbrace{\left(\frac{\partial}{\partial t}+\vec{v}\nabla\vec{v}\right)}_{1} = -\underbrace{\nabla p}_{2}+\underbrace{\rho g}_{3}-\underbrace{2\rho\vec{\Omega}\times\vec{v}}_{4}+\underbrace{\vec{F}_{\text{ext}}}_{5} \tag{4.1}$$

  where $\vec{v} = (u, v, w)$ is the velocity vector, ρ is density, ∇p is the pressure gradient, g is the gravitational constant, Ω is the Earth's rotational velocity and $\vec{F}_{\text{ext}}$ describes all forms of frictional or external volume forces. Thus, the Navier-Stokes equations states the balance between inertia forces (1), pressure forces (2), gravity forces (3), Coriolis forces (4) and other forms of forces (5).

- the conservation of mass is described by the continuity equation:

$$\frac{\partial\rho}{\partial t} = -\nabla(\rho\vec{v}) \tag{4.2}$$

- and the conservation of energy may be given by an alternative formulation of the first law of thermodynamics:

$$\dot{Q} = C_{\text{p}}\frac{\text{d}T}{\text{d}t} - \frac{1}{\rho}\frac{\text{d}p}{\text{d}t}, \tag{4.3}$$

  where C_{p} is the specific heat capacity and $\dot{Q}$ is the heating rate per unit mass.

In combination with

- the equation of state for an ideal gas:

$$p = \rho RT \tag{4.4}$$

- and conservation of humidity q:

$$\frac{\partial \rho q}{\partial t} = -\nabla(\rho \vec{v} q) + \rho(\dot{E} - \dot{C}), \tag{4.5}$$

these seven equations form the basis for every AGCM, where R is the ideal gas constant, $\dot{E}$ and $\dot{C}$ are evaporation and condensation rates respectively.

A common assumption made in the third component of the Navier Stokes Equation 4.1 is the hydrostatic approximation

$$\frac{\partial p}{\partial z} = -\rho g, \tag{4.6}$$

which can be applied when vertical accelerations and therefore vertical inertia terms in Equation 4.1 are negligibly small compared to vertical gravity and pressure forces. This is typically the case when horizontal scales are large compared to vertical scales. In case vertical and horizontal scales are of similar magnitude, non-hydrostatic models (e.g. ICON) consider the entire vertical momentum equation and resolve non-hydrostatic motions.

Nevertheless, the dynamical equations given above do not form a closed system, since unknown quantities such as $\dot{E}$, $\dot{C}$,$\dot{Q}$ or $\vec{F}_{\text{ext}}$ have to be quantified that rely and are based on physical processes. The real climate system includes a huge variety of such underlying processes, which are often times less well understood or proceed on spatial and temporal scales smaller than the given model resolution. These processes include for instance atmospheric radiative transfer of shortwave and longwave radiation, microturbulence, cloud and sea-ice formation, as well as interactions and fluxes between different subsystem in coupled climate systems (e.g. air-sea fluxes of heat and moisture or wind drag forces on sea ice). In order to account for such processes in a simplified way, parametrisations have to be constructed and incorporated, which are based on empirical observations and physical understanding. Such parametrisations typically include large amounts of tuning parameters, which generally strongly depend on the model's resolution. In order to optimise these parametrisations, the included parameters are typically adjusted by using observational data [Hourdin et al., 2017].

4.1.2 *Coordinates and numerical schemes*

For numerically solving the previous nonlinear equations, the most straightforward approach is to discretise the Earth's surface into grid points as shown in Figure 4.1b. Generally, there exist different types of grids, such as regular latitude-longitude grids, triangular grids, icosahedral grids, as well as nested grids, which allow for higher resolutions in specific regions without expending computer resources in areas where coarser resolutions are sufficient.

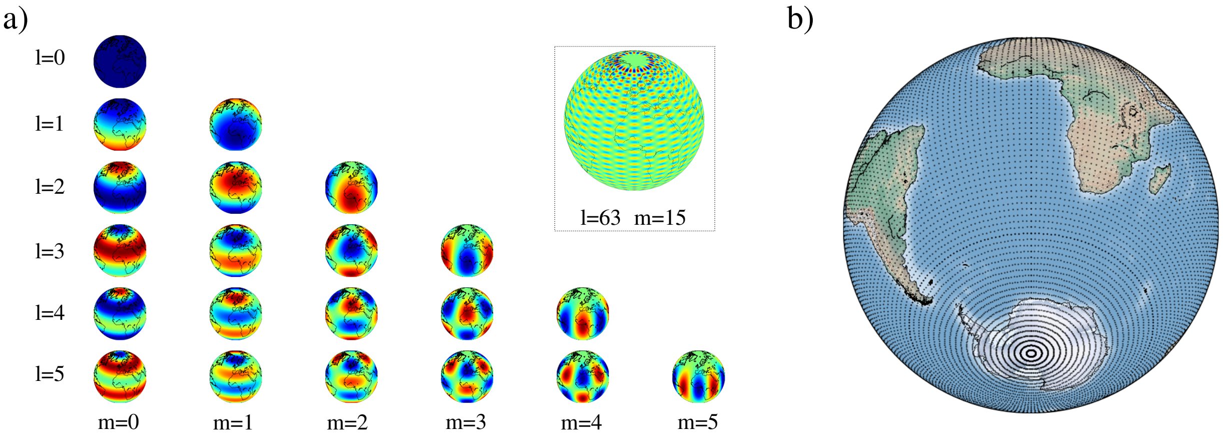

Figure 4.1: (a) Illustration of the spherical harmonics $\mathcal{Y}_{\mathrm{l,m}}$ employed as basis functions in global spectral atmospheric models. Shown is also a higher spherical harmonic (l=63, m=15) that contributes to the finest resolution details in ECHAM T63 trunctuation. (b) Quadratic gaussian N48 grid with 96 latitudes and 192 longitudes corresponding to a spectral T63 trunctuation.

The dominant and most intuitive approach for solving the equations of motion is the finite difference method, which approximates partial derivatives by differential quotients. In case of forward differences this has the general form

$$\frac{\partial X(x,t)}{\partial t} \rightarrow \frac{X_{\mathrm{j}}^{\mathrm{n+1}} - X_{\mathrm{j}}^{\mathrm{n}}}{\Delta t}, \tag{4.7}$$

$$\frac{\partial X(x,t)}{\partial x} \rightarrow \frac{X_{\mathrm{j+1}}^{\mathrm{n}} - X_{\mathrm{j}}^{\mathrm{n}}}{\Delta x}, \tag{4.8}$$

where $X_{\mathrm{j}}^{\mathrm{n}}$ is the value of the respective climatic variable at grid point j and time step n.

Modifications of this approach include for example backward or central finite differences that are computationally more demanding but numerically more stable and precise. As implemented for instance in the Finite Element Sea Ice-Ocean Model (FESOM), an alternative approach is given by the method of finite elements. This method utilises a set of basis functions that are nonzero inside a respective grid cell and zero elsewhere for solving the system of partial differential equations [Wang et al., 2014].

A different approach, which is frequently employed in global AGCMs spanning the entire global domain, is to transform the governing equations to spectral space [Silberman, 1954]. In this connection, a specific variable $X(\lambda, \varphi, \eta, t)$ might be expressed as a truncated series of spherical harmonics

$$X(\lambda, \varphi, \eta, t) = \sum_{\mathrm{l}=0}^{T} \sum_{\mathrm{m}=0}^{l} \psi_{\mathrm{l,m}}(\eta, t)\mathcal{Y}_{\mathrm{l,m}}(\lambda, \varphi) = \sum_{\mathrm{l}=0}^{T} \sum_{\mathrm{m}=0}^{l} \psi_{\mathrm{l,m}}(\eta, t) P_{\mathrm{l,m}}(\varphi) e^{im\lambda} \tag{4.9}$$

where λ is longitude, φ is latitude, η is height coordinate, T is the spectral truncation number, $\mathcal{Y}_{\mathrm{l,m}}$ are spherical harmonics shown in Figure 4.1a, $P_{\mathrm{l,m}}(\varphi)$ are associated Legendre Functions

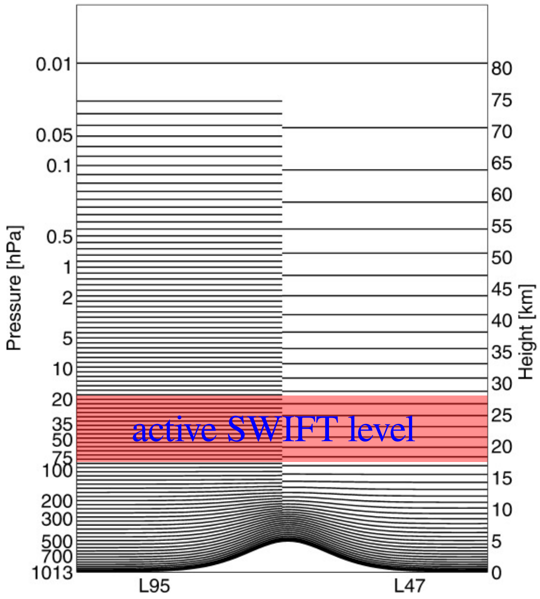

Figure 4.2: Illustration of the vertical pressure levels of a hybrid σ-pressure coordinate system over a mountain ridge with 500 hPa at the hilltop. Shown are the two available vertical resolutions in ECHAM6 (L47 and L95). The transition from a pure pressure coordinate system to a σ-coordinate system occurs approximately below 82 hPa. The red area signifies the altitude range in which SWIFT is active (picture taken and edited from [Schmidt et al., 2013]).

and m may be interpreted as a east-west wave number. The spectral coefficients $\psi_{\mathrm{l,m}}(\eta, t)$ can be obtained from the real grid point representations by first computing a Fast Fourier Transform in zonal direction followed by a Legendre transform in meridional direction. In order to ensure a highly accurate and efficient computation of the Legendre transform, a Gaussian grid is commonly chosen as a counterpart in physical grid space (see Figure 4.1b). For a quadratic Gaussian grid this corresponds to $N = \frac{4(T+1)}{3}$ nearly equally-spaced Gaussian quadrature latitudes between equator and pole, as well as $4N$ equally-spaced longitudes. The resolution in grid space is constrained by the spectral truncation number T corresponding to shortest wavelength in spectral space. In this respect, computational costs rise rapidly with increasing grid size, since forward and backward transforms have to be computed at each time step. However, a main advantage of calculations in spectral space is that spatial derivatives can be calculated exactly and the partial differential equations therefore reduce to ordinary differential equations. Especially the calculation of advection terms, which is time-expensive in real grid space, can be computed much more efficiently after a spectral transform [Machenhauer, 1979]. Therefore, spectral models compute most of the dynamical core Equations 4.1-4.5 in spherical harmonics space. Nevertheless, both representations, in grid space as well as in spectral space, generally have context-dependent computational benefits and disadvantages and may be used differently in various climate models.

In order to solve the partial differential equation system, sufficient and suitable boundary and initial conditions are necessary. For this reason, the temporal initial condition includes an initial state of the entire atmospheric system, and lower boundary conditions at each time step (e.g. SST, orography) need to be provided in the spatial domain when employing stand-alone atmospheric models.

Typical vertical height coordinates are geometric height z, pressure p or terrain-following σ-coordinate systems. In a hybrid σ-coordinate system, the vertical height levels coincide with the isobars in upper atmospheric regions, whereas in lower levels a σ-coordinate system is smoothly merged in. This ensures a terrain-following vertical coordinate system in lower tropospheric regions, as shown in Figure 4.2. The pressure $p_i(\lambda, \varphi)$ corresponding to the midpoint of the respective i-th vertical layer is given in such a hybrid σ-pressure system by

$$p_{\mathrm{i}}(\lambda, \varphi) = A_{\mathrm{i}} + B_{\mathrm{i}} p_{\mathrm{s}}(\lambda, \varphi),$$

where $p_{\mathrm{s}}(\lambda, \varphi)$ is the surface pressure at a given location [Stevens et al., 2013]. This results in pure σ-levels near the surface ($A_{\mathrm{i}} = 0, B_{\mathrm{i}} \lessapprox 1$) and pure pressure levels ($B_{\mathrm{i}} = 0$) at higher altitudes.

4.2 ECHAM

ECHAM is an AGCM developed by the Max-Planck-Institute for meteorology in Hamburg and is based on the dynamical core of a global forecast model from ECMWF [Stevens et al., 2013]. Since 1987, the original model was mostly extended and improved by including a variety physical parametrisations over time. As the previous versions, the latest version ECHAM6 consists of a mixed finite-difference/spectral discretisation of the underlying primitive equations (see Chapter 4.1.1) and employs a hybrid σ-pressure vertical coordinate system up to 0.01 hPa. Two vertical resolutions are available, one with 95 (L95) and one with 47 vertical levels (L47), where the L95 mode provides a finer vertical resolution in the upper troposphere and in the stratosphere enhancing the representation of vertical wave propagation. In this respect, different resolution setups have been tuned, such as a low resolution setup LR (T63/L47), a medium resolution setup MR (T63/L95) and a high resolution setup HR (T127/L95). The respective horizontal spectral trunctuations T127 and T63 correspond to associated Gaussian grids of approximately 1.9° and 0.95° resolution (see Figure 4.1b). Additionally, a semi-Lagrangian transport model on a Gaussian grid for tracers (e.g. chemical species) and certain scalar quantities is used. In this thesis, only data from the MR setup are analysed.

4.3 POLAR SWIFT

Most present climate models, such as many CMIP5 models, utilise prescribed ozone fields. However, these prescribed fields do not necessarily match the internal dynamics within the model. For example, there might be situations when values of the prescribed ozone fields that are normally associated with locations inside the polar vortex, are located outside the model-internal vortex due to vortex excursions. Moreover, using prescribed ozone does not allow for a realistic representation of feedback mechanisms between ozone and radiation/dynamics within the model, such as changes of chemical reaction rates due to temperature variations or enhanced ozone depletion on PSCs in a cooling stratosphere. Such insufficient representation of feedback mechanisms, as well as the misalignment between large-scale dynamical structures and the distribution of ozone, which acts as an important radiative forcing gas (see Chapter 2.6), may lead to an unrealistic representation of model-internal dynamics.

In order to overcome this typical deficiency of using prescribed ozone fields, chemistry climate models (CCMs) have been developed, which contain an integrated GCM and solve a huge set of hundreds of coupled differential equations for computing many chemical species (typically around 50). CCMs use input parameters (e.g. temperatures) from its integrated GCM in order to calculate the temporal evolution of several chemical species, which are afterwards returned back to the GCM in order to calculate radiative forcings. Nevertheless, due to the large amounts of variables and differential equations CCMs are generally computationally very expensive; consequently, they do not allow for many ensemble simulations.

Therefore, the fast chemistry model SWIFT has been invented, which simulates the stratospheric ozone chemistry with a simplified chemistry scheme and operates in ozone layer altitudes between 20–80 hPa (see Figure 4.2) with a time step of one day. Since SWIFT only considers the most essential processes involved in ozone chemistry, it is computationally less expensive compared to common CCMs. Generally, SWIFT consists of a polar [Rex et al., 2014; Wohltmann et al., 2017] and an extrapolar model [Kreyling et al., 2018]. For this study, only the polar model is used.

Polar SWIFT simulates the vortex-averaged mixing ratios of the key species involved in polar ozone depletion, that is O_3, HCl, HNO_3, $ClONO_2$ and ClO_x (see Chapter 2.6.2). A set of coupled differential equations representing these most important chemical processes is used to simulate the temporal evolution of the species within the polar vortex.

The model is driven by daily values of the fraction of vortex area that is cold enough to allow for the formation of PSCs (FAP), as well as the 24 h average of the fraction of the vortex that is illuminated by sunlight (FAS). SWIFT assumes that the change of vortex-averaged ozone mixing ratio O_3 is proportional to the amount of vortex-averaged mixing ratio of chemically-active chlorine $\langle[\mathrm{ClO_x}]\rangle$ and FAS

$$\frac{\mathrm{d}\langle[\mathrm{O_3}]\rangle}{\mathrm{d}t} = -d \cdot \langle[\mathrm{ClO_x}]\rangle \cdot \mathrm{FAS}.$$

d denotes a reaction rate coefficient, which is, along with several other reaction coefficients within the set of differential equations, fitted on five pressure levels to vortex-averaged reaction rate of the Lagrangian ATLAS Chemistry and Transport Model [Wohltmann et al., 2009].

On the SH, SWIFT is active from May until November and is initialised each May with climatological mixing ratios of the respective gases derived form ATLAS model runs and satellite measurements. In order to account for changes in the total amount of inorganic chlorine Cl_y over recent decades (e.g. due to CFC emissions), initialised mixing ratios of chlorine reservoir gases HCL and $ClONO_2$ are scaled over time. Outside the polar vortex transient climatologies containing monthly zonally averaged ozone fields [Cionni et al., 2011] are used, which rely on satellite observations and polar ozonesonde measurements.

The change of O_3 between two consecutive time steps due to transport by the Brewer-Dobson circulation is assumed to be proportional to a respective temperature difference ΔT (plus a constant term). This is motivated by the fact that warmer temperatures inside the polar vortex are associated with a stronger Brewer-Dobson circulation, which in turn strengthens the transport of ozone into the vortex. In order to ensure a realistic interaction between ozone fields and atmospheric dynamics, SWIFT was coupled to the AGCM ECHAM6.3 for the respective simulations used in this thesis (see Romanowsky et al., 2019). In this respect, temperature fields, as well as solar angles are passed from the atmospheric model to the SWIFT module.

4.4 MPI-ESM

The Max Planck Institute for Meteorology Earth System Model MPI-ESM [Giorgetta et al., 2013] is a completely coupled climate model, coupling the AGCM for the atmosphere ECHAM6 with the Global Ocean/Sea-Ice Model MPIOM. ECHAM is directly coupled to the terrestrial and biosphere model JSBACH, which considers physical and biogeochemical aspects of vegetation and soil. The ocean model MPIOM operates on a tripolar grid and is directly coupled to the marine biogeochemistry model HAMOCC5. All submodels are coupled via the OASIS3 coupler, which transfers fluxes of energy, water, momentum and CO_2 between the different subsystems and allows for instance for an interactive and realistic representation of the carbon cycle. Coupling between atmosphere-sea ice and atmosphere-land processes occurs on the atmospheric time step, whereas coupling of the ocean with atmosphere and land occurs once a day. When employing the MR-resolution setup, the ocean model operates on a $0.4°$ tripolar grid with a time step of 60 minutes, whereas the atmospheric model ECHAM operates with a time step of 7.5 minutes.

4.5 EVALUATION OF MODELS

In order to assess the capability of state-of-the-art climate models (especially that of the AGCM ECHAM) to simulate recent spatial and temporal characteristics of the AAO, data from different model setups are studied. Despite the fact that special focus is placed on including the interactive ozone chemistry model SWIFT, also coupled MPI-ESM runs are analysed. This allows for a better general assessment of the performance of contemporary climate models.

Therefore, data from four different model setups with differing ensemble sizes are studied in the upcoming evaluation:

1. **Three** stand-alone ECHAM6.1-MR ensemble runs for the period 1979–2008 taken from the Coupled Model Intercomparison Project phase 5 CMIP5 database. The ensemlbe simulations differ in the respective initial state only. These simulations follow the guideline of the Atmospheric Model Intercomparison Project AMIP [Taylor et al., 2012] and therefore use observed SST and SIE fields as boundary conditions. The analysed ensemble simulations are available from the CMIP5 archive (http://cmip-pcmdi.llnl.gov/cmip5/).

   Natural forcing includes changes in the Earth's orbit and variability in solar irradiance, as well as variations in natural tropospheric and stratospheric aerosols concentrations. Additionally, anthropogenic forcing is considered by using prescribed transient fields of well-mixed greenhouse gases CO_2, CH_4, N_2O and CFCs, as well as of time-varying monthly zonally averaged ozone fields [Cionni et al., 2011], which were already mentioned in

Chapter 4.3. ECHAM in MR-configuration operates with a time step of 7.5 minutes and with a spatial resolution of about 1.9°.

2. **One** stand-alone (CMIP5 AMIP-style) ECHAM6.3-MR run for the period 1979–2008 with same forcing and boundary conditions as in setup 1. Compared to ECHAM6.1, ECHAM6.3 includes some improvements in the cloud and radiation scheme. The run was performed by Daniel Kreyling at the Alfred Wegener Institute in Potsdam.

3. **Three** stand-alone (CMIP5 AMIP-style) ensemble runs of ECHAM6.3-MR coupled to SWIFT for the period 1979–2008. The same forcing and boundary conditions are used as in setup 1. The runs were performed by Daniel Kreyling at the Alfred Wegener Institute in Potsdam.

4. **Three** ensemble runs of the MPI-ESM for the period 1979–2005 in MR-resolution setup. ECHAM6.1-MR used as the atmospheric component. The data are taken from the CMIP5 database and follow the respective CMIP5 guidelines for the historical simulations [Taylor et al., 2012]. The same natural and anthropogenic forcings are used as in setup 1. For the years 2005–2016, the data are complemented with data from the completely RCP45 scenario runs, which continue the three realisations of the historical simulation for the time period 2005–2100, assuming an additional radiative forcing of 4.5 $\frac{W}{m^2}$ in 2100 compared to preindustrial times. The analysed ensemble simulations are available from the CMIP5 archive (http://cmip-pcmdi.llnl.gov/cmip5/).

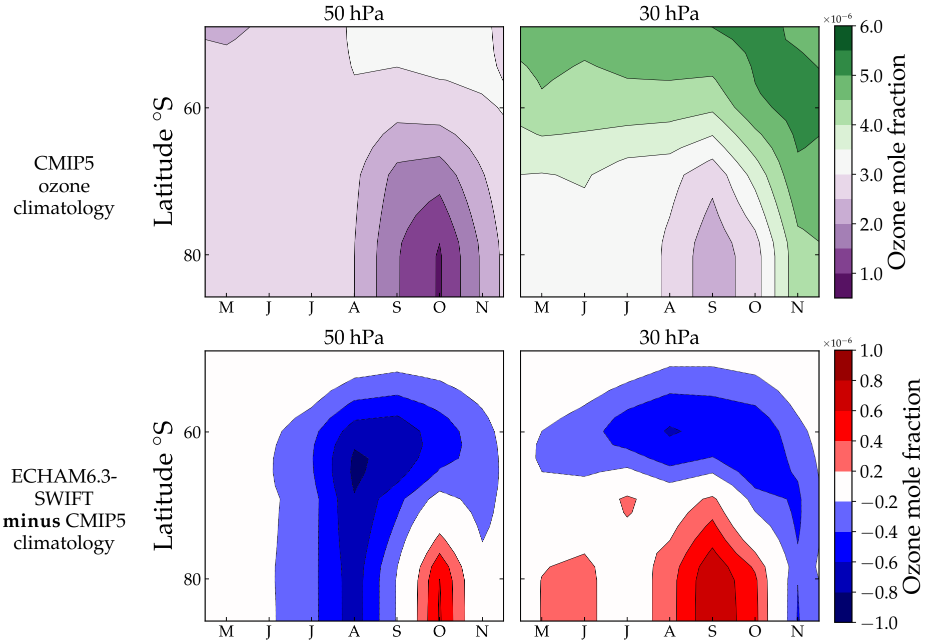

Figure 4.3: Upper row: zonally averaged ozone mole fractions for various months, calculated from monthly CMIP5 ozone climatologies over the period 1979–2008. Shown are plots for two stratospheric SWIFT-levels (left 50 hPa, right 30 hPa). Bottom row: Differences in zonally averaged ozone mole ratios calculated by subtracting the climatology from the ensemble mean of the ECHAM6.3+SWIFT runs.

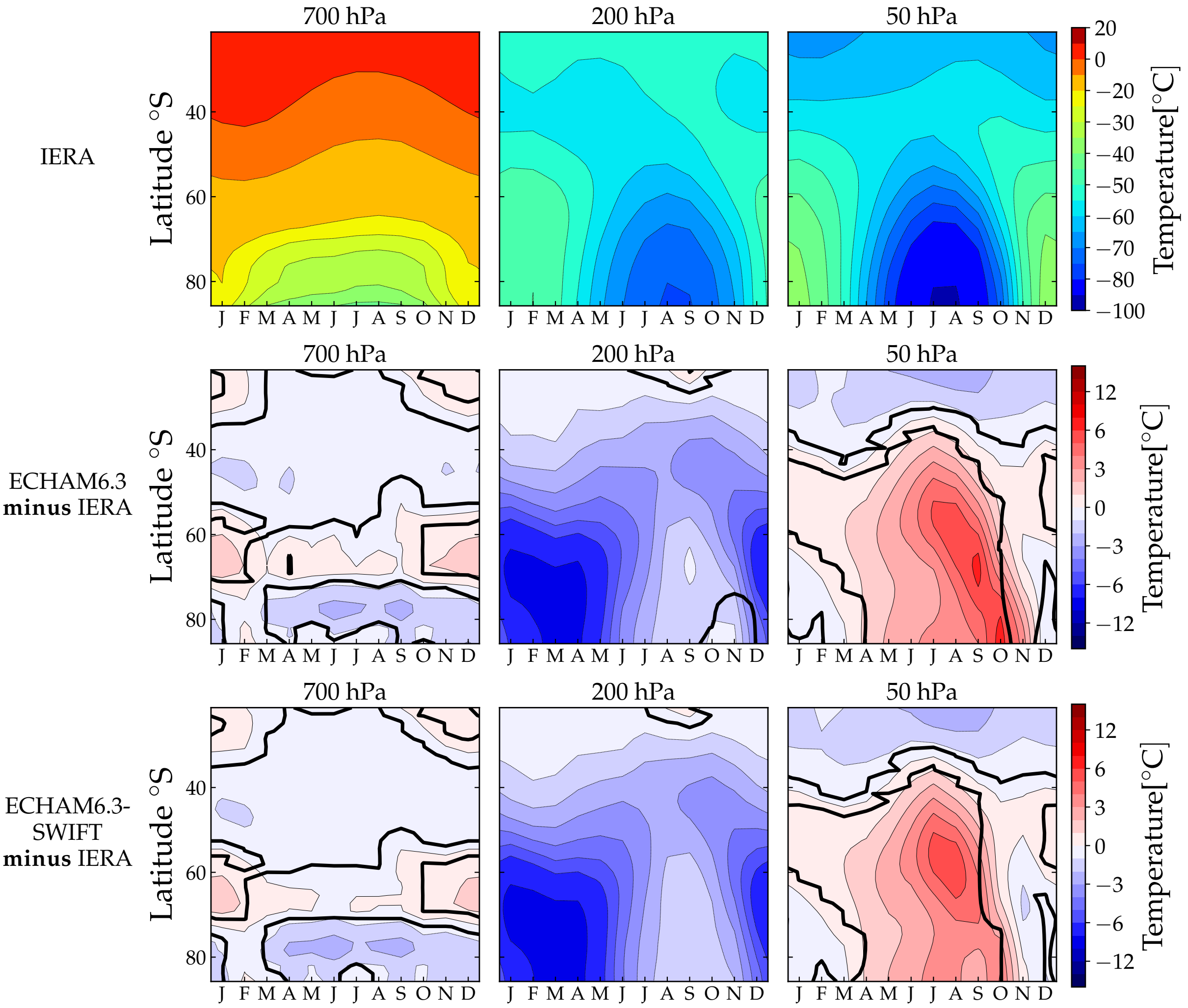

Figure 4.4: Zonally averaged temperatures for various months calculated from monthly ERA-Interim temperature data over the period 1979–2008 (upper row). Shown are plots for the lower troposphere (700 hPa, left), the upper troposphere (200 hPa, middle) and the stratosphere (50 hPa, right). The respective bias plots are computed by subtracting ERA-Interim from the ECHAM6.3 run (middle row) and from the ensemble mean of the ECHAM6.3+SWIFT runs (bottom row). Thick black lines indicate regions were 95 % confidence intervals of the bias, which were computed based on the interannual variability of the time series, do not include a zero bias.

4.5.1 *General assessment of ECHAM-SWIFT*

As mentioned in the very beginning, special focus is on the coupled ECHAM-SWIFT model setup (see Chapter 4.5 setup 3). For this reason it will be first analysed, whether including the interactive ozone module SWIFT to ECHAM6.3 has positive effects on correcting ECHAM-biases in temperature and zonal wind.

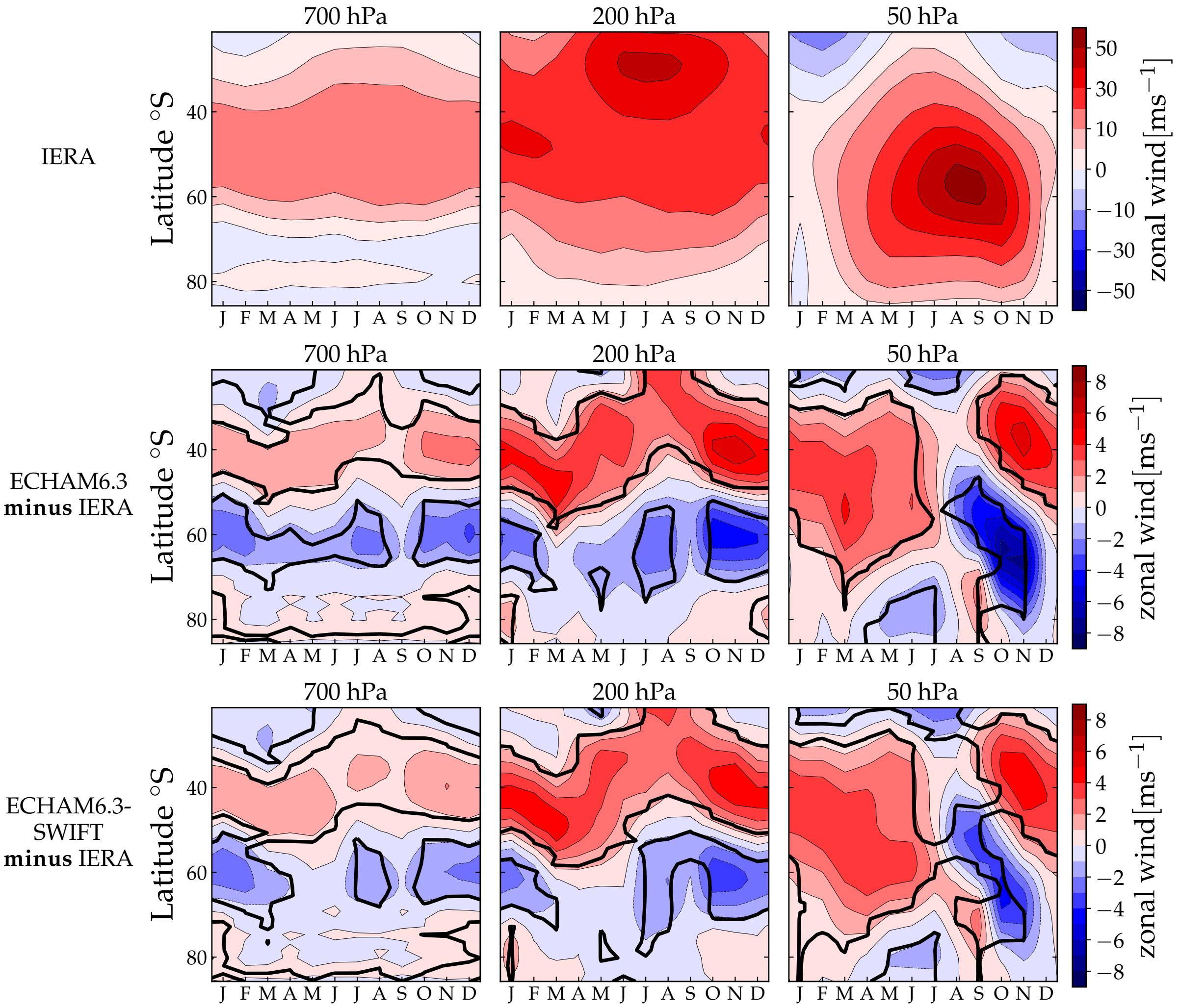

Figure 4.5: Same as in Figure 4.4, but for zonal wind.

However to start with, Figure 4.3 illustrates differences in zonally averaged ozone mole ratios between ECHAM6.3-SWIFT and the zonally averaged CMIP5 ozone climatology used in the other model setups. Shown are plots for various seasons at the 50 hPa and 30 hPa pressure levels, which are located in the SWIFT-active altitude range (see Figure 4.2).

Obviously, the zonally averaged amount of ozone in mid-latitudinal regions is generally underestimated by the SWIFT simulations compared to the climatology. Contrary in late austral summer and austral spring, ozone mixing ratios over polar regions at 30 hPa exceed those in the climatology. This discrepancy between polar and mid-latitude regions could be attributed to asymmetries of the vortex, as excursions of an unstable polar vortex are generally associated with warmer temperatures and therefore higher vortex-averaged ozone amounts. Additionally, the parametrisation of the ozone transport by the Brewer-Dobson circulation might transport too much ozone into the polar vortex during austral spring.

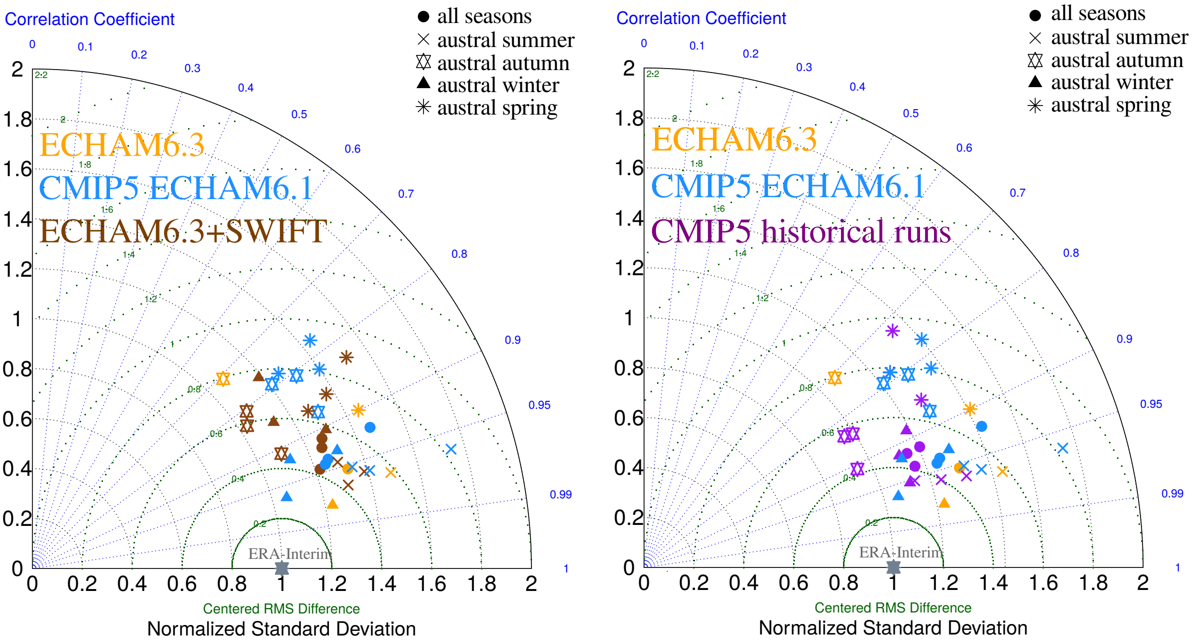

Figure 4.6: Taylor diagram (see Appendix B.4) for the leading EOF patterns computed from geopotential height anomalies z'_{700} at the 700 hPa pressure level. Left: stand-alone atmosphere runs ECHAM6.1/6.3 and ECHAM6.3-SWIFT (setups 1,2,3). Right: coupled MPI-ESM-MR runs and stand-alone atmosphere runs ECHAM6.1/6.3 (setups 1,2,4). Different colors indicate different model setups and different symbols signify different seasons.

Figure 4.4 indicates a slight reduction in temperature biases during austral spring season (where SWIFT is active) in polar stratospheric regions at 50 hPa when using ECHAM6.1 coupled to SWIFT instead of ECHAM6.3 stand-alone (see Chapter 4.5 setup 2). This bias reduction can however hardly be termed significant due to the strong interannual variability in this season. This is indeed quite surprising, since SWIFT tends to yield on average too much ozone in austral spring over polar regions (see Figure 4.3) and these larger ozone abundances would normally contribute to an additional heating of the stratosphere. The strong negative temperature bias of ECHAM6.3 near the tropopause is not affected by SWIFT.

As shown in Figure 4.5, biases of tropospheric zonal winds seem to be unaffected by SWIFT as well. Nevertheless, a reduction of the easterly zonal wind bias can be observed during austral spring in the stratosphere when coupling SWIFT to ECHAM. This is in good agreement with the temperature bias reduction in polar regions during this season (see Figure 4.4) that increases the meridional temperature gradient between mid- and high-latitudes and therefore contributes to a westward shift of the mean zonal wind.

4.5.2 *Simulated Antarctic Oscillation patterns*

This section compares the AAO patterns calculated from the model simulations with the reanalysis pattern. For this reason, Figures 4.6 and 4.7 show the respective Taylor diagrams (see Appendix B.4). The leading EOF and the corresponding 1st PC times series for the different model

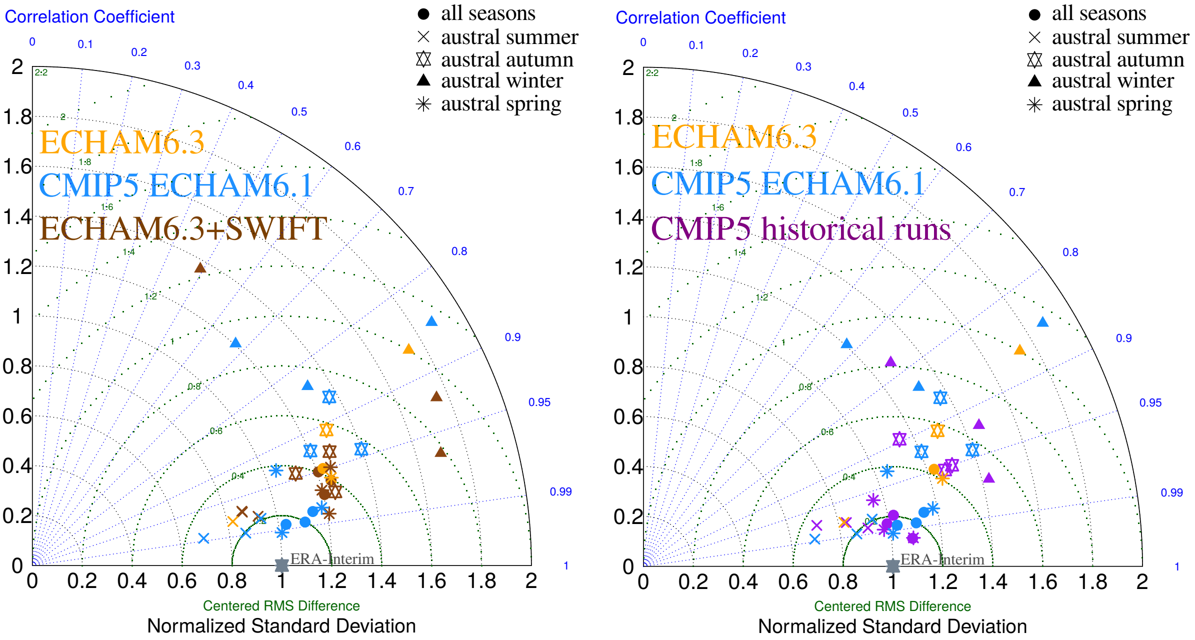

Figure 4.7: Same as in Figure 4.6, but for the leading EOF patterns calculated from geopotential height anomalies z'_{50} of the 50 hPa pressure level.

simulations were calculated for geopotential height anomaly fields (z'_{700} and z'_{50}) according to the same procedure already applied in Chapter 3.3.

Figure 4.6 depicts a Taylor diagram that compares the leading tropospheric (z'_{700}) EOF model patterns with the reference reanalysis pattern. The corresponding tropospheric patterns for each respective model run are shown in Appendix A.2. As it can be noticed in Appendix A.2, the main reason for the reduced model correlation coefficient in the Taylor diagram 4.6 mostly stems from the models' deficiency in simulating the mid-latitudinal centres of action. Moreover, the models tend to produce too zonally symmetric variability patterns in the mid-latitudes compared to the reanalysis. Additionally, the tropospheric pole of variability over Ross and Amundsen Sea, which is observed in the reanalysis pattern in MAM and SON, is mostly absent in the model simulations. This leads to less similarity between tropospheric model and reanalysis pattern in austral autumn and austral spring compared to other seasons. Generally, the models tend to overestimate the explained variance, as well as the dynamical amplitude (pattern standard deviation) of the tropospheric AAO. Especially the polar centre of action is more pronounced compared to the reanalysis.

Figure 4.7 shows the Taylor diagram for comparing the model-based stratospheric (z'_{50}) leading EOF pattern with the reference reanalysis pattern. The corresponding stratospheric patterns for each respective model run are shown in Appendix A.3. Obviously, all model setups reveal problems in reproducing the asymmetric and wave-distorted variability pattern in MAM and JJA (see Appendix A.3). This is indicated by the reduced pattern correlation coefficients in the Taylor diagram. Nevertheless, a closer investigation of the model patterns in MAM and JJA (see Appendix A.3) shows that the models basically simulate the distorted variability pattern, however arbitrarily rotated around the pole by up to 90°. This may indicate an insufficient repre-

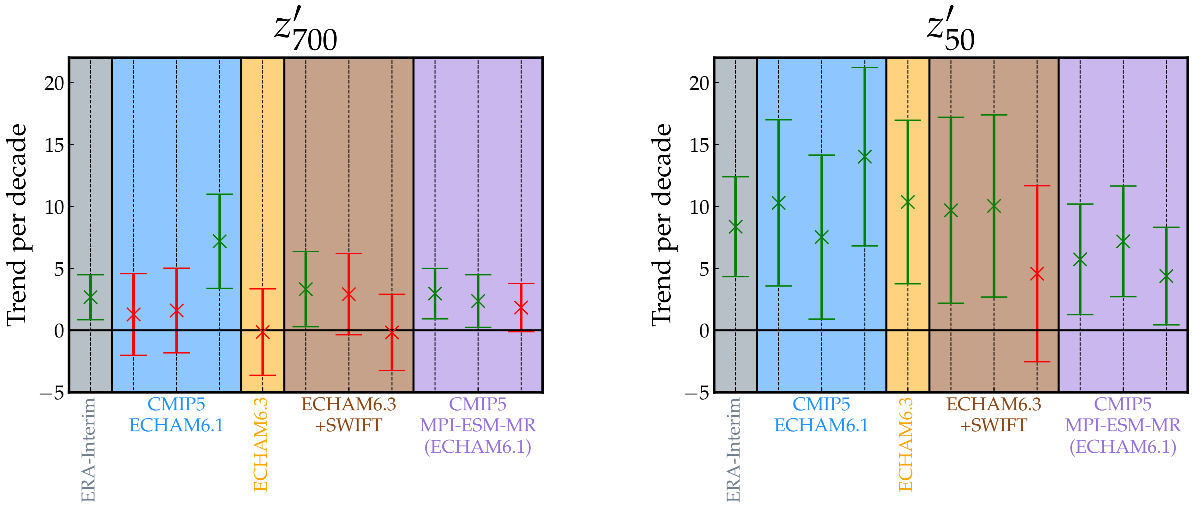

Figure 4.8: Summary of simulated trends of the standardised AAOI time series from different model simulation for all seasons. The standardised AAOI time series and the respective confidence intervals were calculated according to the same procedure applied in Chapter 3.3. Green errobars indicate significant trends when the respective errorbar does not cross the zero line. Red errorbars signify non-significant trends. In order to additionally account for the actual strength of the model trends, the original standardised leading PC time series were multiplied by the respective pattern standard deviation before estimating trend slopes and confidence intervals. The corresponding standardised time series are shown in Appendix A.2 and A.3.

sentation of vertical wave propagation and troposphere-stratosphere coupling processes within the models. As it can be derived from Figure 4.5, no significant turns from westerly to easterly winds, which would potentially reflect or suppress vertical wave propagation (see Equation 2.4), are observed in the model simulations in the lower atmosphere during MAM and JJA. Generally, the symmetric stratospheric patterns in DJF and SON are on average better reproduced by the models than the asymmetric patterns in JJA and MAM. The suggested dipole pattern between Cape Horn and East Antarctica in MAM (see Chapter 3.3.2) is consistently simulated by the models. This motivates a real physical mechanism beyond this observed pattern, instead of barely being a statistical artefact. With the exception of austral summer, the models generally tend to overestimate the stratospheric patterns' standard deviations. This could be linked to the positive stratospheric temperature biases in MAM, JJA and SON (see Figure 4.4). During theses seasons, overestimated stratospheric temperatures in the models can generally be associated with an overall weaker, and therefore less stable polar vortex, which might exhibit larger variability between different years.

Overall, it is hard to identify any clear differences between different model setups, especially due to the relatively large spread between different ensemble simulations. As the tropospheric AAO is an inherent feature of atmospheric dynamics (see Chapter 2.7.2), the fully coupled MPI-ESM runs do not show any significant improvements in the troposphere, but neither in the stratosphere as well. Aiming to improve the interaction between stratospheric chemical processes and dynamics by including SWIFT does not show any enhancements in simulating the spatial patterns of variability.

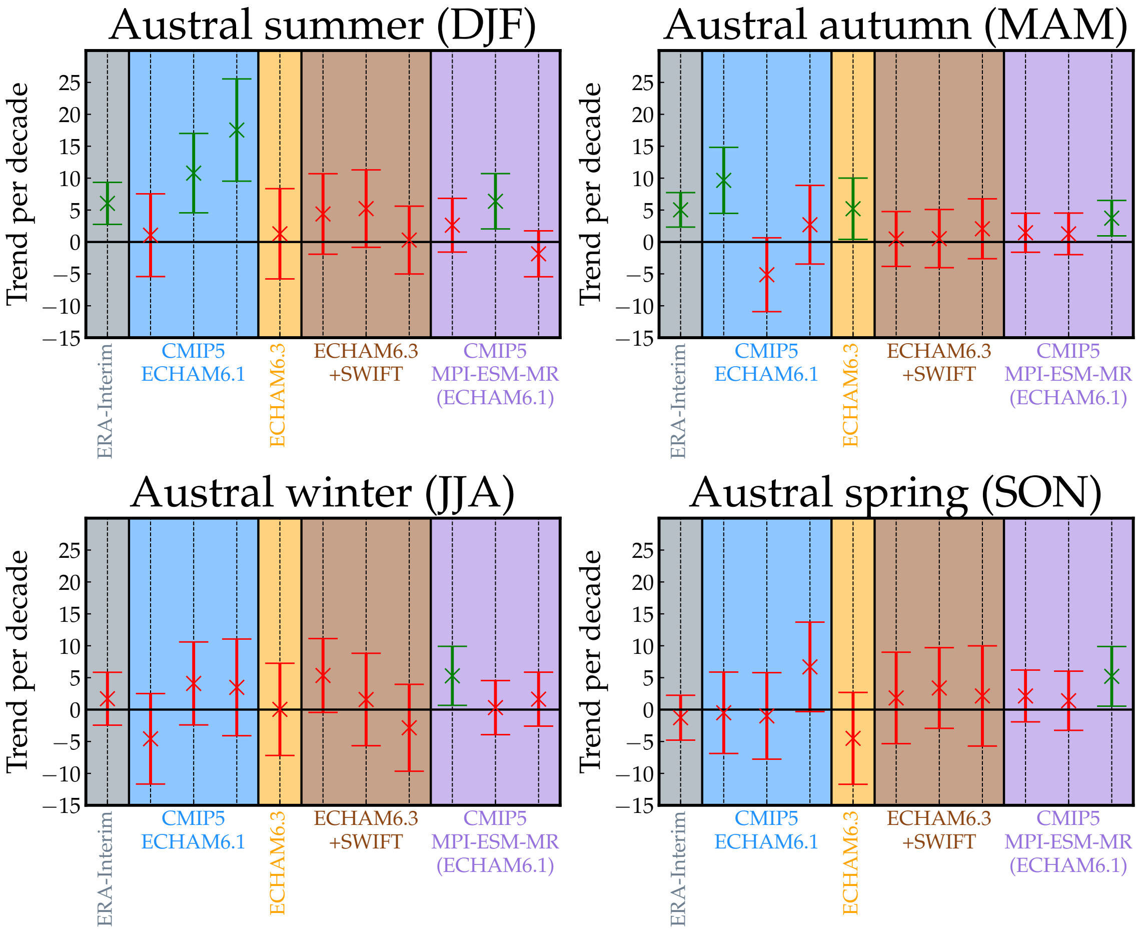

Figure 4.9: Same as in Figure 4.8, but only for z'_{700} and for different seasons. The corresponding standardised 1st PC time series are shown in Appendix A.2.

4.5.3 *Simulated Antarctic Oscillation trends*

In this section, the long-term progressions of the leading PC time series estimated by linear trend analysis are summarised for the model simulations (see Figures 4.8–4.10). Since only up to three ensemble members were available for each respective model setup, the trend and the respective confidence intervals were calculated according to Appendix B.2 for each ensemble member individually, instead of taking ensemble means. In order to additionally account for the actual strength of the model trends, the original standardised leading PC time series were multiplied by the respective pattern's standard deviation before estimating linear trend slopes and confidence intervals. The corresponding standardised leading PC time series of each respective ensemble run are shown in Appendix A.2 and A.3.

Figure 4.8 summarises the linear trends of the AAOI for z'_{700} and z'_{50} in case where all season were pooled together before applying the EOF analysis. Obviously, the positive tropospheric linear trend over recent decades observed in the ERA-Interim data is reproduced by less than 50 % of the model runs. Due to the large spread between different ensemble members, no pre-

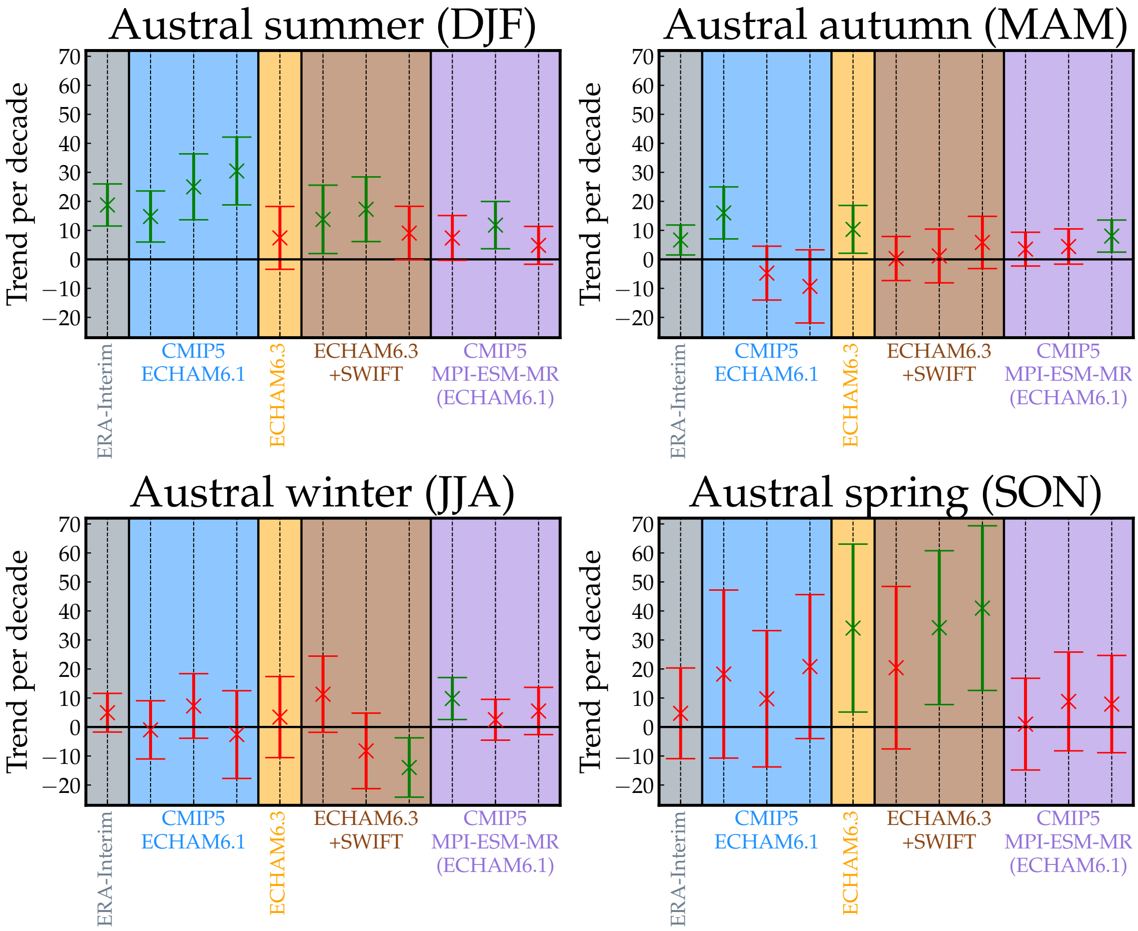

Figure 4.10: Same as in Figure 4.8, but for z'_{50} The corresponding standardised 1st PC time series are shown in Appendix A.3.

ferred model setup is identifiable that simulates the observed positive tropospheric AAO trend consistently. Contrary, the observed positive trend in the stratosphere is simulated by nearly all simulations. Compared to the reanalysis, the stand-alone atmosphere runs tend to overestimate the strength of the linear stratospheric trend, whereas the coupled MPI-ESM simulations rather underestimate the observed trend. Especially SWIFT does not show any enhancements in simulating recent long-term progressions of the tropospheric AAO, which were expected due to potential improvements in troposphere-stratospheric interactions when including interactive ozone chemistry.

The summary of seasonal tropospheric AAOI trends in Figure 4.9 shows that the models are generally not able to reproduce the observed tropospheric trends in DJF and MAM. Only three model runs significantly simulate the observed positive linear trends respectively, and the spread between different ensemble members is large. In accordance with the reanalysis data nearly all model simulations do not produce significant unrealistic AAO trends in JJA and SON.

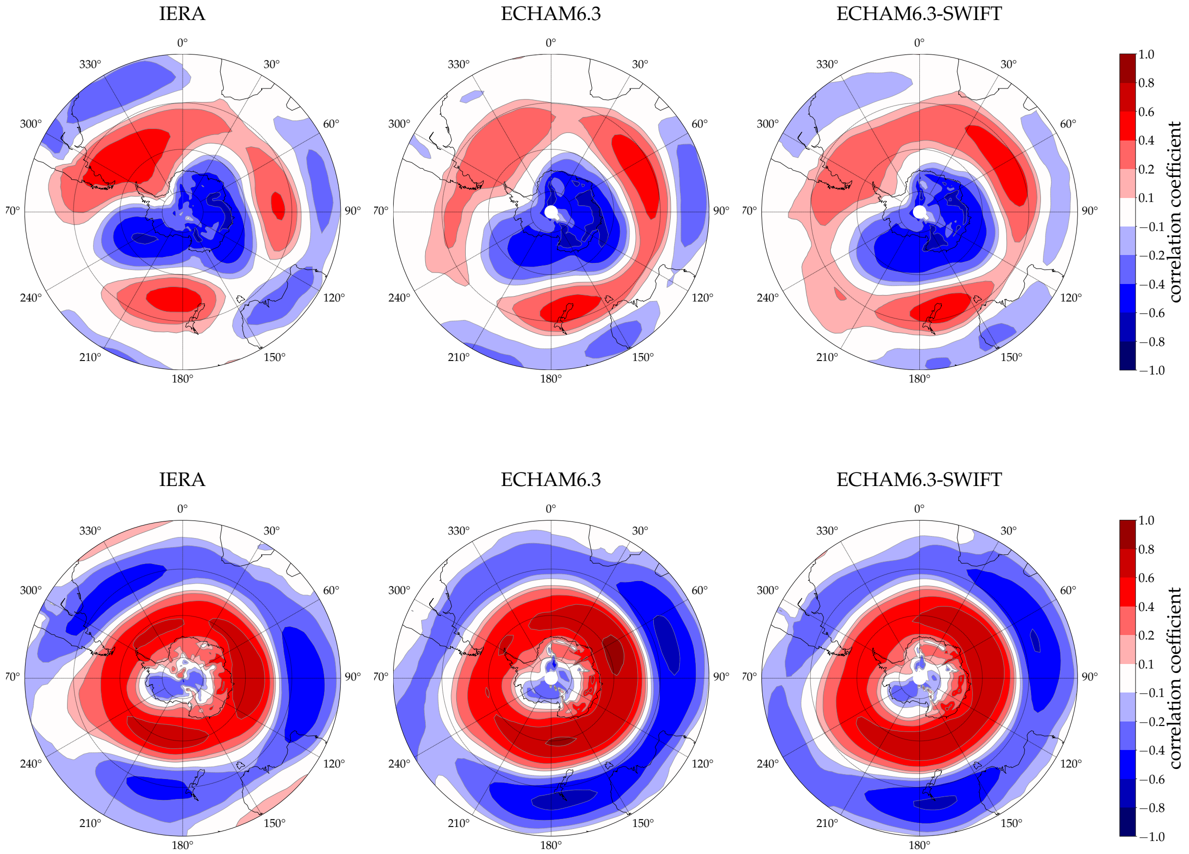
IERA ECHAM6.3 ECHAM6.3-SWIFT

IERA ECHAM6.3 ECHAM6.3-SWIFT

Figure 4.11: Correlation map between the tropospheric (z'_{700}) leading PC time series and monthly mean temperature anomalies T'_{700} (upper row) and zonal wind anomalies u'_{700} (bottom row) at 700 hPa for ERA-Interim, ECHAM6.3 and ECHAM6.3-SWIFT. All time series have been linearly detrended before computing the correlation.

As shown in Figure 4.10, the stratospheric positive trend in DJF is reproduced in more than half of the model simulations, whereas a significant trend in MAM is mostly absent. This may show that the models are capable to simulate the time-delayed impacts of recent springtime ozone losses on the stratospheric summer circulation very well (see Chapter 3.3.2).

However, that the models are overall able to reproduce recent stratospheric, but no tropospheric trends in austral summer indicates a potential deficiency in representing troposphere-stratosphere interactions realistically.

4.5.4 *Correlation maps*

In order to finally study the model-internal alignment between the tropospheric AAO and other climatic fields, Figure 4.11 depicts correlation maps between the leading PC time series and temperature anomalies T'_{700}, as well as zonal wind anomalies u'_{700} at 700 hPa, respectively. The shown correlation maps for ERA-Interim, ECHAM6.3 and ECHAM6.3-SWIFT considered all months of a year.

The ERA-Interim T'_{700} correlation map shown in Figure 4.11 (top) indicates a cooling over Antarctica and a warming over the oceans in mid-latitudinal regions in association with a positive AAO phase, which was already noted in Chapter 2.7.1. The correlation pattern strongly resembles the shape of the corresponding leading EOF pattern. The ECHAM6.3 and ECHAM6.3-SWIFT model simulations basically reproduce the reanalysis correlation pattern, with more symmetric shapes in mid-latitudes however. The shift of the westerly wind belt towards Antarctica associated with a positive AAO phase in the reanalysis data, is consistently present in the chosen model simulations as well (see Figure 4.11 (bottom))

In conclusion this motivates that the large-scale pattern of the AAO in model simulations may be used as a potential predictor for different climate variables in order to assess future climate change.

5

CONCLUSION AND OUTLOOK

This thesis examined characteristics of the tropospheric and stratospheric Antarctic Oscillation (AAO) in reanalysis and climate model data, such as recent trends, its spatial patterns and interannual variability.

In Chapter 3.3, the method of Empirical Orthogonal Function (EOF) was applied to ERA-Interim geopotential height anomaly fields in order to study the dominant pattern of extratropical atmospheric variability over the SH. In this respect, analysis of ERA-Interim tropospheric z'_{700} anomaly fields showed that the AAO is characterised by a see-saw of pressure anomalies between mid- and high-latitudes. However, the associated EOF patterns were characterised by zonal asymmetries in mid-latitudes. In accordance with previous studies [Fogt et al., 2009; Ding et al., 2012], an overall trend towards more positive AAO polarities could be detected by analysing the respective leading tropospheric PC time series. On seasonal time scales, these positive trends were significantly pronounced in austral summer and austral autumn. In austral summer this trend might be attributed to the time-delayed downward propagation of stratospheric signals induced by springtime ozone loss. As stated in Chapter 2.7.1, variations in the tropospheric AAO polarity are strongly related to meridional shifts of the westerly wind belt, regional cooling and warming, meridional heat fluxes, as well as to other climate components on the SH. Therefore, recent climate trends in the SH can obviously be related to the positive trend of the AAO.

Furthermore, the same EOF analysis was carried out for z'_{50} geopotential height anomalies in order to characterise the dominant stratospheric patterns of variability, which in austral summer and austral spring appear as zonally symmetric variability pattern around the pole. However, austral winter and austral autumn reveal more asymmetric and distorted variability patterns that might be attributed to enhanced vertical propagation of planetary waves in these seasons. As in the troposphere, positive linear trends of the stratospheric leading PC time series could be detected in austral summer and austral autumn.

In order to study temporal interannual variability of the tropospheric AAO in more detail, wavelet transforms of the respective stratospheric and tropospheric leading PC time series were computed (see Chapter 3.5). However, barely any spectral signals differ significantly from the corresponding theoretical red-noise spectrum of an AR(1) process.

As already motivated above, the Antarctic Oscillation and its temporal development can be employed as a helpful indicator for the prediction of future changes in SH's climate. In order to assess the reliability of future projections by climate models, the capability of different climate model setups in simulating recent AAO patterns and trends was studied on seasonal levels. In this respect, data from different model configurations, all containing the atmospheric general circulation model ECHAM (MPI-ESM-MR, ECHAM6.1/6.3, ECHAM6.3+SWIFT, see Chapters 4.2–4.5), have been analysed to assess their skills in reproducing trends and patterns of the AAO. Especially the use of the interactive ozone module polar SWIFT was motivated by different previous studies, which emphasised the importance of climate-ozone feedbacks [Thompson et al., 2002; Fogt et al., 2009; Romanowsky et al., 2019]. Nevertheless, the tropospheric (z'_{700}) analysis of the different model data revealed that in general the model setups were not able to reproduce recent tropospheric AAO trends and especially not the asymmetric AAO structure in mid-latitudes (see Chapter 4.5.3 and 4.5.2). This was however hard to assess, due to the relatively large spread between different ensemble members and would require more ensemble simulation for meaningful statistics. In contrast to the troposphere, stratospheric (z'_{50}) trends of the variability patterns were generally reproduced by most model runs (see Chapter 4.5.3). This shows on the one hand, that the models are generally capable to simulate the time-delayed impacts of recent springtime ozone losses on the stratospheric summer circulation very well; on the other hand, the inability to reproduce the tropospheric trends indicates problems in simulating troposphere-stratosphere interactions realistically—particularly the time-delayed downward propagation of stratospheric signals induced by ozone depletion in springtime. Overall, the model setups had less difficulties in reproducing the simpler symmetric variability pattern in austral summer and austral spring, compared to the distorted stratospheric variability pattern in austral winter and austral autumn (see Chapter 4.5.2), as well as to the more complex tropospheric patterns.

As expected, the coupled MPI-ESM simulations did not yield any significant improvements, since the tropospheric AAO is assumed to be a result of internal atmospheric dynamics. Apart from the fact, that interactive ozone chemistry might not play the key role when trying to simulate the AAO realistically, there might be other reasons why polar SWIFT did not show any improvements:

- The fact that SWIFT only considers vortex-averaged mixing ratios might be an oversimplification in the SH, as the Antarctic polar vortex may be splitted into a well-mixed inner vortex core and a broad ring of weakly-mixed air near the vortex edge [Lee et al., 2001].
- In contrast to the NH [Romanowsky et al., 2019], the stratospheric polar vortex in the SH is more zonally symmetric around the pole; therefore, the use of zonally averaged ozone climatologies in the SH (as done by most CMIP5 models) might even outperform polar SWIFT, which uses a single vortex-averaged ozone value.

Whether this insufficiency—especially in the troposphere and on seasonal time scales—in simulating recent trends of the AAO is solely a shortcoming of ECHAM or of other state-of-the-art atmospheric general circulation model as well, should be addressed in future studies. Although other ensemble studies [Zheng et al., 2013] suggested improvements of CMIP3 over CMIP5 model experiments, it remains to be seen whether upcoming CMIP6 model simulations perform better in simulating the Antarctic Oscillation.

A general deficiency of climate models in simulating recent temporal trends of dominant atmospheric variability patterns would raise the question, to what extent they are able to project future climate change correctly. Due to the high complexity of atmospheric variability patterns, improvements in simulating their temporal and spatial characteristics might be a slow, but steady process over the upcoming years. This process may potentially come along with future optimizations of climate models in their entirety, such as the development of better physical parametrisations, finer model resolution of small-scale processes or a general better representations of troposphere-stratosphere processes.

APPENDIX A

A.1 WAVELET TRANSFORMS OF STRATOSPHERIC PC TIME SERIES

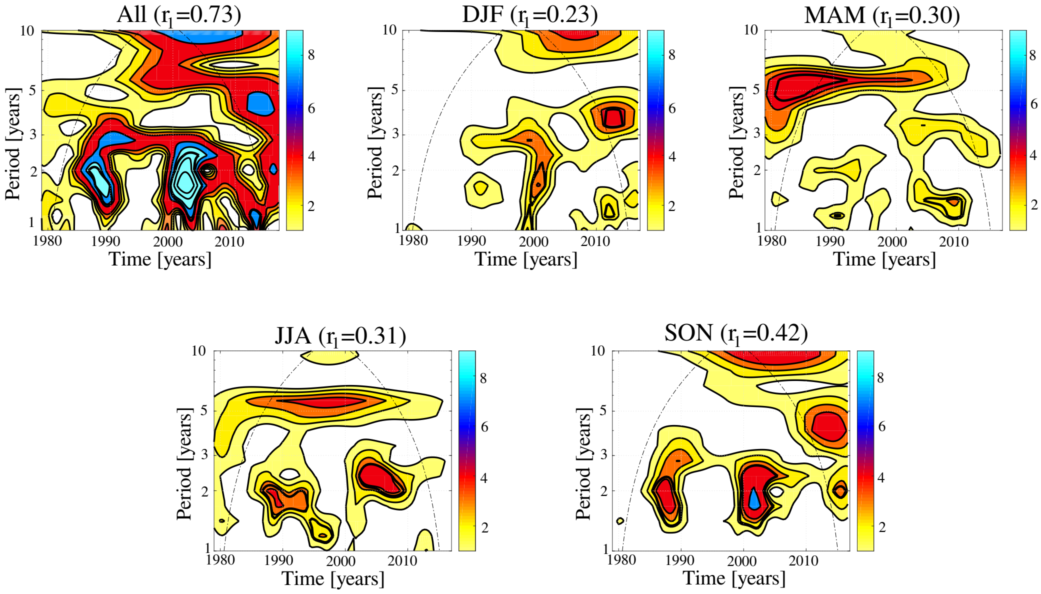

Figure A.1: Same wavelet transform as in Figure 3.6 but for the detrended z'_{50} leading PC time series.

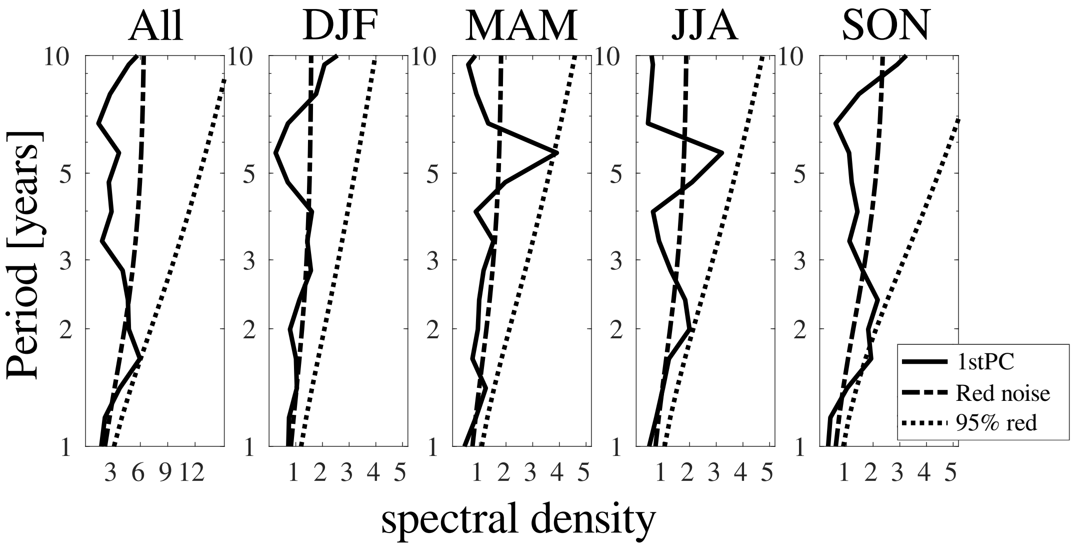

Figure A.2: Same global wavelet sepctrum as in Figure 3.7 but for the detrended z'_{50} leading PC time series.

A.2 TROPOSPHERIC AAO PATTERNS AND TIME SERIES

The leading tropospheric (z'_{700}) EOFs and the respective standardised PC are shown for all model setups, as well as for the ERA-Interim reanalysis. The EOFs and PC time series have been calculated according to the same procedure described in Chapter 3.3.

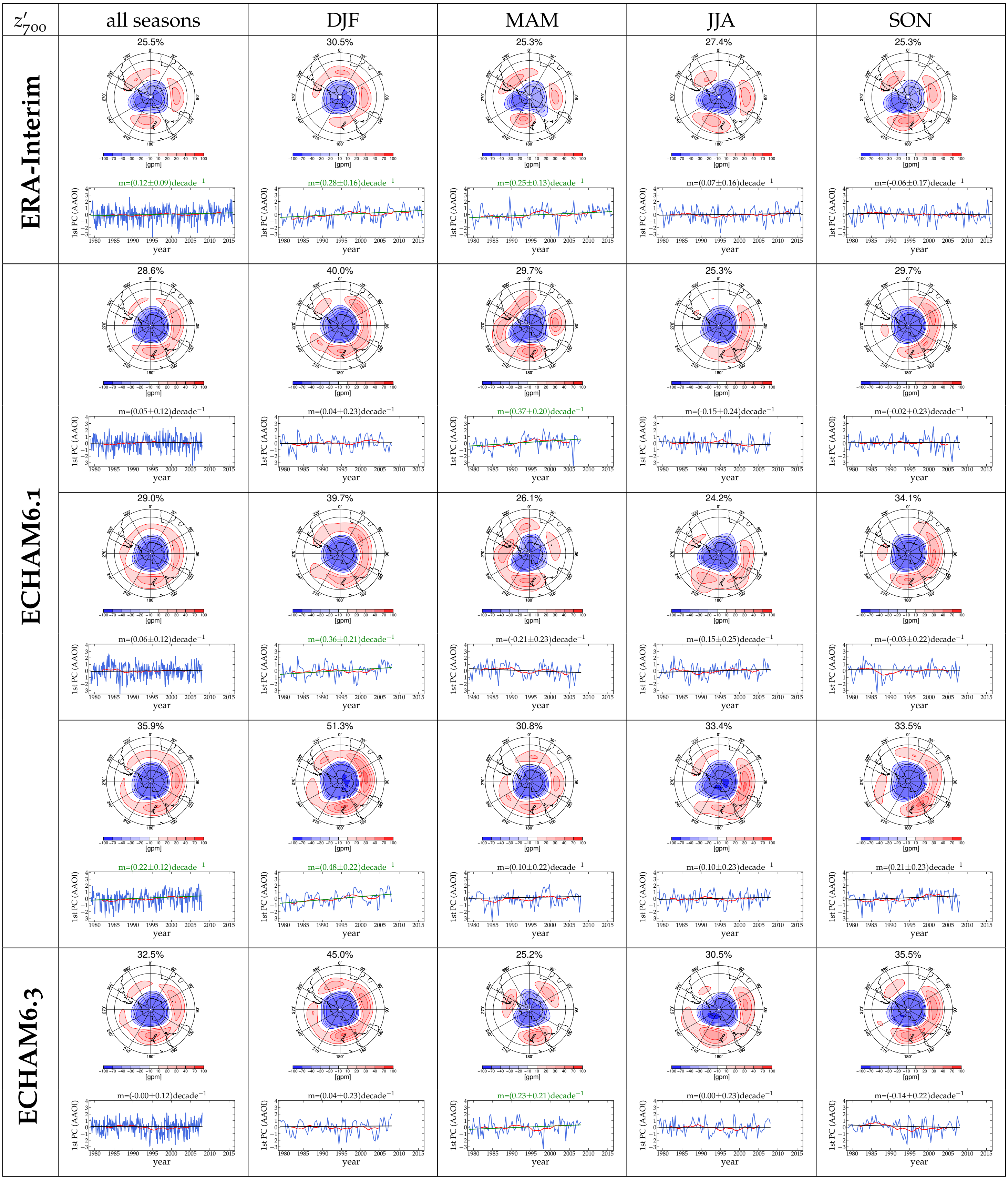

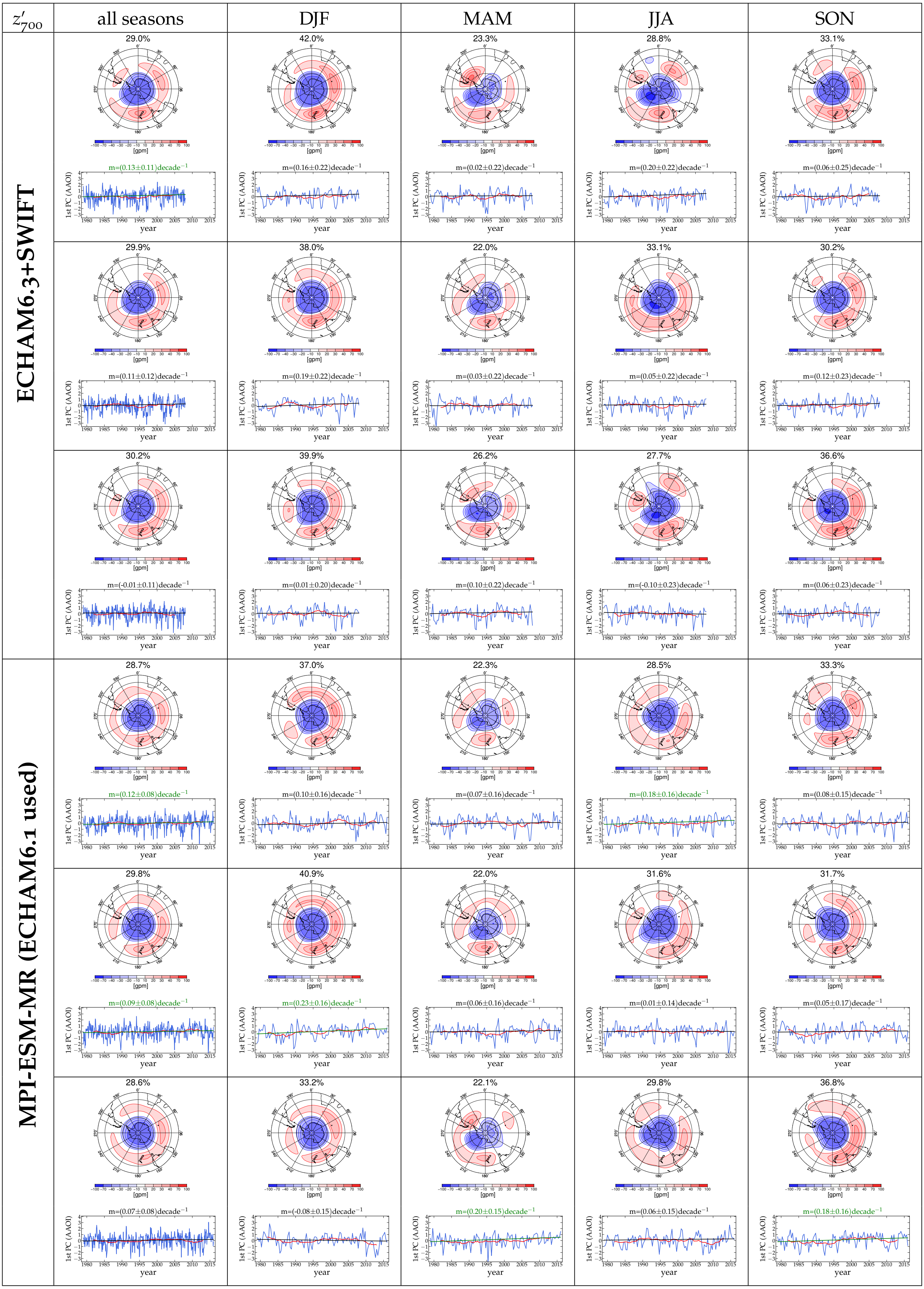z'_{700}
all seasons
DJF
MAM
JJA
SON
ECHAM6.3+SWIFT
MPI-ESM-MR (ECHAM6.1 used)
29.0%
m=(0.13±0.11)decade^{-1}
42.0%
m=(0.16±0.22)decade^{-1}
23.3%
m=(0.02±0.22)decade^{-1}
28.8%
m=(0.20±0.22)decade^{-1}
33.1%
m=(0.06±0.25)decade^{-1}
29.9%
m=(0.11±0.12)decade^{-1}
38.0%
m=(0.19±0.22)decade^{-1}
22.0%
m=(0.03±0.22)decade^{-1}
33.1%
m=(0.05±0.22)decade^{-1}
30.2%
m=(0.12±0.23)decade^{-1}
30.2%
m=(-0.01±0.11)decade^{-1}
39.9%
m=(0.01±0.20)decade^{-1}
26.2%
m=(0.10±0.22)decade^{-1}
27.7%
m=(-0.10±0.23)decade^{-1}
36.6%
m=(0.06±0.23)decade^{-1}
28.7%
m=(0.12±0.08)decade^{-1}
37.0%
m=(0.10±0.16)decade^{-1}
22.3%
m=(0.07±0.16)decade^{-1}
28.5%
m=(0.18±0.16)decade^{-1}
33.3%
m=(0.08±0.15)decade^{-1}
29.8%
m=(0.09±0.08)decade^{-1}
40.9%
m=(0.23±0.16)decade^{-1}
22.0%
m=(0.06±0.16)decade^{-1}
31.6%
m=(0.01±0.14)decade^{-1}
31.7%
m=(0.05±0.17)decade^{-1}
28.6%
m=(0.07±0.08)decade^{-1}
33.2%
m=(-0.08±0.15)decade^{-1}
22.1%
m=(0.20±0.15)decade^{-1}
29.8%
m=(0.06±0.15)decade^{-1}
36.8%
m=(0.18±0.16)decade^{-1}
-100 -70 -40 -30 -20 -10 10 20 30 40 70 100
[gpm]
0°
30°
60°
90°
120°
150°
180°
210°
240°
270°
300°
330°
1st PC (AAOI)
4
3
2
1
0
-1
-2
-3
1980
1985
1990
1995
2000
2005
2010
2015
year

A.3 STRATOSPHERIC AAO PATTERNS AND TIME SERIES

The leading stratospheric (z'_{50}) EOFs and the respective standardised PC are shown for all model setups, as well as for the ERA-Interim reanalysis. The EOFs and PC time series have been calculated according to the same procedure described in Chapter 3.3.

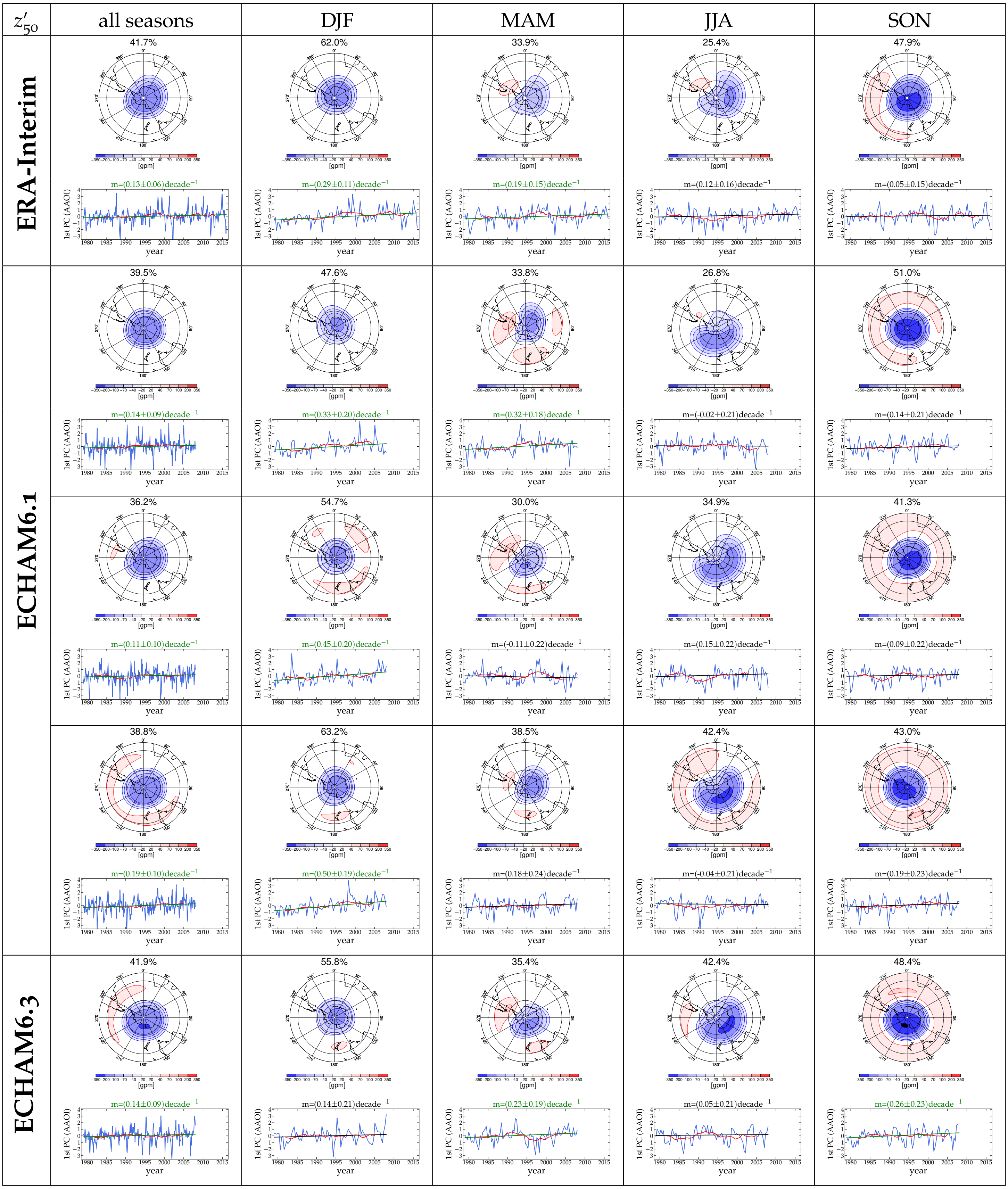

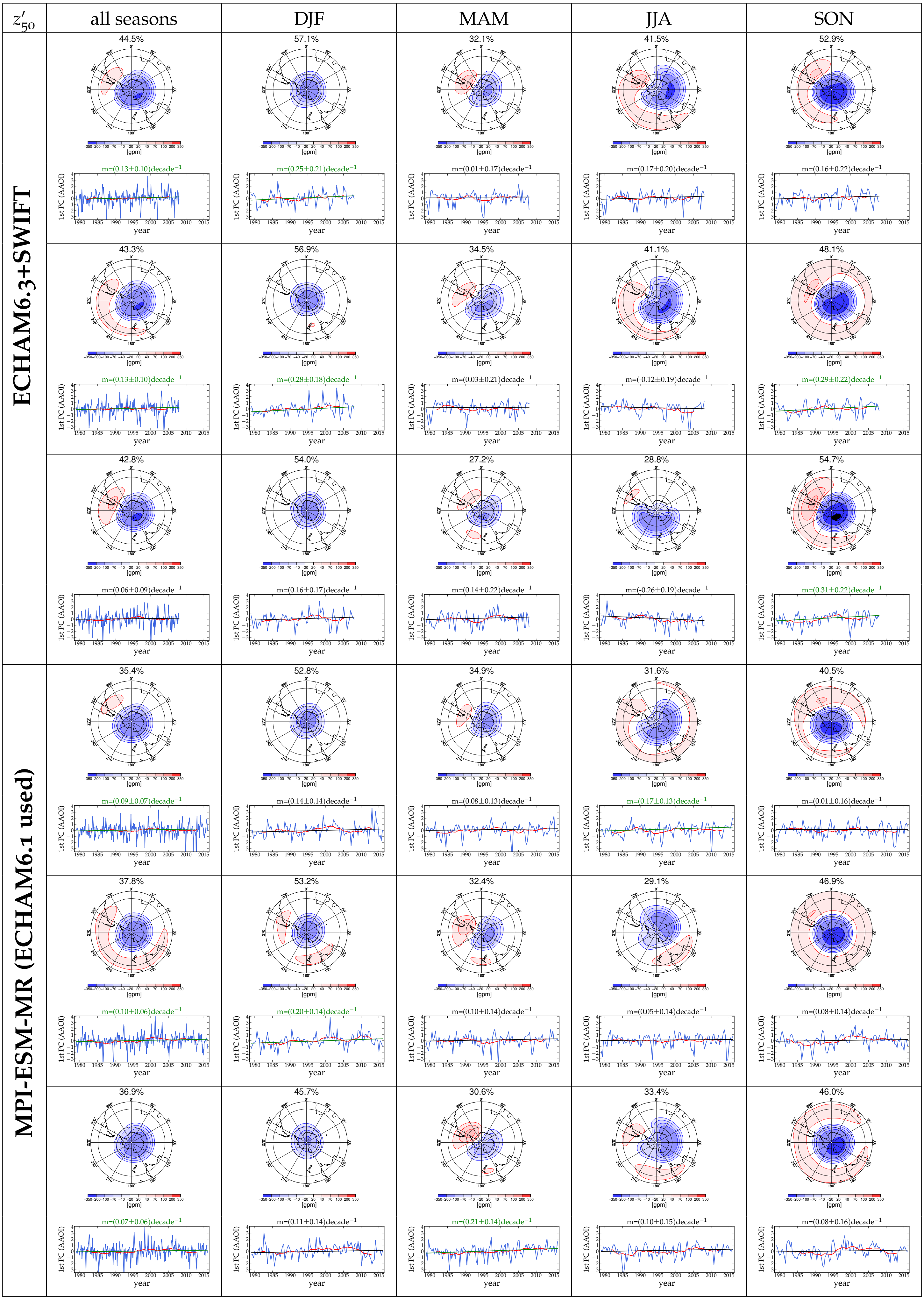
z'_{50}
all seasons
DJF
MAM
JJA
SON
ECHAM6.3+SWIFT
MPI-ESM-MR (ECHAM6.1 used)
44.5%
57.1%
32.1%
41.5%
52.9%
m=(0.13±0.10)decade^{-1}
m=(0.25±0.21)decade^{-1}
m=(0.01±0.17)decade^{-1}
m=(0.17±0.20)decade^{-1}
m=(0.16±0.22)decade^{-1}
43.3%
56.9%
34.5%
41.1%
48.1%
m=(0.13±0.10)decade^{-1}
m=(0.28±0.18)decade^{-1}
m=(0.03±0.21)decade^{-1}
m=(-0.12±0.19)decade^{-1}
m=(0.29±0.22)decade^{-1}
42.8%
54.0%
27.2%
28.8%
54.7%
m=(0.06±0.09)decade^{-1}
m=(0.16±0.17)decade^{-1}
m=(0.14±0.22)decade^{-1}
m=(-0.26±0.19)decade^{-1}
m=(0.31±0.22)decade^{-1}
35.4%
52.8%
34.9%
31.6%
40.5%
m=(0.09±0.07)decade^{-1}
m=(0.14±0.14)decade^{-1}
m=(0.08±0.13)decade^{-1}
m=(0.17±0.13)decade^{-1}
m=(0.01±0.16)decade^{-1}
37.8%
53.2%
32.4%
29.1%
46.9%
m=(0.10±0.06)decade^{-1}
m=(0.20±0.14)decade^{-1}
m=(0.10±0.14)decade^{-1}
m=(0.05±0.14)decade^{-1}
m=(0.08±0.14)decade^{-1}
36.9%
45.7%
30.6%
33.4%
46.0%
m=(0.07±0.06)decade^{-1}
m=(0.11±0.14)decade^{-1}
m=(0.21±0.14)decade^{-1}
m=(0.10±0.15)decade^{-1}
m=(0.08±0.16)decade^{-1}
0° 30° 60° 90° 120° 150° 180° 210° 240° 270° 300° 330°
−350 −200 −100 −70 −40 −20 20 40 70 100 200 350
[gpm]
1st PC (AAOI)
year
1980 1985 1990 1995 2000 2005 2010 2015

METHODS B

B.1 EMPIRICAL ORTHOGONAL FUNCTION ANALYSIS

Empirical Orthogonal Function (EOF) Analysis is a common and widely used statistical technique in atmospheric science for analysing data in high dimensional phase spaces and also for dimensionality reduction. The objective is to structure, to simplify and especially to find in place of the ordinary original variables $x_i(t)$ a relatively small number of new independent variables $u_i(t)$, which represent as much of the original data sets variability as possible. For this reason, a new set of orthogonal coordinate axes $\mathbf{e_i^u}$ instead of the ordinary and often more intuitive axes $\mathbf{e_i^x}$ has to be found, in which to examine the data.
The desirable characteristics of the new orthogonal coordinate axes are given in a way that:

- the maximum possible amount of variance or variation within the data set can be explained along the axis $\mathbf{e_1^u}$ (with new coordinates $u_1(t)$)
- the maximum possible amount of remaining residual variance of the data set can be explained along the subsequent axis $\mathbf{e_2^u}$
- and so forth for the remaining axis $\mathbf{e_i^u}$,

subjected to the condition that the new variables $u_i(t)$ are uncorrelated with the variables having lower indices.

In contrast to other analysis and transformation techniques, such as Fourier Transforms or Taylor expansions, in which fixed sinusoidal or polynomial coordinate systems are used, the coordinate axes $\mathbf{e_i^u}$ for an EOF analysis have to be identified uniquely for each specific data set. Due to its wide field of potential applications, EOF analysis is for instance also referred to as a discrete form of the *Karhunen-Loève* Transform in signal processing and theory of stochastic processes, or to eigenvalue decomposition in linear algebra.

B.1.1 *Basic principle in two dimensions*

The general procedure of EOF analysis can be best visualized and illustrated in the two-dimensional case. For this reason, we will consider a two-dimensional phase space with two variables x_1 and x_2 measured simultaneously at certain times, which for instance may be associated with two temperature measurements at two different locations. In Figure B.1, the two variables x_1 and x_2 reveal a strong positive correlation. Instead of using the original coordinate system $\mathbf{e_1^x}$ and $\mathbf{e_2^x}$, which are associated with the two variables x_1 and x_2, this system could be rotated in order to obtain a new system with variables u_1 and u_2 and with new orthogonal coordinate axes $\mathbf{e_1^u}$ and $\mathbf{e_2^u}$. As depicted in Figure B.1 (right), displaying the data set in the new u-coordinates shows that most variance or spread of the data set is represented along axis $\mathbf{e_1^u}$. The small amount of residual variance is explained along the orthogonal axis $\mathbf{e_2^u}$.
Thus it is obvious, that the initial 2-dimensional structure of the data set can be reduced to a

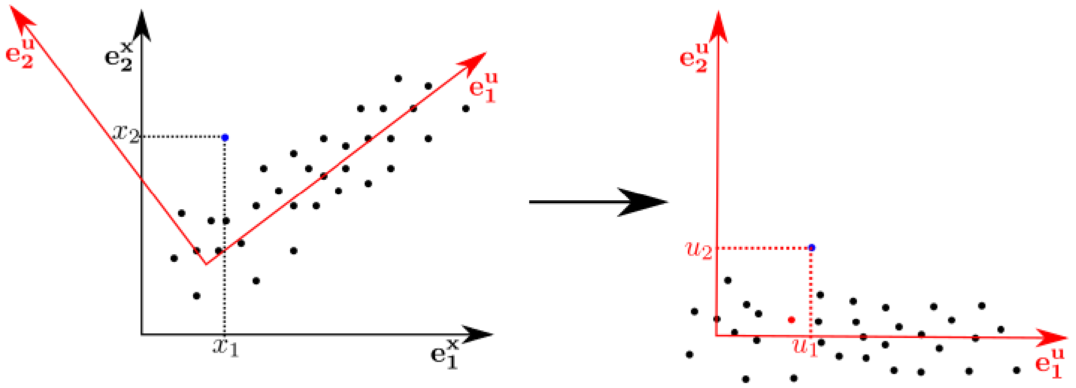

Figure B.1: Illustration of the basic principle of an EOF analysis: A data set initially represented in an intuitive x-coordinate system may be examined in a new coordinate system with axes $\mathbf{e_1^u}$ and $\mathbf{e_2^u}$ and variables u_1 and u_2. Most variance is represented along $\mathbf{e_1^u}$ and th small amount of residual variance along $\mathbf{e_2^u}$.

1-dimensional perspective by only considering the new variable u_1; however, at the expanse of loosing a certain amount of information about the data set.

B.1.2 *Extension and generalisation to higher dimensions*

EOF analysis reveals its greatest power, when it comes to analysing high dimensional data sets, which are rather hard to visualize and to structure due to the large number of given variables x_i [Wilks, 2006; Kidson et al., 1975]. For this reason, the previous considerations might be extended and quantified to higher N-dimensional phase spaces, which is the general case for a time series of climatic variables x (e.g. sea surface temperature, pressure) defined on N grid points around the globe and measured at T different times t_k. The climatic variable x at a specific grid point $i = 1, ..., N$ at time t_k $(k = 1, 2, ..., T)$ is denoted by $x_i(t_k)$ and shall be represented in the new coordinate system $\mathbf{e_i^u}$. This may be summarized at time t_k in vector notation as

$$\mathbf{x}(t_k) = (x_0(t_k), x_1(t_k), ..., x_N(t_k)) = \sum_{i=1}^{N} \mathbf{e_i^u} u_i(t_k).$$

The native and most intuitive N basis vectors are given by $\mathbf{e_1^x} = (1, 0, 0, ..., 0)$, $\mathbf{e_2^x} = (0, 1, 0, ..., 0)$ with respective coordinates $x_1(t_k)$, $x_2(t_k)$ and so forth.

For identifying the axis $\mathbf{e_1^u}$, along which the corresponding projected variance

$$\sigma_1^2 = \frac{\mathbf{e_1^u} \underline{\mathbf{S}}^{\mathbf{x}} \mathbf{e_1^u}^T}{\mathbf{e_1^u} \mathbf{e_1^u}^T} \tag{B.1}$$

is maximised (see Chapter B.1), the covariance matrix $\underline{\mathbf{S}}^{\mathbf{x}}$ of the N-dimensional time series $\mathbf{x}(t_k)$ has to be calculated, which components are defined as

$$S_{ij}^x = \mathrm{E}[(x_i(t_k) - \mu_i)(x_j(t_k) - \mu_j)]. \tag{B.2}$$

μ_i denotes the expectation value in time at grid point i, E[...] is the temporal expectation value and the x-index signifies that the matrix is given in initial x coordinates.

It points out that the variance σ_1, which is defined by the so called Rayleigh quotient in Equation B.1, is maximised by the eigenvector of the covariance matrix $\underline{\mathbf{S}}^{\mathbf{x}}$ corresponding to its largest eigenvalue.Therefore, the axis $\mathbf{e}_1^{\mathbf{u}}$ is given by the eigenvector of the covariance matrix $\underline{\mathbf{S}}^{\mathbf{x}}$ corresponding to its largest eigenvalue and the subsequent desired new coordinate axes $\mathbf{e}_\mathbf{i}^{\mathbf{u}}$ are given by the subsequent eigenvectors of $\underline{\mathbf{S}}^{\mathbf{x}}$.

The corresponding new time dependent variables $u_i(t_k)$ are related to the new basis vectors $\mathbf{e}_\mathbf{i}^{\mathbf{u}}$ and the original variables $x_i(t_k)$ by the projection relation

$$u_i(t_k) = \mathbf{e}_\mathbf{i}^{\mathbf{u}}\mathbf{x}(t_k) = \sum_{j=1}^{N} e_{ij}^{u} x_j(t_k). \tag{B.3}$$

As the covariance matrix $\underline{\mathbf{S}}^{\mathbf{x}}$ is symmetric, its eigenvectors and consequently the new coordinate axes $\mathbf{e}_\mathbf{i}^{\mathbf{u}}$ are orthogonal as required and its eigenvalues λ_i are real.

Transforming a symmetric covariance matrix into a representation in its Eigenbasis always implies that the resulting matrix is diagonal. For this reason, represented in the new rotated coordinate system $\mathbf{e}_\mathbf{i}^{\mathbf{u}}$ (or Eigenbasis), the covariance matrix $\underline{\mathbf{S}}^{\mathbf{u}}$ has the form

$$\underline{\mathbf{S}}^{\mathbf{u}} = \begin{pmatrix} \lambda_1 & 0 & \dots & 0 \\ 0 & \lambda_2 & \dots & 0 \\ \vdots & \vdots & \ddots & \vdots \\ 0 & 0 & \dots & \lambda_N \end{pmatrix}.$$

As the off-diagonal entries are zero, the new variables u_i are uncorrelated with each other.

Furthermore, the respective real-valued eigenvalues λ_i characterise the fraction of explained variance R_i^2 along an axis $\mathbf{e}_\mathbf{i}^{\mathbf{u}}$, which is given by the ratio of the respective eigenvalue λ_i to the total variance

$$R_i^2 = \frac{\lambda_i}{\sum\limits_{j=1}^{N} \lambda_j}. \tag{B.4}$$

The new variables $u_i(t_k)$ are commonly called i-th *Principal Components* (PC) and the respective coordinate axes $\mathbf{e}_\mathbf{i}^{\mathbf{u}}$ are called i-th *Empirical Orthogonal Functions* (EOF).

Since vectors of different magnitude, which are aligned into the same direction might act as eigenvectors of the correlation matrix $\underline{\mathbf{S}}^{\mathbf{x}}$, there exist different scaling conventions for the EOFs and the corresponding PCs. For analyses in this thesis, the EOFs will be defined in a way that the respective PC time series have unit variance.

As EOFs are generally computed from a finite set of data, the calculated EOFs are generally subjected to sampling errors and their true population counterpars are not known. In this respect, North et al., 1982 established the rule of thumb that when a group of true population eigenvalues lie within the sampling errors $\delta\lambda_i \sim \lambda_i\sqrt{\frac{2}{N}}$ of each other, then the sampled EOFs $\mathbf{e}_\mathbf{i}^{\mathbf{u}}$ associated with λ_i are random mixtures of the true population EOFs.

It is important to bear in mind that due to the linear character of standard EOF analysis, this method is mostly suitable for detecting linear structures in the data, whereas for identifying potential nonlinear structures within the data set a huge variety of techniques. Such nonlinear methods include for instance *nonlinear Principal Components Analysis* [Monahan, 2000] or *Self Organising Maps*, which are however often hard to interpret [Mori et al., 2016].

B.2 TREND AND SIGNIFICANCES

For estimating the slope of a linear trend of a time series $x(t_k)$ observed at N time steps t_k, the non-parametric, unbiased and robust Theil-Sen estimator

$$m = \mathrm{median}\left(\frac{x_\mathrm{k} - x_\mathrm{j}}{t_\mathrm{k} - t_\mathrm{j}}\right) \quad \text{for all pairs of } k, j = 1, ...N \quad \text{with} \quad k > j \tag{B.5}$$

is used, which estimates the slope as the median of all slopes between paired values.

Since many time series analysed in this thesis do not fulfill certain assumption making the ordinary least-squares estimator an efficient estimator of the true population slope, the Theil-Sen estimator is preferred, since it is less sensitive to outliers, to a skewed or non-Gaussian distribution of residuals, as well as to violations of the homoscedasticity assumption.

For assessing whether the fitted trends are reliable and not a random result of variability, confidence intervals were constructed by employing a bootstrap resampling approach. Initially, the best-fit line with Sen's slope estimator $\bar{m}$ was computed and the N residuals were kept. Afterwards, N values from the residuals were randomly selected with replacement and added to the original best-fit line of the original data. Then, the trend m was re-estimated for the newly created time series of length N. This procedure was repeated 5000 times and the standard deviation σ_m of trend slopes m was calculated .

A trend is now termed "significant" (meaning significantly different from a zero trend) if a zero trend does not fall within the computed 95 % confidence interval ($\bar{m} \pm 1.96\sigma_\mathrm{m}$), assuming that the underlying bootstrapped probability distribution $p(m)$ is Gaussian. This definition of significance is equivalent to a Z-test, which rejects the null hypothesis (trends are distributed according to the bootstrapped probability distribution $p(m)$) on a 5 % significance level.

B.3 WAVELET TRANSFORM

Ordinary frequency analysis of time series usually employs Fourier Transforms. On the one hand, this technique results in a perfect frequency resolution but on the other hand, provides no temporal resolution—that is, the information at which specific times step or time interval a certain frequency is detected in the time series. This drawback of standard Fourier Transform is a consequence of the fact that the signal is decomposed into sine and cosine waves. Such waves can perfectly be scaled in the frequency domain but have however an infinite extent and allow for no localisation in the time domain. A straightforward remedy for this insufficiency is the Short-Time Fourier Transform (STFT), which simply divides the original time series into shorter segments of equal length and computes the Fourier Transform separately for each segment. The uncertainty principle $\Delta t \Delta \omega \geq \frac{1}{2}$ constrains the simultaneous resolution of time Δt

and frequency $\Delta\omega$. Generally, within the low frequency range higher resolutions in frequency are commonly desired at the expanse of coarser time resolution—and vice versa for higher frequencies.

Since STFT uses segments of equal length, the implied temporal resolution for low and high frequencies remains constant. Therefore, a popular and more elegant extension to this method is the so-called wavelet transform, which has a wide range of potential applications, for instance in image compression, signal processing or atmospheric science [Torrence et al., 1998]. The wavelet transform $[W_\Psi x(t)](a,b)$ of a time series $x(t)$ is given by

$$[W_\Psi x(t)](a,b) = \frac{1}{\sqrt{|a|}} \int_{-\infty}^{\infty} \overline{\Psi\left(\frac{t-b}{a}\right)} x(t) \mathrm{d}t, \tag{B.6}$$

where the overbar denotes the complex conjugate. Instead of sine and cosine basis function, that transform employs wavelets $\Psi\left(\frac{t-b}{a}\right)$, which can be considered as wave packets that can be shifted in the time domain by varying parameter b. Altering scaling parameter a may lead to compression of the wavelet, which implies the desired property of better localisation in time for higher frequencies. Contrary, wavelet-stretching results in lower frequencies and a coarser resolution in time. In order to guarantee that the corresponding frequency-time domain can be reconstructed form shifting and scaling parameters of the computed wavelet transform $[W_\Psi x(t)](a,b)$, the wavelet $\Psi(t)$ requires being a quadratically integrable function with finite energy

$$\int_{-\infty}^{\infty} |\Psi(t)|^2 \mathrm{d}t < \infty. \tag{B.7}$$

Additionally, it has to fulfill the admissibility condition

$$2\pi \int_{-\infty}^{\infty} \frac{|\hat{\Psi}(\omega)|^2}{\omega} \mathrm{d}\omega < \infty, \tag{B.8}$$

which ensures zero mean $\int_{-\infty}^{\infty} \Psi(t)\mathrm{d}t{=}0$ and vanishing zero frequency component $\hat{\Psi}(\omega{=}0){=}0$ in the wavelet's Fourier transform $\hat{\Psi}$. Under these conditions, shifting and scaling parameters (a and b) of the computed wavelet transform $[W_\Psi x(t)](a,b)$ can be used to reconstruct the corresponding frequency-time domain. A popular wavelet $\Psi\left(\frac{t-b}{a}\right)$ frequently chosen for such an analysis is the *Morlet* wavelet, which is basically a sine wave windowed by a Gaussian envelope.

A common approach for assessing and comparing time series and their spectra is to consider an Autoregressive AR(1) model

$$x_{\mathrm{t+1}} = r_1(x_{\mathrm{t}} - \mu) + \mu + \varepsilon_{\mathrm{t+1}}, \tag{B.9}$$

which takes into account the lag-1 autocorrelation r_1 and the mean μ. The white noise ε_{t+1} with amplitude $\sigma_\varepsilon^2 = (1 - r^2)\sigma_x$ is connected to the variance σ_x of the simulated time series $x(t)$. The theoretical spectral density of such a process of length n is given by

$$S_{\text{theo}}(\omega) = \frac{\sigma_\varepsilon^2}{1 + r_1^2 - 2r_1 \cos(\omega)} \tag{B.10}$$

and for persistence parameter $0 \leq r_1 \leq 1$ a "red"-spectrum is exhibited with higher frequencies smoothed out and lower frequencies retained.

For assessing whether the spectral density $\hat{S}(\omega)$ of some time series at a distinct frequency ω is significantly larger than the theoretical spectral density S_{theo} of an AR(1) process with same r_1, μ and σ_x, the upper confidence limit is given by [Wilks, 2006]

$$\hat{S}(\omega) \geq \frac{S_{\text{theo}}(\omega)}{\nu} \chi_\nu^2 (1 - \alpha), \tag{B.11}$$

where α is the quantile of the Chi-squared distribution $\chi_\nu^2(1 - \alpha)$ with ν degrees of freedom.

B.4 TAYLOR DIAGRAM

Taylor diagrams [Taylor, 2001] are useful tools in order to graphically compare a spatial (model) pattern f_n with a reference (reanalysis) pattern r_n, both defined on N grid points with n=1, ..., N. In this respect, the relative skill of the models in reproducing the reference pattern is characterised by different statistics:

- The amplitude of the model pattern given by the standard deviation

  $$\sigma_f = \sqrt{\frac{1}{N-1} \sum_{n=1}^{N} \left(f_n - \bar{f}\right)^2}, \tag{B.12}$$

  where $\bar{f}$ denotes the mean. The standard deviation σ_r of the reanalysis pattern is defined similarly.

- The centred Root-Mean-Square (RMS) difference between model and reanalysis pattern

  $$E' = \sqrt{\frac{1}{N} \sum_{n=1}^{N} [(f_n - \bar{f}) - (r_n - \bar{r})]^2}. \tag{B.13}$$

- And the pattern correlation coefficient between both patterns

  $$R = \frac{\frac{1}{N} \sum_{n=1}^{N} (f_n - \bar{f}) \cdot (r_n - \bar{r})}{\sigma_f \sigma_r} \tag{B.14}$$

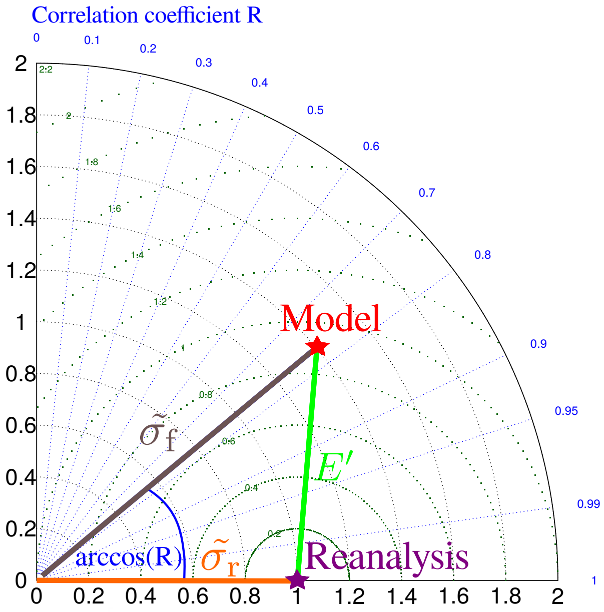

Figure B.2: Example and illustration of a Talyor diagram, which simultaneously represents different statistics by a single dot ($\tilde{\sigma}_{\mathrm{f}}$, R and E') for graphically comparing the resemblance of different model patterns with a reference reanalysis pattern.

The relationship between these four different statistics may be written as

$$E'^2 = \sigma_{\mathrm{f}}^2 + \sigma_{\mathrm{r}}^2 - 2\sigma_{\mathrm{f}}\sigma_{\mathrm{r}}\cos(R), \tag{B.15}$$

allowing in combination with the law of cosine for a convenient simultaneous representation of all four statistics in a 2-D Taylor diagram by a single dot (see Figure B.2).

When f_{n} and r_{n} are normalised such that the reference standard deviation is set to unity $\sigma_{\mathrm{r}} = 1$, then within the Taylor diagram the radial distance between model point and origin indicates the relative standard deviation $\tilde{\sigma}_{\mathrm{f}} = \frac{\sigma_{\mathrm{f}}}{\sigma_{\mathrm{r}}}$ of the model compared to the reference data. Thus, the drawn quadrants around the origin indicate levels of constant $\tilde{\sigma}_{\mathrm{f}}$.
The cosine of the angle enclosed by the horizontal axis and the radial line to the model point is equivalent to the pattern correlation coefficient R between model and reanalysis pattern.

Additionally, the centred RMS difference E' is directly given by the distance between model point and reference reanalysis point. Therefore, the green dotted semicircles originating at the reference point indicate levels of constant E'.

BIBLIOGRAPHY

Ångström, A. (1935). “Teleconnections of Climatic Changes in Present Time.” In: *Geografiska Annaler* 17.3-4, pp. 242–258.

Bates, D. R. and M. Nicolet (1950). “The photochemistry of atmospheric water vapor.” In: *Journal of Geophysical Research* 55.3, pp. 301–327.

Bauer, E. and D. Handorf (2004). “Holocene Climate Variability from Model Simulations—State of the Art.” In: *The climate in Historical Times*. Springer Berlin Heidelberg, pp. 57–75.

Bintanja, R. et al. (2013). “Important role for ocean warming and increased ice-shelf melt in Antarctic sea-ice expansion.” In: *Nature Geoscience* 6.5, pp. 376–379.

Bracco, A. et al. (2004). “Internal variability, external forcing and climate trends in multi-decadal AGCM ensembles.” In: *Climate Dynamics* 23.6, pp. 659–678.

Brewer, A. W. (1949). “Evidence for a world circulation provided by the measurements of helium and water vapour distribution in the stratosphere.” In: *Quarterly Journal of the Royal Meteorological Society* 75.326, pp. 351–363.

Bromwich, D. H. et al. (2007). “A tropospheric assessment of the ERA-40, NCEP, and JRA-25 global reanalyses in the polar regions.” In: *Journal of Geophysical Research: Atmospheres* 112.D10.

Butler, A. H., D. W. J. Thompson, and K. R. Gurney (2007). “Observed relationships between the Southern Annular Mode and atmospheric carbon dioxide.” In: *Global Biogeochemical Cycles* 21.4.

Cai, W. et al. (2015). “ENSO and greenhouse warming.” In: *Nature Climate Change* 5.9, pp. 849–859.

Cash, B. A., P. J. Kushner, and G. K. Vallis (2002). “The Structure and Composition of the Annular Modes in an Aquaplanet General Circulation Model.” In: *Journal of the Atmospheric Sciences* 59.23, pp. 3399–3414.

Chapman, S (1930). *A theory of upper-atmospheric ozone*. London: Edward Stanford.

Charlton, A. J. et al. (2005). “The impact of the stratosphere on the troposphere during the southern hemisphere stratospheric sudden warming, September 2002.” In: *Quarterly Journal of the Royal Meteorological Society* 131.609, pp. 2171–2190.

Charney, J. G. and P. G. Drazin (1961). “Propagation of planetary-scale disturbances from the lower into the upper atmosphere.” In: *Journal of Geophysical Research* 66.1, pp. 83–109.

Chen, B. and Z. Liu (2016). “Global water vapor variability and trend from the latest 36 year (1979 to 2014) data of ECMWF and NCEP reanalyses, radiosonde, GPS, and microwave satellite.” In: *Journal of Geophysical Research: Atmospheres* 121.19.

Cionni, I. et al. (2011). “Ozone database in support of CMIP5 simulations: results and corresponding radiative forcing.” In: *Atmospheric Chemistry and Physics* 11.21, pp. 11267–11292.

Claussen, M. et al. (2002). “Earth system models of intermediate complexity: closing the gap in the spectrum of climate system models.” In: *Climate Dynamics* 18.7, pp. 579–586.

Connolley, W. M. (1997). “Variability in annual mean circulation in southern high latitudes.” In: *Climate Dynamics* 13.10, pp. 745–756.

Coumou, D. et al. (2014). "Quasi-resonant circulation regimes and hemispheric synchronization of extreme weather in boreal summer." In: *Proceedings of the National Academy of Sciences* 111.34, pp. 12331–12336.

Crutzen, P. J. (1970). "The influence of nitrogen oxides on the atmospheric ozone content." In: *Quarterly Journal of the Royal Meteorological Society* 96.408, pp. 320–325.

Dee, D. P. et al. (2011). "The ERA-Interim reanalysis : configuration and performance of the data assimilation system." In: *Quarterly Journal of the royal meteorological society* 137.656, pp. 553–597.

Diaz, H. F., M. P. Hoerling, and J. K. Eischeid (2001). "ENSO variability, teleconnections and climate change." In: *International Journal of Climatology* 21.15, pp. 1845–1862.

Ding, Q. et al. (2012). "Influence of the Tropics on the Southern Annular Mode." In: *Journal of Climate* 25.18, pp. 6330–6348.

Fan, K. and H. Wang (2004). "Antarctic oscillation and the dust weather frequency in North China." In: *Geophysical Research Letters* 31.10.

Farman, J. C., B. G. Gardiner, and J. D. Shanklin (1985). "Large losses of total ozone in Antarctica reveal seasonal ClOx/NOx interaction." In: *Nature* 315.6016, pp. 207–210.

Feldstein, S. B. and C. L. E. Franzke (2017). "Atmospheric Teleconnection Patterns." In: *Nonlinear and Stochastic Climate Dynamics*. Ed. by C. L. E. Franzke and T. J. OKane. Cambridge: Cambridge University Press, pp. 54–104.

Fogt, R. L. et al. (2009). "Historical SAM Variability. Part II: Twentieth-Century Variability and Trends from Reconstructions, Observations, and the IPCC AR4 Models." In: *Journal of Climate* 22.20, pp. 5346–5365.

Gauss, M. et al. (2005). "Radiative forcing since preindustrial times due to ozone change in the troposphere and the lower stratosphere." In: *Atmospheric Chemistry and Physics Discussions* 5.4, pp. 5751–5807.

Gerber, E. P. and G. K. Vallis (2005). "A Stochastic Model for the Spatial Structure of Annular Patterns of Variability and the North Atlantic Oscillation." In: *Journal of Climate* 18.12, pp. 2102–2118.

Gerber, E. P. and D. W. J. Thompson (2017). "What Makes an Annular Mode "Annular"?" In: *Journal of the Atmospheric Sciences* 74.2, pp. 317–332.

Gillett, N. P., T. D. Kell, and P. D. Jones (2006). "Regional climate impacts of the Southern Annular Mode." In: *Geophysical Research Letters* 33.23.

Gillett, N. P. and D. W. J. Thompson (2003). "Simulation of recent southern hemisphere climate change." In: *Science (New York, N.Y.)* 302.5643, pp. 273–5.

Giorgetta, M. A. et al. (2013). "Climate and carbon cycle changes from 1850 to 2100 in MPI-ESM simulations for the Coupled Model Intercomparison Project phase 5." In: *Journal of Advances in Modeling Earth Systems* 5.3, pp. 572–597.

Gong, D. and S. Wang (1999). "Definition of Antarctic Oscillation index." In: *Geophysical Research Letters* 26.4, pp. 459–462.

Goosse, H. et al. (2010). *Introduction to climate dynamics and climate modelling*.

Greene, C. A. et al. (2017). "Wind causes Totten Ice Shelf melt and acceleration." In: *Science Advances* 3.11.

Hagemann, S., K. Arpe, and L. Bengtsson (2005). *Validation of the hydrological cycle of ERA 40*. Tech. rep. Max Planck Institute for Meteorology.

Hall, A. et al. (2002). “Synchronous Variability in the Southern Hemisphere Atmosphere, Sea Ice, and Ocean Resulting from the Annular Mode.” In: *Journal of Climate* 15.21, pp. 3043–3057.

Hasselmann, K. (1976). “Stochastic climate models Part I. Theory.” In: *Tellus* 28.6, pp. 473–485.

Ho, M., A. S. Kiem, and D. C. Verdon-Kidd (2012). “The Southern Annular Mode: a comparison of indices.” In: *Hydrology and Earth System Sciences* 16.3, pp. 967–982.

Hoegh-Guldberg, O. and J. F. Bruno (2010). “The impact of climate change on the world’s marine ecosystems.” In: *Science (New York, N.Y.)* 328.5985.

Holton, J. R. et al. (1995). “Stratosphere-troposphere exchange.” In: *Reviews of Geophysics* 33.4, p. 403.

Holz, A. and T. T. Veblen (2011). “Variability in the Southern Annular Mode determines wildfire activity in Patagonia.” In: *Geophysical Research Letters* 38.14.

Hoskins, B. J. and D. J. Karoly (1981). “The Steady Linear Response of a Spherical Atmosphere to Thermal and Orographic Forcing.” In: *Journal of the Atmospheric Sciences* 38.6, pp. 1179–1196.

Hoskins, J. B., E. M. Mcintyre, and A. W. Robertson (1985). *On the use and significance of isentropic potential vorticity maps*. Tech. rep., pp. 877–946.

Hourdin, F. et al. (2017). “The Art and Science of Climate Model Tuning.” In: *Bulletin of the American Meteorological Society* 98.3, pp. 589–602.

Hurrell, J. W. (1996). “Influence of variations in extratropical wintertime teleconnections on northern hemisphere temperature.” In: *Geophysical Research Letters* 23.6, pp. 665–668.

Jacobson, M. Z. (2005). *Fundamentals of atmospheric modeling*. Cambridge university press, pp. 1–5.

James, I. N. and P. M. James (1989). “Ultra-low-frequency variability in a simple atmospheric circulation model.” In: *Nature* 342.6245, pp. 53–55.

Jones, A. E. and J. D. Shanklin (1995). “Continued decline of total ozone over Halley, Antarctica, since 1985.” In: *Nature* 376.6539, pp. 409–411.

Jones, P. D. and D. H. Lister (2015). “Antarctic near-surface air temperatures compared with ERA-Interim values since 1979.” In: *International Journal of Climatology* 35.7, pp. 1354–1366.

Karoly, D. J. (1989). “Southern Hemisphere Circulation Features Associated with El Niño-Southern Oscillation Events.” In: *Journal of Climate* 2.11, pp. 1239–1252.

Kidson and W. John (1975). “Eigenvector Analysis of Monthly Mean Surface Data.” In: *Monthly Weather Review* 103.3, pp. 177–186.

Kreyling, D. et al. (2018). “The Extrapolar SWIFT model (version 1.0): fast stratospheric ozone chemistry for global climate models.” In: *Geoscientific Model Development* 11.2, pp. 753–769.

Lachlan-Cope, T. A., W. M. Connolley, and J. Turner (2001). “The role of the non-axisymmetric antarctic orography in forcing the observed pattern of variability of the Antarctic climate.” In: *Geophysical Research Letters* 28.21, pp. 4111–4114.

Lee, A. M. et al. (2001). “The impact of the mixing properties within the Antarctic stratospheric vortex on ozone loss in spring.” In: *Journal of Geophysical Research: Atmospheres* 106.D3, pp. 3203–3211.

Lee, S. and H.-k. Kim (2003). “The Dynamical Relationship between Subtropical and Eddy-Driven Jets.” In: *Journal of the Atmospheric Sciences* 60.12, pp. 1490–1503.

Lefebvre, W. et al. (2004). “Influence of the Southern Annular Mode on the sea ice–ocean system.” In: *Journal of Geophysical Research* 109.C9.

Li, C. and J. J. Wettstein (2012). “Thermally Driven and Eddy-Driven Jet Variability in Reanalysis.” In: *Journal of Climate* 25.5, pp. 1587–1596.

Limpasuvan, V. and D. L. Hartmann (1999). “Eddies and the annular modes of climate variability.” In: *Geophysical Research Letters* 26.20, pp. 3133–3136.

Linkin, M. E. and S. Nigam (2008). “The North Pacific Oscillation–West Pacific Teleconnection Pattern: Mature-Phase Structure and Winter Impacts.” In: *Journal of Climate* 21.9, pp. 1979–1997.

Liu, J., J. A. Curry, and D. G. Martinson (2004). “Interpretation of recent Antarctic sea ice variability.” In: *Geophysical Research Letters* 31.2.

Lovenduski, N. S. and N. Gruber (2005). “Impact of the Southern Annular Mode on Southern Ocean circulation and biology.” In: *Geophysical Research Letters* 32.11.

Machenhauer, B. (1979). “The spectral method.” In: *Numerical Methods Used in Atmospheric Models* 2, pp. 121–275.

Marshall, G. J. (2003). “Trends in the Southern Annular Mode from Observations and Reanalyses.” In: *Journal of Climate* 16.24, pp. 4134–4143.

Marshall, G. J. et al. (2004). “Causes of exceptional atmospheric circulation changes in the Southern Hemisphere.” In: *Geophysical Research Letters* 31.14.

Matsuno, T. (1971). “A Dynamical Model of the Stratospheric Sudden Warming.” In: *Journal of the Atmospheric Sciences* 28.8, pp. 1479–1494.

Meneghini, B., I. Simmonds, and I. N. Smith (2007). “Association between Australian rainfall and the Southern Annular Mode.” In: *International Journal of Climatology* 27.1, pp. 109–121.

Mikhailova, N. and A. Yurovsky (2016). “The East Atlantic Oscillation: Mechanism and Impact on the European Climate in Winter.” In: *Morskoy gidrofizicheskiy zhurnal* 4.

Miller, R. L., G. A. Schmidt, and D. T. Shindell (2006). “Forced annular variations in the 20th century Intergovernmental Panel on Climate Change Fourth Assessment Report models.” In: *Journal of Geophysical Research* 111.D18.

Mo, K. C. and J. N. Paegle (2001). “The Pacific-South American modes and their downstream effects.” In: *International Journal of Climatology* 21.10, pp. 1211–1229.

Monahan, A. H. (2000). “Nonlinear Principal Component Analysis by Neural Networks: Theory and Application to the Lorenz System.” In: *Journal of Climate* 13.4, pp. 821–835.

Mori, Y., M. Kuroda, and M. Naomichi (2016). *Nonlinear principal component analysis and its applications*. New York, NY: Springer US.

Mulvaney, R. et al. (2012). “Recent Antarctic Peninsula warming relative to Holocene climate and ice-shelf history.” In: *Nature* 489.7414, pp. 141–144.

Myhre, G. et al. (2013). “Anthropogenic and Natural Radiative Forcing. In: Climate Change 2013: The Physical Science Basis. Contribution of Working Group I to the Fifth Assessment Report of the Intergovernmental Panel on Climate Change.” In: *Cambridge University Press*.

Nan, S. and J. Li (2003). “The relationship between the summer precipitation in the Yangtze River valley and the boreal spring Southern Hemisphere annular mode.” In: *Geophysical Research Letters* 30.24.

North, G. R. et al. (1982). “Sampling Errors in the Estimation of Empirical Orthogonal Functions.” In: *Monthly Weather Review* 110.7, pp. 699–706.

Pachauri, R. K. et al. (2014). *Climate change 2014: synthesis report. Contribution of Working Groups I, II and III to the fifth assessment report of the Intergovernmental Panel on Climate Change*. Tech. rep. IPCC.

Paolo, F. S., H. A. Fricker, and L. Padman (2015). "Ice sheets. Volume loss from Antarctic ice shelves is accelerating." In: *Science (New York, N.Y.)* 348.6232, pp. 327–31.

Parker, W. S. (2016). "Reanalyses and Observations: What's the Difference?" In: *Bulletin of the American Meteorological Society* 97.9, pp. 1565–1572.

Perlwitz, J. et al. (2008). "Impact of stratospheric ozone hole recovery on Antarctic climate." In: *Geophysical Research Letters* 35.8.

Pichler, H. (1997). *Dynamik der Atmosphäre*. Spektrum Akademischer Verlag.

Randel, W. J. and F. Wu (1999). "Cooling of the Arctic and Antarctic Polar Stratospheres due to Ozone Depletion." In: *Journal of Climate* 12.5, pp. 1467–1479.

Reich, S. and C. J. Cotter (2014). *Probabilistic Forecasting and Bayesian Data Assimilation*.

Rex, M. et al. (2014). "Technical Note: SWIFT - a fast semi-empirical model for polar stratospheric ozone loss." In: *Atmospheric Chemistry and Physics* 14.13, pp. 6545–6555.

Richman, M. B. (1986). "Rotation of principal components." In: *Journal of Climatology* 6.3, pp. 293–335.

Rogers, C. J. and H. van Loon (1982). "Spatial Variability of Sea Level Pressure and 500 mb Height Anomalies over the Southern Hemisphere." In: *Monthly Weather Review* 110.10, pp. 1375–1392.

Romanowsky, E. et al. (2019). "The role of stratospheric ozone for Arctic-midlatitude linkages." In: *Scientific Reports* 9.1, p. 7962.

Schmidt, H. et al. (2013). "Response of the middle atmosphere to anthropogenic and natural forcings in the CMIP5 simulations with the Max Planck Institute Earth system model." In: *Journal of Advances in Modeling Earth Systems* 5.1, pp. 98–116.

Screen, J. A. and I. Simmonds (2011). "Erroneous Arctic Temperature Trends in the ERA-40 Reanalysis: A Closer Look." In: *Journal of Climate* 24.10, pp. 2620–2627.

Sempf, M. et al. (2005). "Idealized modelling of the northern annular mode: orographic and thermal impacts." In: *Atmospheric Science Letters* 6.2, pp. 140–144.

– (2007). "Toward Understanding the Dynamical Origin of Atmospheric Regime Behavior in a Baroclinic Model." In: *Journal of the Atmospheric Sciences* 64.3, pp. 887–904.

Seo, K.-H. and H.-J. Lee (2017). "Mechanisms for a PNA-Like Teleconnection Pattern in Response to the MJO." In: *Journal of the Atmospheric Sciences* 74.6, pp. 1767–1781.

Shaman, J. and E. Tziperman (2016). "The Superposition of Eastward and Westward Rossby Waves in Response to Localized Forcing." In: *Journal of Climate* 29.20, pp. 7547–7557.

Silberman, I. (1954). "Planetray waves in the atmosphere." In: *Journal of Meteorology* 11.1, pp. 27–34.

Silvestri, G. E. and C. S. Vera (2003). "Antarctic Oscillation signal on precipitation anomalies over southeastern South America." In: *Geophysical Research Letters* 30.21, p. 2115.

Solman, S. A. and I. Orlanski (2016). "Climate Change over the Extratropical Southern Hemisphere: The Tale from an Ensemble of Reanalysis Datasets." In: *Journal of Climate* 29.5, pp. 1673–1687.

Solomon, S. et al. (1986). "On the depletion of Antarctic ozone." In: *Nature* 321.6072, pp. 755–758.

Solomon, S. et al. (2016). "Emergence of healing in the Antarctic ozone layer." In: *Science (New York, N.Y.)* 353.6296, pp. 269–274.

Stevens, B. et al. (2013). "Atmospheric component of the MPI-M Earth System Model: ECHAM6." In: *Journal of Advances in Modeling Earth Systems* 5.2, pp. 146–172.

Stohl, A. et al. (2003). "Stratosphere-troposphere exchange: A review, and what we have learned from STACCATO." In: *Journal of Geophysical Research: Atmospheres* 108.D12.

Stolarski, R. S. and R. J. Cicerone (1974). "Stratospheric Chlorine: a Possible Sink for Ozone." In: *Canadian Journal of Chemistry* 52.8, pp. 1610–1615.

Taylor, K. E. (2001). "Summarizing multiple aspects of model performance in a single diagram." In: *Journal of Geophysical Research: Atmospheres* 106.D7, pp. 7183–7192.

Taylor, K. E., R. J. Stouffer, and G. A. Meehl (2012). "An Overview of CMIP5 and the Experiment Design." In: *Bulletin of the American Meteorological Society* 93.4, pp. 485–498.

Thompson, D. W. J. and J. M. Wallace (2000). "Annular Modes in the Extratropical Circulation. Part I: Month-to-Month Variability*." In: *Journal of Climate* 13.5, pp. 1000–1016.

Thompson, D. W. J. and S. Solomon (2002). "Interpretation of recent Southern Hemisphere climate change." In: *Science (New York, N.Y.)* 296.5569, pp. 895–9.

Thompson, D. W. J., M. P. Baldwin, and S. Solomon (2005). "Stratosphere–Troposphere Coupling in the Southern Hemisphere." In: *Journal of the Atmospheric Sciences* 62.3, pp. 708–715.

Torrence, C. and G. P. Compo (1998). "A Practical Guide to Wavelet Analysis." In: *Bulletin of the American Meteorological Society* 79.1, pp. 61–78.

Torrence, C. and P. J. Webster (1999). "Interdecadal Changes in the ENSO–Monsoon System." In: *Journal of Climate* 12.8, pp. 2679–2690.

Trigo, R. M., T. J. Osborn, and J. M. Corte-Real (2002). "The North Atlantic Oscillation influence on Europe: climate impacts and associated physical mechanisms." In: *Climate Research* 20.1, pp. 9–17.

Turner, J. et al. (2016). "Absence of 21st century warming on Antarctic Peninsula consistent with natural variability." In: *Nature* 535.7612, pp. 411–415.

Vallis, G. K. and E. P. Gerber (2008). "Local and hemispheric dynamics of the North Atlantic Oscillation, annular patterns and the zonal index." In: *Dynamics of Atmospheres and Oceans* 44.3-4, pp. 184–212.

Walker, G. T. (1923). "Correlation in seasonal variation of weather. VIII : A preliminary study of world weather." In: *Memoirs of India Meteorological Department* 24, pp. 75–131.

Wallace, J. M. and D. S. Gutzler (1981). "Teleconnections in the Geopotential Height Field during the Northern Hemisphere Winter." In: *Monthly Weather Review* 109.4, pp. 784–812.

Wang, Q. et al. (2014). "The Finite Element Sea Ice-Ocean Model (FESOM) v.1.4: formulation of an ocean general circulation model." In: *Geoscientific Model Development* 7.2, pp. 663–693.

Waugh, D. W., A. H. Sobel, and L. M. Polvani (2017). "What Is the Polar Vortex and How Does It Influence Weather?" In: *Bulletin of the American Meteorological Society* 98.1, pp. 37–44.

Wilks, D. S. (2006). *Statistical methods in the atmospheric sciences*. Academic Press, p. 627.

Wofsy, S. C., M. B. McElroy, and Y. L. Yung (1975). "The chemistry of atmospheric bromine." In: *Geophysical Research Letters* 2.6, pp. 215–218.

Wohltmann, I. and M. Rex (2009). "The Lagrangian chemistry and transport model ATLAS: validation of advective transport and mixing." In: *Geoscientific Model Development* 2.2, pp. 153–173.

Wohltmann, I., R. Lehmann, and M. Rex (2017). “Update of the Polar SWIFT model for polar stratospheric ozone loss (Polar SWIFT version 2).” In: *Geosci. Model Dev* 10, pp. 2671–2689.

Zheng, F. et al. (2013). “Simulation and Projection of the Southern Hemisphere Annular Mode in CMIP5 Models.” In: *Journal of Climate* 26.24, pp. 9860–9879.

ACRONYMS

AAO	Antarctic Oscillation
AO	Arctic Oscillation
AAOI	Antarctic Oscillation-index
AGCM	Atmospheric General Circulation model
AR	Autoregressive
AMIP	Atmospheric Model Intercomparison Project
CCM	Chemistry Climate Model
CFC	ChloroFluoroCarbons
CMIP5	Coupled Model Intercomparison Project Phase 5
DJF	December, January, February
EAO	East Atlantic Oscillation
ENSO	El Niño-Southern Oscillation
EOF	Empirical Orthogonal Function
ESM	Earth System Model
GCM	General Circulation Model
JJA	June, July, August
MAM	March, April, May
MPI-ESM	Max Planck Institute for Meteorology Earth System Model
NAM	Northern Annular Mode
NAO	North Atlantic Oscillation
NH	Northern Hemisphere
NPO	North Pacific Oscillation
PC	Principal Component
PNA	Pacific North American Oscillation

PSC	Polar Stratospheric Cloud
SAM	Southern Annular Mode
SIE	Sea Ice Extent
SH	Southern Hemisphere
SO	Southern Oscillation
SON	September, October, November
SLP	Sea Level Pressure
SST	Sea Surface Temperature
STFT	Short-Time Fourier Transform

DANKSAGUNG

Danken möchte ich an erster Stelle meiner Betreuerin Dörthe Handorf für die wirklich jederzeit liebevolle und kompetente Unterstützung, sowie natürlich auch Markus Rex, dass ich in seiner Arbeitsgruppe meine Masterarbeit schreiben konnte und das vergangene Jahr wirklich sehr viel lernen konnte. Ebenso danken möchte ich Arkady Pikovksy, dass er sich als Zweitgutachter für meine Arbeit bereit erklärt hat.

Zudem möchte ich auch noch Sabine Erxleben vor allem für den IT-support in den ersten Wochen danken, sowie Daniel Kreyling für das Aufsetzen der Modellläufe. Ein Dank geht auch raus an Sandro, Marie, Benjamin, Jan und Ingo für das Korrekturlesen von Teilen meiner Arbeit, sowie eigentlich auch an das gesamte AWI Team samt aller Post-Docs, Doktoranten und anderen Studenten für die wirklich nette und familiäre Atmosphäre innerhalb der Arbeitsgruppe und die gemeinsamen Aktivitäten auch außerhalb des Institutsalltags.

Zum Ende will ich auch noch meinen Eltern und meiner Familie danken, die mich vom Anfang bis zum Ende meiner Studienzeit stets unterstützt haben.

SELBSTSTÄNDIGKEITSERKLÄRUNG

Hiermit versichere ich, dass ich die vorliegende Masterarbeit selbstständig verfasst und keine anderen als die angegebenen Quellen und Hilfsmittel verwendet habe, wobei ich alle wörtlichen und sinngemäßen Zitate als solche gekennzeichnet habe.
Diese wissenschaftliche Arbeit hat in gleicher oder¨ahnlicher Form noch keiner P¨rufungsbehörde vorgelegen und wurde auch nicht veröffentlicht.

Potsdam, 31. Juli 2019

Johannes Riebold